Insights into conformational heterogeneity of an RRM: implications for fibril formation

विद्या वाचस्पति की
उपाधि की अपेक्षाओं की आंशिक पूर्ति में प्रस्तुत शोध प्रबंध

A thesis submitted in partial fulfillment of the requirements of the degree of Doctor of Philosophy

द्वारा / By
ओसामा आज़मी / OSAMA AAZMI

पंजीकरण सं. / Registration No.: 20203712

शोध प्रबंध पर्यवेक्षक / डॉ. जीतेंद्र चुघ

Thesis Supervisor: Dr. Jeetender Chugh

भारतीय विज्ञान शिक्षा एवं अनुसंधान संस्थान पुणे
INDIAN INSTITUTE OF SCIENCE EDUCATION AND RESEARCH PUNE
2025

<u>Dedicated to all who have suffered in pursuit of hidden conformations, silent chemical shifts, and the whispered truths of spin</u>

Doing Any Research Work, Is HOW A HERCULEAN TASK, can be understood by only them, who have themselves done any kind of Such Research. It Demands, Not Only High Ambition, Nail-Sweating Labour, Courage, But Also A Great Deal of PATIENT PERSISTENCE. This reminds me of something important, as quoted by:

In Anyone's BOSOM, IF NO HOLY FIRE IS INFLAMING
WHAT's There THEN, In ANY SUCH LIVING

STRUGGLING WITH ALL TROUBLES, YOU BECOME,
IF YOU MAY
ON ANY ROAD TO GREATNESS, THERE's
NO MILKY WAY

(Nadir Kaainati)

भारतीय विज्ञान शिक्षा एवं अनुसंधान संस्थान पुणे
INDIAN INSTITUTE OF SCIENCE EDUCATION AND RESEARCH PUNE
डॉ. होमी भाभा मार्ग, पुणे 411008, महाराष्ट्र, भारत | Dr. Homi Bhabha Road, Pune 411008, Maharashtra, India
T +91 20 2590 8001 W www.iiserpune.ac.in

IISER PUNE

DECLARATION

I declare that this written submission entitled as ***"Insights into conformational heterogeneity of an RRM: implications for fibril formation"*** represents my idea in my own words and where others' ideas have been included; I have adequately cited and referenced the original sources. I also declare that I have adhered to all principles of academic honesty and integrity and have not misrepresented or fabricated or falsified any idea/data/fact/source in my submission. I understand that violation of the above will be cause for disciplinary action by the Institute and can also evoke penal action from the sources which have thus not been properly cited or from whom proper permission has not been taken when needed.

The work reported in this thesis is the original work done by me under the guidance of Dr. Jeetender Chugh.

Date: 30.07.2025

Osama Aazmi
Signature of the student

भारतीय विज्ञान शिक्षा एवं अनुसंधान संस्थान पुणे
INDIAN INSTITUTE OF SCIENCE EDUCATION AND RESEARCH PUNE
डॉ. होमी भाभा मार्ग, पुणे 411008, महाराष्ट्र, भारत | Dr. Homi Bhabha Road, Pune 411008, Maharashtra, India
T +91 20 2590 8001 W www.iiserpune.ac.in

IISER PUNE

CERTIFICATE

Certified that the work incorporated in the thesis entitled "***Insights into conformational heterogeneity of an RRM: implications for fibril formation***" submitted by ***Osama Aazmi*** was carried out by him, under my supervision. The work presented here or any part of it has not been included in any other thesis submitted previously for the award of any degree or diploma from any other University or institution.

Date: 30.07.2025

Signature of the supervisor

Acknowledgements

I would like to express my sincere gratitude to everyone who has supported me throughout the duration of this project. It's simply impossible to go through this process without thanking some very special people.

First and foremost, I would like to extend my deepest appreciation to my supervisor, Dr. Jeetender Chugh, for his guidance, support, and mentorship. His constant feedback and advice have greatly contributed to the successful completion of this project. Sincere thanks to my RAC members, Dr. Santosh Kumar Jha and Dr. Gayathri Pananghat for their thoughtful discussions during RAC meetings.

I would like to express sincere gratitude to Prof. Neel Sarovar Bhavesh (ICGEB, New Delhi, India) for generously providing the FUS-RRM plasmids. I am very thankful to Prof. Jayant B. Udgaonkar for providing the facility to measure aggregation kinetics and also extend my thanks to Dr. Radha Chauhan (NCCS) and Ms. Jyotsna (NCCS) for their assistance with the SEC-MALS experiments. I am also grateful to Ms. Madhurima from IISc Bangalore for her kindness and for generously taking the time to assist me with the CEST experiments.

I would also like to thank my past and present lab members, Dr. Firdousi, Soumya, Nikhil, Zainab, Ipsita, Nikhat, Devika, and Akshit for their unwavering support and motivation. They were always there to offer encouragement, share ideas, and provide both emotional and practical assistance when needed. It is impossible not to thank Ishtiyaq and Hilal for the wonderful memories I've had during my journey.

I am also thankful to Sandeep, Nitin and Karan for keeping the magnet alive and specially Sandeep and Nitin for their quick support during NMR breakdown.

I am deeply thankful to my family for their unwavering support, love, and especially their heartfelt Dua, which gave me the strength and motivation to complete this work. They are truly the greatest gift in my life, and I am profoundly grateful to the Almighty for blessing me with them.

Synopsis

Insights into conformational heterogeneity of an RRM: implications for fibril formation

Name: Mr. Osama Aazmi.

Registration No.: 20203712.

Thesis Supervisor: Dr. Jeetender Chugh.

Department: Department of Biology, IISER Pune.

In this thesis, we aim to characterize the structural dynamics of FUS-RRM with NMR spectroscopy. We have focused on understanding the role of conformational dynamics in FUS-RRM aggregation, coupled with other biophysical tools. To present the outcomes of our study, we have curated such results as the chapters of this thesis, as follows:

Chapter 1: Introduction

The importance of protein dynamics in cellular function has been widely accepted by experimental and computational methods (1-3). However, because of the inherent flexibility of proteins, it is difficult to assign a direct role to their specific functions. For human fused in sarcoma (FUS) protein, a combination of biophysical experiments has elucidated its role in liquid-liquid phase separation (LLPS) and aggregation (4, 5). FUS, implicated in neurodegenerative diseases, contains N- and C-terminal LC-rich regions and a single RNA-recognition motif (RRM) (6). FUS-RRM consists of βαββαβ arrangement of secondary structures and is a well-folded domain. Recent experiments have shown FUS-RRM can also form fibrils in solution; however, the detailed molecular insights into the fibrillation process are yet to be deciphered (7). We hypothesized the role of conformational dynamics in dictating FUS-RRM aggregation and tried to elucidate it using pH and ATP perturbations.

Chapter 2: Investigating conformational heterogeneity and fibril formation in FUS-RRM

In this chapter, we have characterized FUS-RRM aggregation kinetics at pH 6.4. To gain insights into the role of dynamics in its aggregation, we identified fast µs-ms dynamics of FUS-RRM using adiabatic $R_{1\rho}$ and $R_{2\rho}$ experiments and slow µs-ms dynamics using ^{15}N CEST. By using these advance NMR techniques, we establish the presence of conformational heterogeneity and its role in FUS-RRM aggregation.

Chapter 3: pH-perturbation on dynamics and FUS-RRM fibril formation

The thermodynamic stability of protein conformations results from a delicate balance between electrostatic interactions, hydrophobic forces, and the environmental cues perturbing these interactions (8, 9).

A change in pH is one such perturbation that can disrupt this balance, leading to structural transitions and functional alterations in proteins, such as a change in specificity, allostery, and protein misfolding (10).

In order to understand the role of conformational dynamics in FUS-RRM aggregation, we carried out pH-perturbations. At pH 4.6, we observed quenching of the fast μs-ms dynamics, indicating that the protein is rigidified and undergoing slow exchange. For the slow μs-ms dynamics, on the other hand, we found an increase in population of the excited state. Using different biophysical techniques, while no change was observed in the monomer structure, aggregation is found to be accelerated with a change in the final fibril state. This chapter thus highlights the role of conformational dynamics in altering the pathway to FUS-RRM aggregation, which can have different cellular fates.

Chapter 4: ATP-induced perturbation on dynamics and fibrillation of FUS-RRM domain

Small molecule ATP has been shown to bind FUS-RRM (11). Therefore, we used it to test its effect on FUS-RRM dynamics and aggregation. The contrasting effects of ATP on fast and slow dynamics at pH 6.4 and 4.6, along with the corresponding changes in aggregation behavior, suggest a complex relationship between ATP, pH, and protein aggregation kinetics. Surprisingly, we also observed ATP restores faster dynamics at low pH. We speculate that increased fast dynamics are important for delaying aggregation, as has also been suggested by other studies, but will need further investigations.

Chapter 5: Conclusions and future directions

The results from this study provide important insights into the conformational dynamics of FUS-RRM, a key domain involved in RNA binding and cellular regulation. By combining CEST, adiabatic $R_{1\rho}$ and $R_{2\rho}$ relaxation dispersion, AFM, and CD spectroscopy, this study uncovers the existence of different excited states. The exchange between these conformational states may be crucial for FUS-RRM's functional roles, particularly its ability to interact with different nucleic acids. The results of pH-dependent aggregation kinetics suggest that there might be a certain optimum concentration of cellular ATP levels relative to the protein concentration that can inhibit or delay the formation of amyloid aggregates. As cells undergo

stress, higher ATP levels could stabilize the distinct conformation and thus prevent aggregation. An increased concentration of ATP might thus be a safeguard against aggregation-prone proteins during stress conditions or upon aging. This study provides key insights into the role of conformational dynamics in FUS-RRM aggregation. Moving forward, several important avenues remain to be explored, such as, determining the structure of excited state using ^{13}C CEST, performing cell-based assays to evaluate cytotoxicity of aggregates, linking its aggregation to pathological relevance.

References

1. Boehr DD, Dyson HJ, Wright PE. An NMR perspective on enzyme dynamics. Chemical reviews. 2006;106(8):3055-79.
2. Kay LE. New Views of Functionally Dynamic Proteins by Solution NMR Spectroscopy. Journal of molecular biology. 2016;428(2 Pt A):323-31.
3. Shukla D, Hernández CX, Weber JK, Pande VS. Markov state models provide insights into dynamic modulation of protein function. Accounts of chemical research. 2015;48(2):414-22.
4. Lu Y, Lim L, Song J. RRM domain of ALS/FTD-causing FUS characteristic of irreversible unfolding spontaneously self-assembles into amyloid fibrils. Scientific reports. 2017;7(1):1043.
5. Patel A, Lee HO, Jawerth L, Maharana S, Jahnel M, Hein MY, et al. A Liquid-to-Solid Phase Transition of the ALS Protein FUS Accelerated by Disease Mutation. Cell. 2015;162(5):1066-77.
6. Afroz T, Cienikova Z, Clery A, Allain FHT. One, Two, Three, Four! How Multiple RRMs Read the Genome Sequence. Methods Enzymol. 2015;558:235-78.
7. Agrawal S, Kuo PH, Chu LY, Golzarroshan B, Jain M, Yuan HS. RNA recognition motifs of disease-linked RNA-binding proteins contribute to amyloid formation. Scientific reports. 2019;9(1):6171.
8. Mishra P, Patni D, Jha SK. A pH-dependent protein stability switch coupled to the perturbed pKa of a single ionizable residue. Biophys Chem. 2021;274:106591.
9. Pace CN. Polar group burial contributes more to protein stability than nonpolar group burial. Biochemistry. 2001;40(2):310-3.
10. Moulick R, Goluguri RR, Udgaonkar JB. Ruggedness in the Free Energy Landscape Dictates Misfolding of the Prion Protein. Journal of molecular biology. 2019;431(4):807-24.
11. Kang J, Lim L, Song J. ATP binds and inhibits the neurodegeneration-associated fibrillization of the FUS RRM domain. Communications biology. 2019;2:223.

List of Publications

1. Aazmi O, Aswale AR, Saju L, Chugh J. Investigating the role of conformational heterogeneity in FUS-RRM fibrillation. Int J Biol Macromol. 2025;311(Pt 3):143954.
2. Aazmi O, Aswale AR, Chugh J. H+ ions and ATP reshape the conformational landscape of an RNA recognition motif, regulating fibrillation. (Manuscript under preparation).

Abbreviations

°C	Degree Celcius
Å	Angstrom
aa	Amino acid
ATP	Adenosine triphosphate
ANS	8-Anilinio-1-naphthalenesulphonic acid
kcal	Kilo-calorie
CD	Circular Dichroism
CPMG	Carr-Purcell-Meiboom-Gill
CSA	Chemical Shift Anisotropy
CSP	Chemical Shift Perturbation
D_2O	Deuterium oxide
DEST	Dark Exchange Saturation Transfer
DNA	Deoxy-ribonucleic acid
DTT	Dithiothreitol
EDTA	Ethylene diamine tetraacetic acid
HARD	Heteronuclear Adiabatic Relaxation dispersion
hr	Hour
HS	Hyperbolic Secant
HSQC	Heteronuclear Single Quantum Coherence
HMQC	Heteronuclear Multiple Quantum Coherence
Hz, kHz, MHz	Hertz, kilo-Hertz, mega-Hertz
IPTG	Isopropyl-β-D-1-thiogalactopyranoside
ITC	Isothermal Titration Calorimetry
K	Kelvin
LB	Lysogeny Broth
kDa	Kilo-Dalton
M, mM, µM	Mole, milli-mole, micro-mole
MALS	Multi-Angle Light Scattering
MBP	Maltose Binding Protein
miRNA	microRNA
ml, µl	Milli-liter, micro-liter
NaCl	Sodium chloride
nm	Nano-meter
NMR	Nuclear Magnetic Resonance
NOE	Nuclear Overhauser Effect
OD	Optical Density

PDB	Protein Data Bank
ppm	Parts per million
RD	Relaxation Dispersion
RNA	Ribonucleic acid
s, ms, µs, ps, ns	Second, milli-second, micro-second, pico-second, nano-second
SDS-PAGE	Sodium dodecyl sulfate - Polyacryl Amide Gel Electrophoresis
SEC	Size Exclusion Chromatography
SOFAST	Selective Optimized-Flip-Angle Short-Transient
TITAN	TITration ANalysis
TSP	Total Soluble Protein

Table of Contents

Chapter 1: Introduction 1
1.1 The protein structure 2
1.2 Protein folding pathway 3
1.3 Protein aggregation and formation of amyloids 4
1.4 RNA-binding proteins (RBPs) and their involvement in neurodegenerative diseases 5
1.5 The structural features of FUS 6
1.6 Protein dynamics 7
1.7 Chemical exchange and dynamic processes in NMR 9
1.8 Biophysical techniques to study protein conformations 11
1.8.1 Circular dichroism (CD) spectroscopy 11
1.8.2 Fluorescence spectroscopy 12
1.8.2.1 8-anilino-1-naphthalenesulfonic acid (ANS) fluorescence 13
1.8.3 Size exclusion chromatography – multi-angle light scattering (SEC-MALS) 14
1.8.4 Atomic force microscopy (AFM) 15
1.8.5 Transmission electron microscope (TEM) 16
1.8.6 Nuclear magnetic resonance (NMR) spectroscopy 18
1.8.6.1 Basic steps in the NMR experiment 20
1.8.6.2 Spin relaxation 21
1.8.6.2.1 Longitudinal relaxation (T_1) 21
1.8.6.2.2 Transverse relaxation (T_2) 23
1.8.6.2.3 Nuclear Overhauser Effect (NOE) 24
1.8.6.2.4 Dipole-dipole relaxation in liquids 25
1.8.6.2.5 Chemical Shift Anisotropy (CSA) 26
1.8.6.2.6 Effect of molecular tumbling on relaxation 27
1.8.6.3 Heteronuclear adiabatic relaxation dispersion (HARD) 28
1.8.6.4 ^{15}N chemical exchange saturation transfer (CEST) for slow μs-ms dynamics 30
1.9 Scope of the Thesis 31
1.10 References 32
Chapter 2: Investigating conformational heterogeneity and fibril formation in FUS-RRM ... 36
2.1 Introduction 37
2.2 Methods 38
2.2.1 Protein overexpression and purification 38
2.2.2 NMR Spectroscopy 38
2.2.2.1 ^{15}N HARD 39

2.2.2.2 ^{15}N CEST experiment 39
2.2.3 Random coil chemical shift prediction using POTENCI 40
2.2.4 Circular dichroism (CD) spectroscopy 40
2.2.5 Aggregation kinetics 41
2.2.6 AFM imaging 42
2.2.7 SEC-MALS (Size-Exclusion Chromatography with Multi-Angle Light Scattering) 42
2.3 Results 42
2.3.1 Protein overexpression and purification 42
2.3.2 Protein size confirmation 43
2.3.3 FUS-RRM aggregation kinetics 44
2.3.4 Adiabatic $R_{1\rho}$ and $R_{2\rho}$ for characterisation of fast µs-ms dynamics 46
2.3.5 Characterisation of slow µs-ms dynamics using ^{15}N CEST 47
2.3.6 The ES^{CEST} of FUS-RRM is an unfolded state 49
2.4 Discussion 52
2.5 References 53
Chapter 3: pH-perturbation on dynamics and FUS-RRM fibril formation 55
3.1 Introduction 56
3.2 Methods 58
3.2.1 NMR Spectroscopy 58
3.2.2 Chemical shift perturbation (CSP) 58
3.2.3 Circular dichroism (CD) spectroscopy 59
3.2.4 Fluorescence spectroscopy 59
3.2.5 8-Anilinio-1-naphthalenesulphonic acid (ANS) fluorescence spectroscopy 59
3.2.6 Thermal stability 59
3.2.7 Aggregation kinetics 60
3.2.8 AFM imaging 60
3.3 Results 60
3.3.1 Adiabatic $R_{1\rho}$ and $R_{2\rho}$ for characterisation of fast µs-ms dynamics 60
3.3.2 Characterisation of slow µs-ms dynamics using ^{15}N CEST at pH 4.6 61
3.3.3 pH-induced structural perturbations 63
3.3.4 pH-induced perturbation on aggregation kinetics 67
3.3.5 pH-induced perturbation in the fibril state 67
3.4 Proposed model 68
3.5 Discussion 69
3.6 References 70

Chapter 4: ATP-induced perturbation on dynamics and fibrillation of FUS-RRM domain 72
4.1 Introduction....73
4.2 Methods....73
4.2.1 Selective Optimized-Flip-Angle Short-Transient (SOFAST)-HMQC and data fitting in TITAN.....73
4.2.2 ^{15}N HARD....74
4.2.3 ^{15}N CEST....74
4.2.4 Aggregation kinetics....75
4.2.5 TEM imaging....75
4.3 Results....75
4.3.1 NMR titration study of ATP-binding to FUS-RRM....75
4.3.2 ATP modulates the ES^{HARD} of FUS-RRM....77
4.3.3 ATP modulates the ES^{CEST} of FUS-RRM....78
4.3.4 Aggregation kinetics....81
4.4 Proposed model....82
4.5 Discussion....83
4.6 References....84
Chapter 5: Conclusions and Future Directions....86
5.1 Conclusions....87
5.2 Future Directions....88
5.3 References....89
Appendix 1: Protein over-expression and purification....90
Appendix 2: Supporting tables....96

Chapter 1: Introduction

1.1 The protein structure

Macromolecules such as proteins (polymers of amino acids), nucleic acids (polymers of nucleotides), carbohydrates (polymers of sugars), and lipids (with a variety of modular constituents) are made up of basic molecular units (1). Nature has evolved to utilize these biomolecules in a very sophisticated manner, with each of these displaying unique structural features and biological characteristics.

Amongst the different macromolecules listed above, proteins represent several levels of structural complexity (Figure 1.1) as described below:

i) *Primary structure*: The primary structure of a protein represents the linear arrangements of the different types of amino acids spanning from N- to C-terminus of the sequence (2).

ii) *Secondary structure*: The secondary structure comprises sequence-based arrangements of amino acids giving rise to a special topology widely known as α-helices and β-sheets. These are sustained by hydrogen bonds between the nitrogen and oxygen atoms of the stacked backbone amide groups. Additionally, these also include loops, 3_{10} helix, polyproline structures, and other relatively less common motifs like β-turns, and coiled coils (2, 3).

iii) *Tertiary structure*: The tertiary structure represents the spatial arrangements of the side chains of amino acids which are stabilized by non-covalent interactions (except for cysteine disulfide bonds) such as van der Waals, electrostatic, and hydrophobic interactions (2, 3).

iv) *Quaternary structure*: To achieve conformational diversity and functions, proteins adopt a quaternary structure. This also provides a synergistic effect between domains (2, 3).

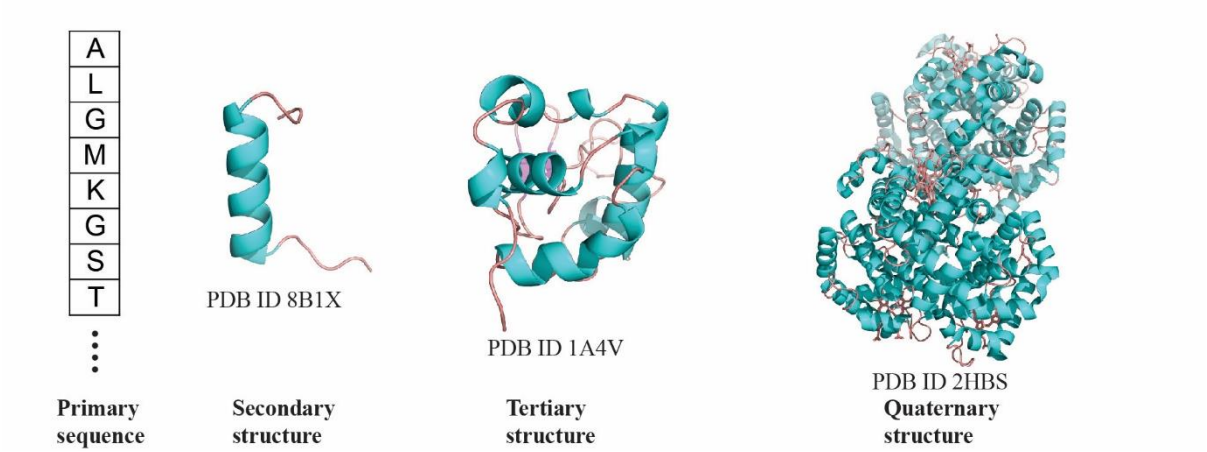

Figure 1.1. The different levels used to represent protein structures. The primary sequence contains information about overall protein fold starting from secondary structures to three-dimensional tertiary and quaternary structures.

While machine-learning algorithms such as AlphaFold (4) have advanced our knowledge in predicting the structure of a protein from its sequence, it fails to provide the

information about how and why that a given conformation is achieved during folding. For the same, gaining insights into the protein folding pathway is beneficial.

1.2 Protein folding pathway

As per the classical model (5), protein folding relied on the kinetics experiments by observing the population of the native (N) and denatured (D) states over time and fitting the data to a two-state model. It also took into account the presence of on- or off-pathway intermediates (I). In contrast to the classical model, the new model (6, 7) of protein folding considers different microstates of the protein that are best represented through the free energy funnel (Figure 1.2). This free energy funnel is built upon two important parameters: (i) protein conformational states, and (ii) free energy of each state, starting with a large number of disordered conformations (high entropy) and gradually transitioning to a well-ordered native conformation (low entropy). The free energy landscape theory (6) suggests that proteins exist in a dynamic ensemble of conformations rather than adopting a single, fixed structure. It emphasizes the need for flexibility in protein structures to respond to different environmental stimuli and stresses on the importance of considering proteins not as rigid, isolated entities, but as dynamic, adaptable ensembles.

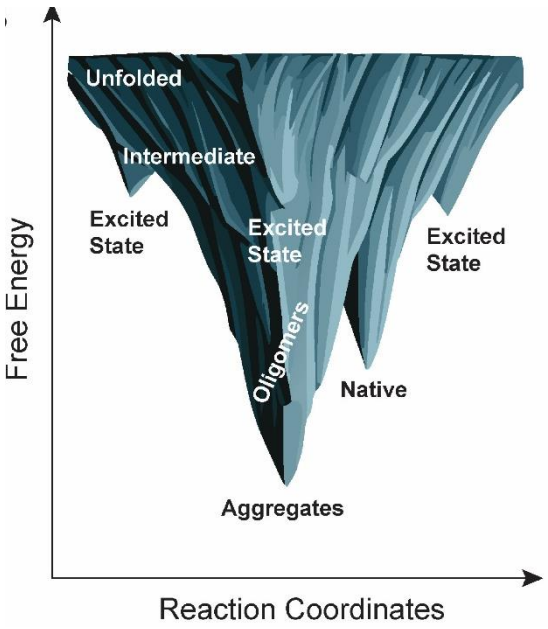

Figure 1.2. Free energy landscape used to describe protein folding and dynamics. The Y-axis represents the free energy; the higher the value, the less stable the state is. The X-axis represents reaction coordinates that depicts the progress towards a more stable state from unfolded state, while encountering different excited states and oligomers.

Experimental and theoretical studies have demonstrated that protein hierarchically achieves its native state following several alternative paths to fold (5, 8). These alternative

paths arise due to conformational heterogeneity existing at each step of protein folding. Even the native state is heterogeneous, and the nature and degree of conformational heterogeneity present are poorly understood. The major reasons behind that are:

1. low population of many conformational states,
2. isostructural and isoenergetic conformational states, and
3. rapid interconversion between these states.

The conformational heterogeneity could be associated with the dynamics of the structural elements of proteins. The state a protein adopts under a specific condition(s) depends upon the thermodynamic and kinetics of different conformations. Hence, it is important to decipher its role in protein folding or misfolding.

1.3 Protein aggregation and formation of amyloids

Proteins perform their cellular functions by folding into specific conformations (9). However, some proteins, known as intrinsically disordered proteins (IDPs), which are not fully folded and remain flexible can still perform cellular functions by interacting with different partners (10). The failure to fold or to remain correctly folded can lead to the progression towards different disease such as cancer, cystic fibrosis, etc. (11, 12). Some proteins have a greater tendency to misfold and escape the protective mechanisms to form aggregates. These aggregates are associated with multiple forms of neurodegenerative diseases such as Alzheimer's, Parkinson's, spongiform encephalopathies, etc. (13, 14). The amyloid deposits present in such diseases are characterized by a characteristic 'cross-β' X-ray fiber diffraction pattern (15) and also distinct optical properties on binding certain dyes such as thioflavin T (ThT) (16).

The ability of proteins to form amyloids is not restricted to only a few proteins, but it is now considered a generic feature of many proteins, including globular proteins like myoglobin (17). The buried hydrophobic amino acids in such proteins are exposed during pH stress, and their chances of forming amyloids increase. Stress conditions like pH, temperature, etc., can affect the folding pathways and, hence, the cellular functions, leading to protein misfolding and the formation of insoluble amyloid fibers (18).

1.4 RNA-binding proteins (RBPs) and their involvement in neurodegenerative diseases

RNA-binding proteins (RBPs) are involved in the formation of ribonucleoprotein (RNP) complexes and in the regulation of gene expression (19). They are characterized by well-defined RNA-binding domains (RBDs) such as RNA-Recognition Motif (RRM), K-homology (KH), etc. (19). The presence of RBDs like RRM and KH indeed plays a crucial role in defining the specificity and affinity of these proteins for their RNA targets (20). The association of RRM(s) with protein-coding genes that contain prion-like domains raises intriguing possibilities regarding the behaviour of these RBPs (Figure 1.3) (21). The prion-like properties of certain RNA-binding proteins suggest that they can form self-replicating aggregates, which is particularly relevant in the context of neurodegenerative diseases, such as amyotrophic lateral sclerosis (ALS) and frontotemporal lobe degeneration (FTLD), where protein aggregation is a hallmark (22-24).

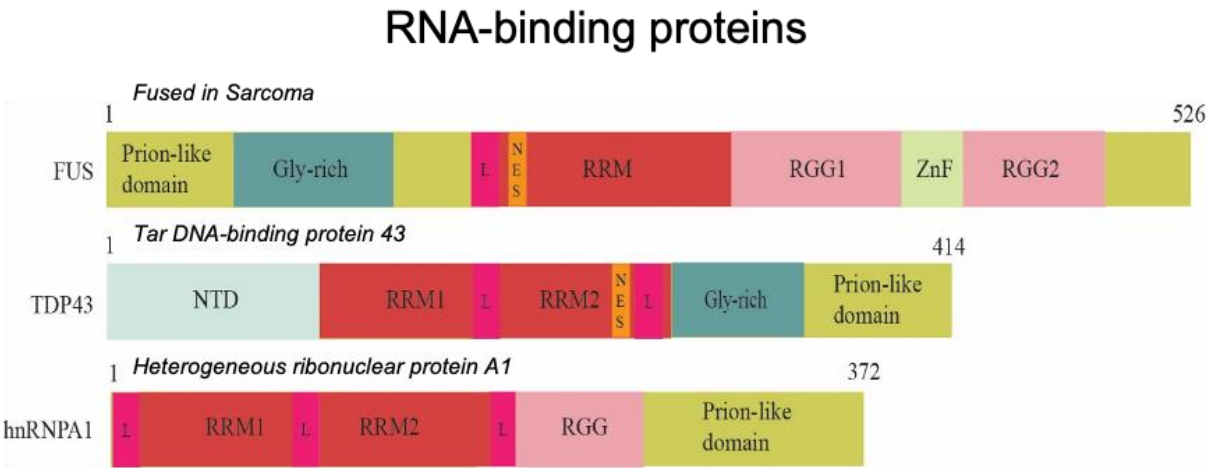

Figure 1.3. Structural features of some RNA binding proteins (RBPs). The prominent features include the presence of prion-like domain and the RNA recognition motifs (RRMs).

By exploring the mechanisms through which RRM-containing proteins may contribute to the formation of pathological aggregates, one could uncover new pathways or therapeutic targets for managing these conditions. This connection highlights the importance of understanding the functional roles of RNP complexes beyond their classical roles in gene regulation, especially in the context of cellular stress and disease. Among the top RRM-bearing prion candidates, FUsed in Sarcoma (FUS) is a crucial RBP associated with various neurodegenerative diseases (25). Some of the important characteristics of FUS and implications in these conditions have been listed below:

a. Cellular Function: FUS plays an important role in RNA metabolism, such as transcription, RNA splicing, and mRNA transport. It shuttles between the nucleus and cytoplasm to perform its functions (26).

b. Impact of Mutations: Several mutations have been identified in FUS, which can disrupt its localization and can induce abnormal accumulation in the cytoplasm (27). This mis-localisation is the hallmark of FUS-related pathologies.

c. Disease Associations: FUS cytoplasmic deposits are found in patients suffering from neurodegenerative diseases including ALS, FTLD, etc. (25).

d. Aggregation and Pathology: FUS leads to aggregate and filamentous structures within cells (27). These aggregates are thought to contribute to neuronal cell death (28).

1.5 The structural features of FUS

FUS is composed of an N-terminal low-complexity (LC) domain, an RNA-Recognition Motif, and a C-terminal LC domain, including the arginine-glycine-glycine (RGG) motif (Figure 1.4). The unique amino acid composition and specific sequences within the FUS-LC are important for normal cellular function but can be dysregulated in disease conditions. A high percentage of specific amino acids such as glycine, serine, glutamine, and tyrosine are present, which causes the FUS-LC domain to form reversible amyloid cores (RAC) (29). These sequences have been investigated to mediate liquid-liquid phase separation (LLPS) and have been known to play an important role in fibril formation (30).

The RRM domain of the human FUS protein is known for its unique structural features, including a non-canonical nucleic acid binding site (31). Unlike traditional RRM domains, which typically have well-defined sequences and structures for RNA binding, the FUS-RRM exhibits variations that allow it to interact with RNA more flexibly. FUS-RRM is composed of βαββαβ type of secondary arrangements and consists of highly conserved sequences among different species (31). Unlike the classical RRM fold, FUS-RRM is quite distinct. The solution NMR structure (PDB ID: 2LCW) reveals the same overall fold with four β-strands stacking onto two α-helices (31) (Figure 1.4). However, the nucleic acid-binding pocket is distorted, and critical aromatic amino acid residues are missing compared to canonical RRMs (32). For example, residues F147 and F149, critical to RNA-binding in TDP43, correspond to E336 and T338 in FUS. T286 and S387 replace the Lys residues in β1 and β4 in FUS-RRM (32). Further,

FUS-RRM has been shown to form small fibril-like structures and exhibit amyloid-like properties (33). This characteristic could be attributed to its role in mediating cytotoxicity in the neuronal cells (34). Hence, it is necessary to understand its mechanism of aggregation, which could help in designing small molecules that inhibit amyloid formation. Indeed, the ATP molecule has been shown to kinetically inhibit its aggregation, but the mechanism via which the inhibition is mediated is not completely known (35).

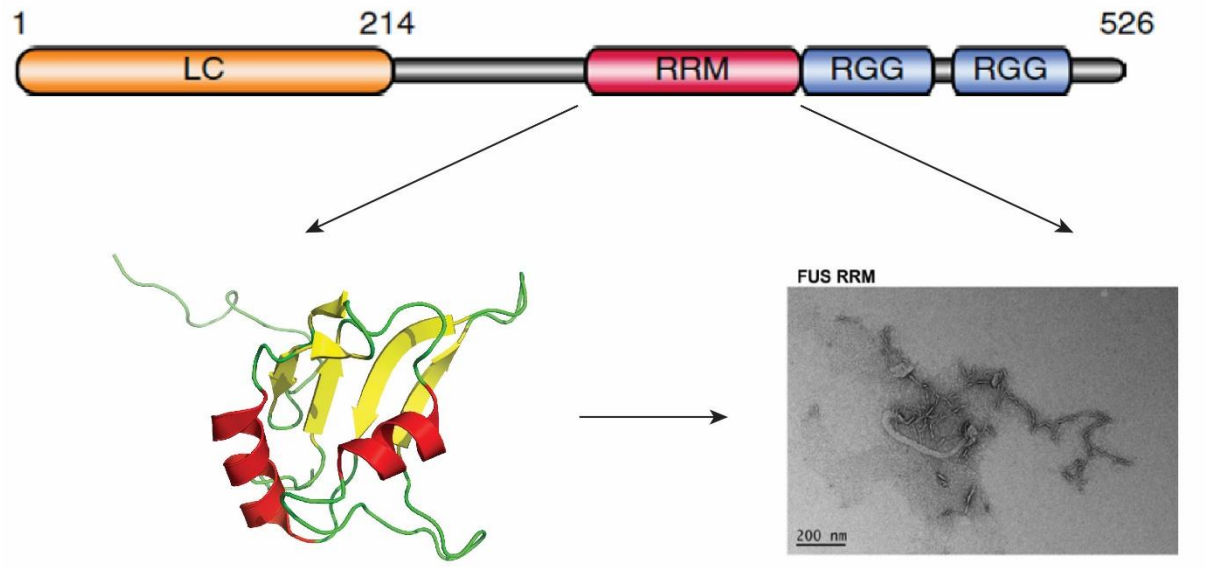

Figure 1.4. Domain organization of FUS and the tertiary structure of its RRM (278-385, PDB ID 2LCW), which forms fibrils in solution. Adapted from (33).

1.6 Protein dynamics

Proteins operate synergistically to preserve the dynamic equilibria in the cells (36-38). The concept of the free energy landscape of protein folding can also be extended to explain the dynamics of the protein. This has been extensively shown by multiple studies (39-42). In the context of biological macromolecules, proteins exhibit side-chain rotations, ligand binding, folding, catalysis, allostery, etc. (Figure 1.5). These occur on a range of timescales, encapsulating picoseconds to nanoseconds (ps-ns) to seconds (s). These motions can easily be captured with different techniques; however, nuclear magnetic resonance (NMR) spectroscopy is one of the best techniques to obtain atomic-level information about protein conformational dynamics.

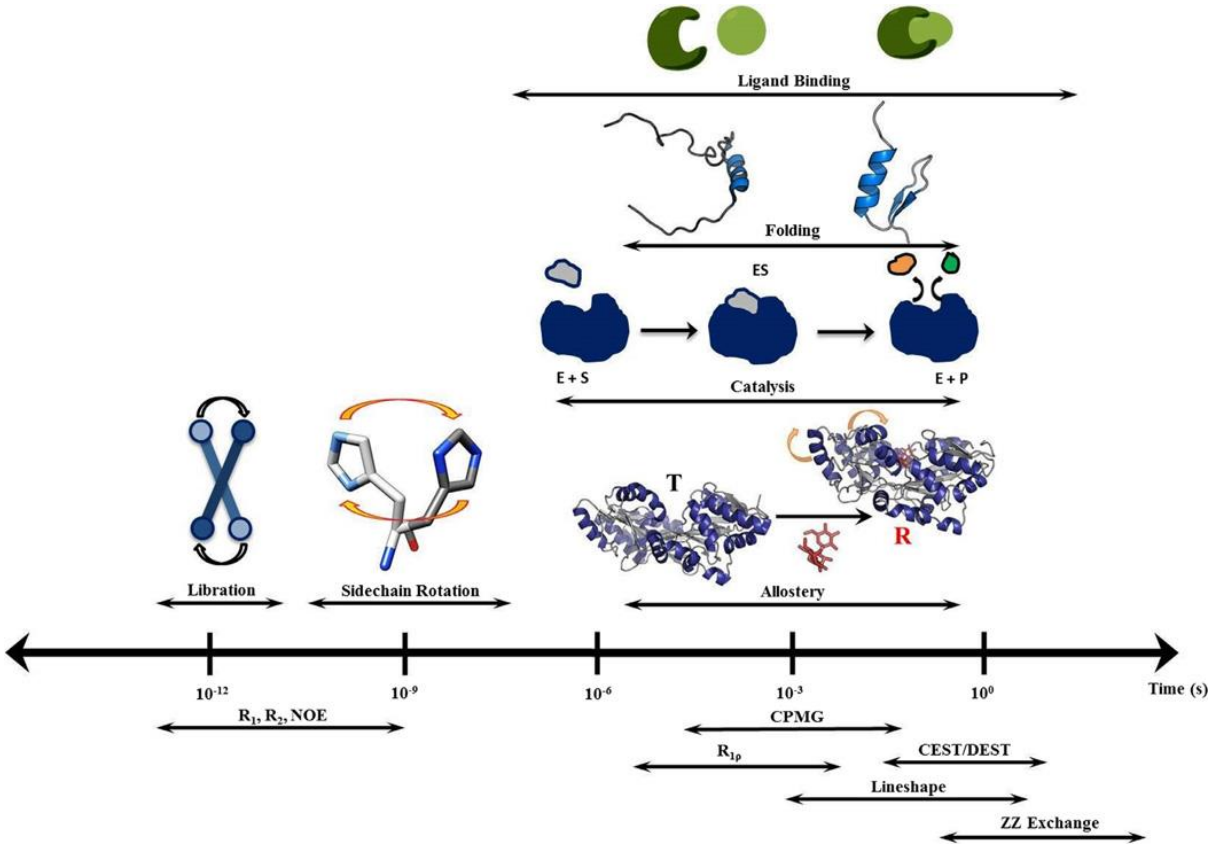

Figure 1.5. Protein dynamics across timescales. The X-axis represents different timescales over which protein motions are observed ranging from femtoseconds to seconds. NMR techniques to capture such timescales are listed at the bottom and provide useful insights into protein's conformations and functions. Adapted from (43).

Multi-tier dynamics can explain the conformational changes relevant to protein function (Figure 1.6). The change in external conditions (s) can affect the dynamics and the free energy landscape, which may shed some light on the role of protein conformers in cellular function. Let's consider a simple two-state system where state A and state B are present and are interconverting with each other, where state B is involved in salt-bridge interactions. State A is the major population, and state B is the minor population. Now, during a biological process, such as ligand binding, it is possible that the states are altered, and it shifts the population, which is represented by a light blue curve in (Figure 1.6). After ligand binding, state A becomes the minor population, and state B is now the major population. Since state B is involved in salt-bridge interaction, a higher population of state B leads to enhanced aggregation within a cell. Therefore, it is crucial to know about the thermodynamics of minor population(s) and the kinetics of their interconversion with major population during various stresses in the cell.

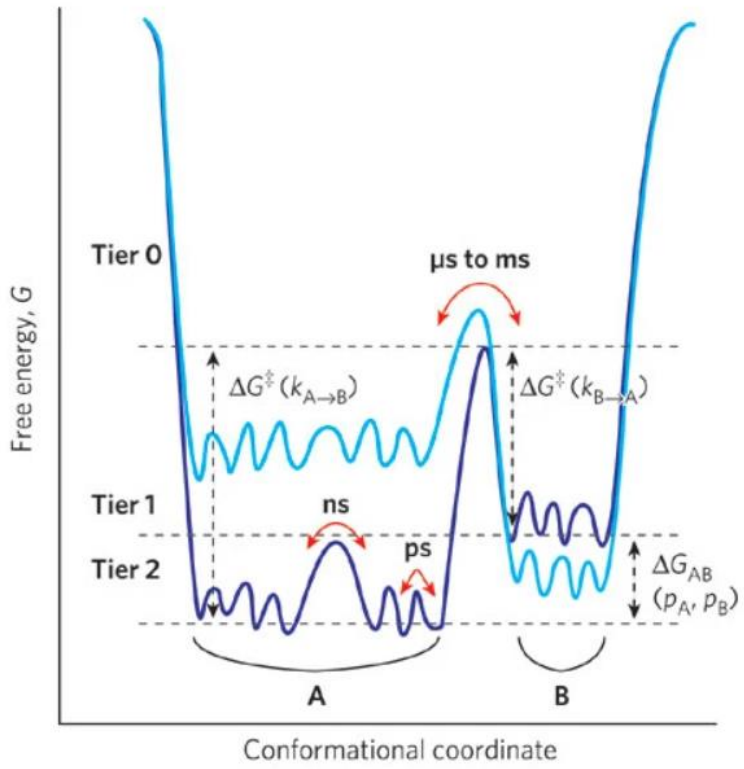

Figure 1.6. Multi-tier dynamics of a folded protein. The populations of the tier-0 states A and B (p_A, p_B) are defined as Boltzmann distributions based on their difference in free energy (ΔG_{AB}). The barrier between these states ($\Delta G^{\ddagger}$) determines the rate of interconversion (k). Lower tiers describe faster fluctuations between a large number of closely related substates within each tier-0 state. A change in the system will alter the energy landscape (from dark blue to light blue, or vice versa). Adapted from (41).

1.7 Chemical exchange and dynamic processes in NMR

Chemical exchange and conformational changes may lead to a perturbation in the chemical shift of the nucleus or its intrinsic traverse relaxation rate constant (R_2) involved in the change (Figure 1.7). This changes the NMR spectrum and causes either change in the NMR line position or line broadening. The exchange is often affected by temperature, pH, salt, etc., and thus can be used to study thermodynamics and kinetics. Major advancements in the NMR methodologies have led to different tools that can capture motions from picoseconds to seconds. These motions in proteins are related to numerous biological functions, from side-chain rotation of methyl groups to ligand binding, protein folding, etc.

In the simplest case, when a nucleus is exchanging between two states A and B with rate constants k_{AB} and k_{BA},

$$\frac{p_B}{p_A} = \frac{k_{AB}}{k_{BA}}, \qquad \text{eq 1.1}$$

$$p_A = 1 - p_B \qquad \text{eq 1.2}$$

where, p_A is the population of the ground state and p_B is the population of the excited state.

k_{ex} (exchange rate) is equal to $k_{AB}+k_{BA}$.

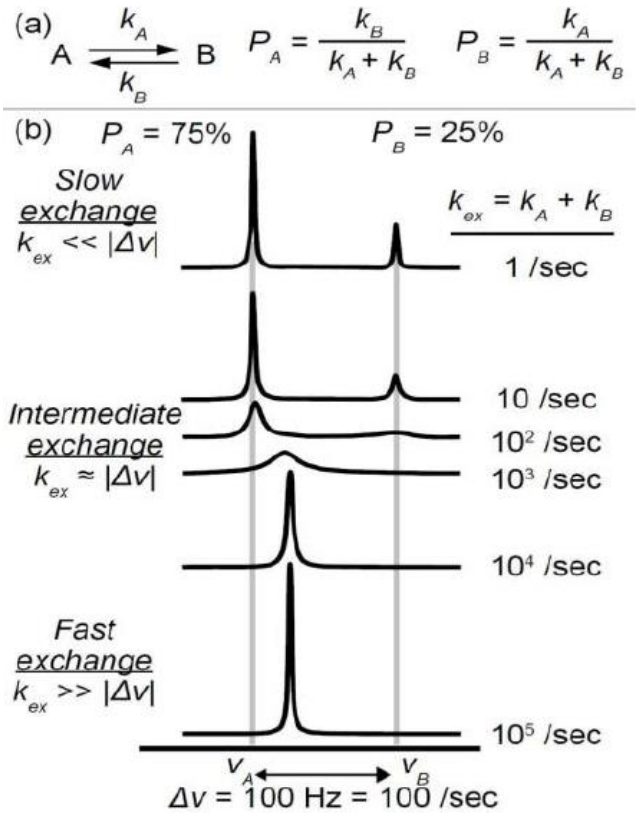

Figure 1.7. Chemical exchange processes can affect the NMR spectra. (a) Thermodynamic and kinetic parameters as depicted for a two-state exchange process. (b) The effect of varying k_{ex} vs chemical shift difference ($\Delta v = \upsilon_A - \upsilon_B$) between the two states. k_{ex} is the exchange rate between two populations. k_A and k_B are the forward and reverse rate constants. Adapted from (44).

- Slow exchange: When $k_{ex} << \upsilon_A - \upsilon_B$, the chemical shift difference between two states (in Hz), then two distinct sharp separate peaks are observed in the spectrum at the chemical shift of the nucleus in the two states, whose intensities are modulated by respective populations
- Intermediate exchange: when $k_{ex} \sim \upsilon_A - \upsilon_B$ (in Hz), then one broad peak is observed in the spectrum.
- Fast exchange: when $k_{ex} >> \upsilon_A - \upsilon_B$ (in Hz), then one sharp single peak is observed in the spectrum. The observed chemical shift is the average of two chemical shifts for the nuclei in two states. Exchange can cause line broadening without splitting the peaks

resulting in one broad peak with respect to other sharp peaks in the spectrum. Sometimes the intensity of this broad peak can be so low that it can hide into the noise.

There are multiple ways of detecting minor population, how it has been carried out for FUS-RRM will be covered in subsequent chapters.

1.8 Biophysical techniques to study protein conformations

1.8.1 Circular dichroism (CD) spectroscopy

Circular dichroism (CD) spectroscopy is a widely used technique to examine the structure and conformational changes of proteins. It is commonly used to monitor the secondary structure of proteins in the far-UV region (250-170 nm), and the tertiary structure of proteins in the near-UV region (300-160 nm). It exploits the differential absorption of right and left circularly polarized light by amides or carbonyls of the protein backbone. This differential absorption leads to characteristic CD spectra for the structural elements. For example, α-helical proteins typically exhibit negative CD bands at 222 nm and 208 nm and well-defined antiparallel β-pleated sheets (β-helices) have negative CD bands at 218 nm (Figure 1.8) (45). Proteins with disordered structures, on the other hand, generally display very low ellipticity above 210 nm and negative bands near 195 nm (45). Since temperature, pH, mutations, or ligand binding can change the structure of proteins, CD spectroscopy has been used to monitor conformational changes induced due to the same. While CD does not give residue-specific information on conformational changes, NMR and X-ray crystallography are used to gain such atomic insights.

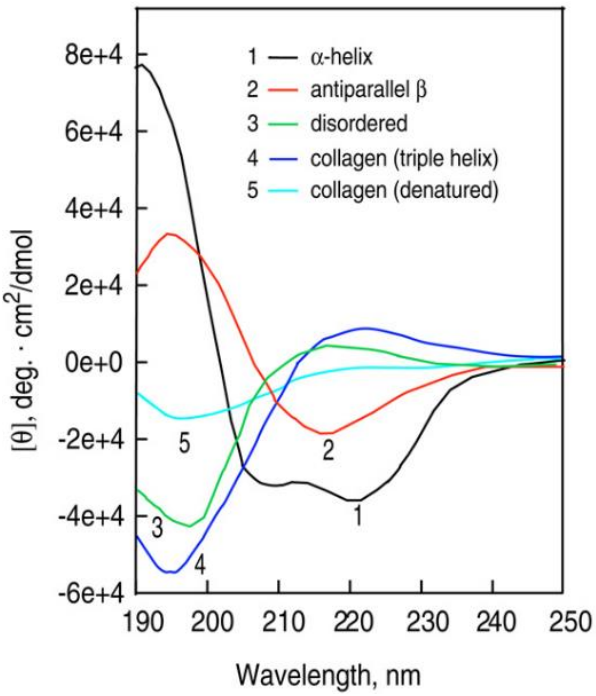

Figure 1.8. Standard far-UV CD spectra corresponding to specific secondary structures of proteins. Adapted from (45).

1.8.2 Fluorescence spectroscopy

Fluorescence spectroscopy is one of the most widely used techniques for studying protein conformations. For proteins, tyrosines, phenylalanines, and tryptophan residues provide intrinsic characteristics of fluorescence. The absorption and emission spectra of these amino acids have been depicted in (Figure 1.9). Tryptophan emission is the dominant one when compared to tyrosine and phenylalanine. In aqueous solutions, the emission peak of tryptophan typically occurs around 350 nm. The sensitivity of tryptophan's fluorescence to its local environment is one of its most valuable features. When tryptophan is in a more polar environment (e.g., water), its emission spectrum is generally red-shifted (longer wavelength). However, in an apolar or hydrophobic environment, the emission peak shifts to a shorter wavelength (blue-shift), providing insight into the protein's structural state or microenvironment. Alternatively, extrinsic fluorescence probes can also be introduced to probe a variety of fluorescence properties. Its application is useful for gaining information about protein dynamics and global structural information but most often it is used to monitor protein unfolding (46), ligand-binding (47), and protein-protein interactions (48).

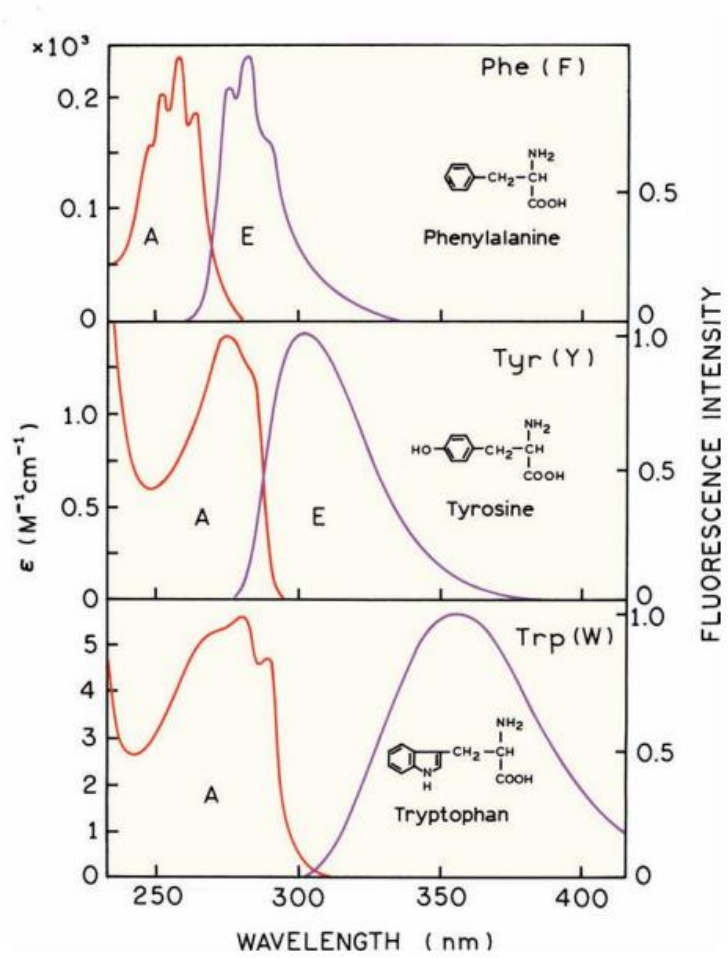

Figure 1.9. Absorption (A) and emission (E) spectra of aromatic amino acids: Phenyl Alanine, Tyrosine and Tryptophan at pH 7.0 in aqueous solution. Adapted from Principles of fluorescence spectroscopy, Joseph R. Lakowicz.

1.8.2.1 8-anilino-1-naphthalenesulfonic acid (ANS) fluorescence

8-anilino-1-naphthalenesulfonic acid (ANS) is a hydrophobic compound that binds to proteins, especially that are partially unfolded or have exposed hydrophobic patches. Upon binding it undergoes a change in fluorescence with a shift towards blue wavelength. This property makes ANS fluorescence useful for studying protein folding and conformational changes (49). The structure of ANS (Figure 1.10) suggests that it can interact primarily with aromatic-aromatic interactions through the sulfonate group by hydrogen bonding.

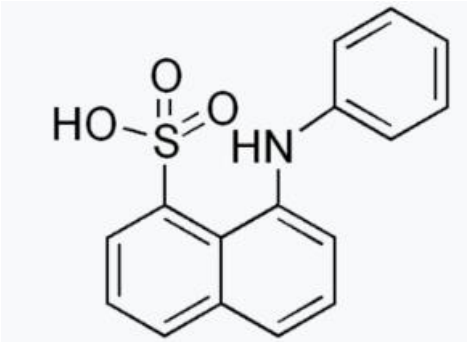

Figure 1.10. Molecular structure of ANS.

1.8.3 Size exclusion chromatography – multi-angle light scattering (SEC-MALS)

Size exclusion chromatography – multi-angle light scattering (SEC-MALS) measures the weight-average molecular weight of macromolecules in solution using the scattered intensity as it elutes from the SEC column (Figure 1.11) (50). It can distinguish oligomers (51) or higher order assemblies from monomers using refractive index (RI) and ultra-violet (UV) detectors with molecular weight ranging from 200 Da to 1 GDa. It can also determine the radius of gyration R_g from 10 nm to 500 nm. Therefore, combining molar mass and size, it can give information about the molecular conformation.

When laser light hits a macromolecule, it induces a dipole which acts as a source of secondary radiation, emitting light at the same frequency but with varying intensity. The size and shape of the macromolecule can affect the scattered intensity. For simplicity, the basic equation governing for a solution of isotropic scatterers (typically $R_g < 10$ nm) is,

$$I_{\text{scattered}} \propto M_{\text{w}} c \left(\frac{\mathrm{d}n}{\mathrm{d}c}\right)^2 \qquad \text{eq 1.3}$$

where, $I_{scattered}$ is the total intensity of scattered light, the parameter that is actually measured by the detectors, M_w is the weight-average molecular weight, c is the concentration of the macromolecule, and dn/dc is the specific refractive index increment of the macromolecule in the solvent. This equation does not consider the angular dependence and other types of interactions but is simplified enough to understand the basic principles of light scattering.

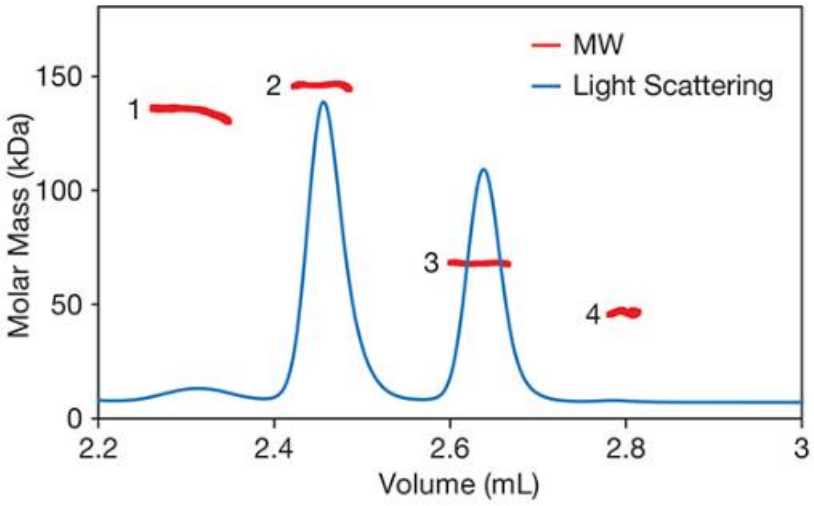

Figure 1.11. Elution profile of macromolecules with respective M_w determined by MALS. The different molecular weights (red) for proteins eluted at different times (blue) have been depicted. Adapted from https://www.wyatt.com/.

1.8.4 Atomic force microscopy (AFM)

Atomic force microscopy (AFM) is an essential tool for surface analysis. It can image nanoscale structures and can also evaluate many physical properties of the material. An AFM consists of three separate subsystems i) sensors, ii) detectors, and iii) positioners (Figure 1.12). These are controlled by a computer. The AFM sensor is the cantilever with a sharp tip near the free end. When it is near the surface, the tip is affected by the force, either deflected or attracted. This movement is optically detected using a laser and a photodetector. The actuators are the piezoelectric device which changes the relative positions of the sample and the cantilever. The most common type of AFM measures the topography of the system that is height. There are various modes to capture AFM images, including tapping mode, x mode, y mode, etc., but the tapping mode has its own advantages (52). In tapping mode, the cantilever is oscillated with an external application of force (typically less than 100 pN) causing it to vibrate up and down. The tip scans across the sample by intermittently contacting the surface. This results in a change of amplitude and phase of the oscillation causing to generation of high-resolution images. Due to the feedback loop, the instrument maintains a constant amplitude of oscillation resulting inconsistent imaging conditions. Because the tip makes intermittent contact with the surface there is reduced friction and is useful for soft biological samples. AFM can visualize the 3D structure of proteins providing size, shape, and surface features. It can be used to monitor aggregates and protein complexes. AFM can also monitor conformational changes of proteins in response to external stimuli such as pH (53), temperature (54), ionic strength (55), etc.

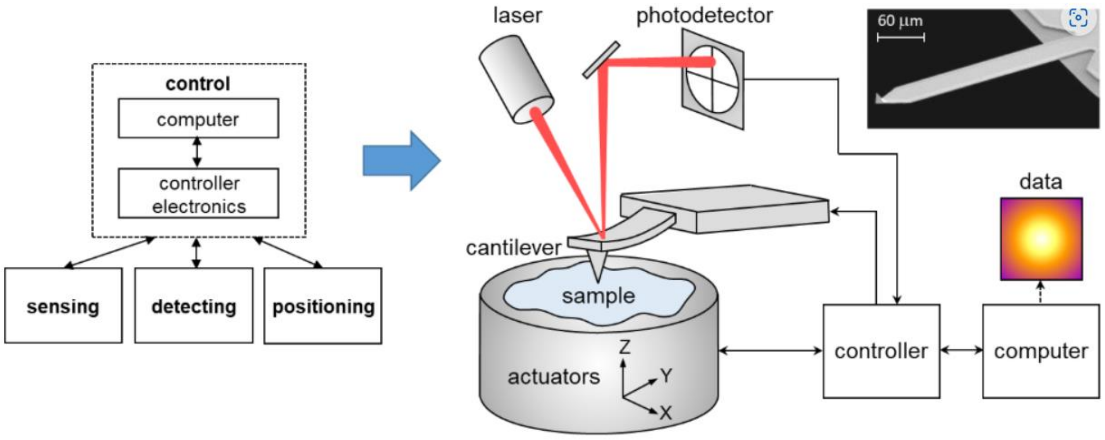

Figure 1.12. Components of the atomic force microscope (AFM) system. Adapted from https://afm.oxinst.com/outreach/atomic-force-microscopy.

1.8.5 Transmission electron microscope (TEM)

Transmission electron microscope (TEM) produces images by illuminating a thin sample with an electron beam in a high vacuum. The TEM can reveal detailed micro-structural arrangements with high magnification (56). The components of a TEM are shown in (Figure 1.13). The electron-producing gun is located at the top which passes electrons down the column through a series of electromagnetic lenses reaching the sample and then to an image collector at the bottom. After hitting the sample some electrons are stopped or deflected by the sample. The transmitted electrons are collected by the screen or camera producing dark or bright images where electrons do not pass through or where it is unscattered, respectively.

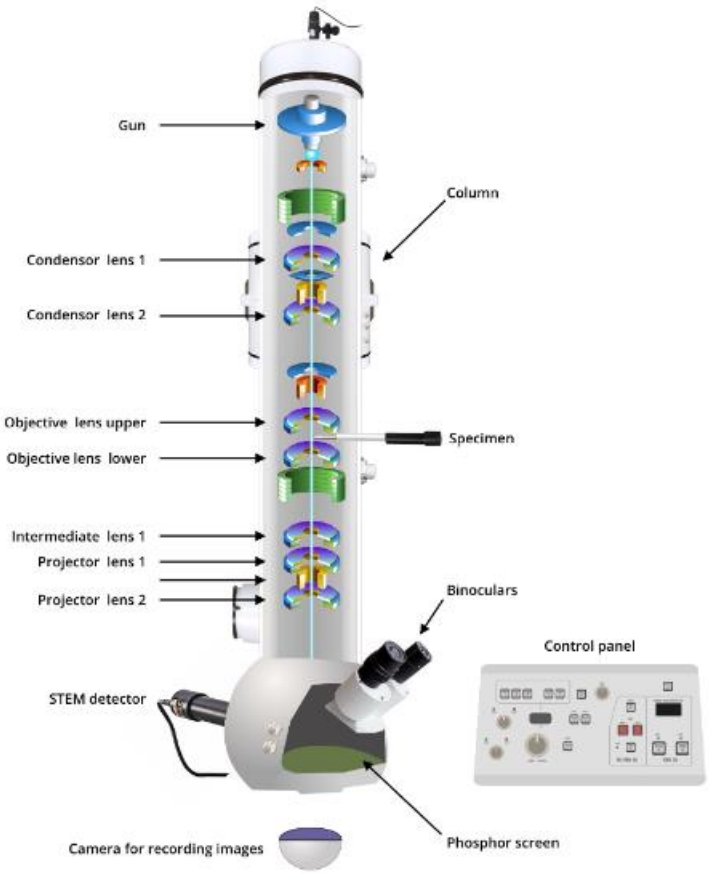

Figure 1.13. Components of the transmission electron microscope (TEM) system. Adapted from https://myscope.training/TEM_Instrument_design.

TEM produces higher-resolution images than the light microscope because the wavelength of the electron is much smaller than that of the visible light. Resolution is defined as,

$$d = \frac{0.61\lambda}{n\sin a} \qquad \text{eq 1.4}$$

where, d is the distance between two points, λ is the wavelength, n is the refractive index and a is the angular aperture. The wavelength (λ) of an electron is related to the accelerating voltage and is approximated by,

$$\lambda = \frac{h}{\sqrt{2meV}} \qquad \text{eq 1.5}$$

where, h is Planck's constant, m is the mass of an electron, e is the electric charge and V is the accelerating voltage. Thus,

$$\lambda \sim \sqrt{\frac{1.5}{V}} \qquad \text{eq 1.6}$$

Thus, the higher the accelerating voltage, the smaller the wavelength and hence greater the resolution. Electron microscopy with its unique capability provides direct visual information of size, shape, and aggregation conditions of a wide range of samples from nanoparticles (57), cell organelles (58) to protein therapeutics (59), (60), and many others.

1.8.6 Nuclear magnetic resonance (NMR) spectroscopy

Nuclear magnetic resonance (NMR) spectroscopy uses the magnetic properties of certain nuclei (^{1}H, ^{13}C, ^{15}N, ^{19}F, ^{31}P, etc.), as charges with non-zero spin angular moment produce magnetic fields. NMR spectroscopy is routinely used to study small, large, and complex biomolecules (61, 62). In solution NMR, typically 0.2-0.6 mL of 0.1-5 mM sample is loaded in an NMR tube. This when placed in a strong magnetic field e.g. 14.1 Tesla (600 MHz) leads to the precession of the nuclei in a cone, like a spinning top in the earth's gravitational field. The rate of precession is dependent upon the strength of the external magnetic field B_0 and the strength of the nuclear magnet γ, as given by the equation,

$$\nu_0 = \frac{\gamma B_0}{2\pi} \qquad \text{eq 1.7}$$

where, ν_0 is the Larmour frequency, γ is the gyromagnetic ratio and B_0 is the external magnetic field.

In a quantum mechanical picture, these spin ½ nuclei are arranged in two states α, a low-energy state parallel to B_0, and β, a high-energy state anti-parallel to B_0. At thermal equilibrium, a large population of nuclei will reside in the low-energy state while slightly less will reside in the high-energy state. Nuclei in the low-energy state may be promoted to the high-energy state upon irradiation by a electromagnetic wave with energy equal to the energy gap between the two states, and this corresponds to the frequency of electromagnetic radiation. For a given temperature and B_0 the Boltzmann distribution of population difference is given by,

$$\frac{N_\alpha}{N_\beta} = \exp\left(\frac{\Delta E}{k_B T}\right) \text{ where } \Delta E = \gamma B_0 \hbar \quad \text{eq 1.8}$$

where, N_α and N_β are the populations of the low and high-energy states, k_B is the Boltzmann constant, T is the absolute temperature, ΔE is the energy gap, γ is the gyromagnetic ratio, B_0 is the external magnetic field, and ħ is the reduced Planck's constant. For the B_0 field of 14.1T and at 298K, the ratio between N_α and N_β is,

$$\frac{N_\alpha}{N_\beta} = 1.000097 \qquad \text{eq 1.9}$$

Thus, there is a very small difference between the two states and that is why NMR is an insensitive technique compared to other spectroscopic techniques. The individual magnetic moments of the nuclei result in net magnetization in +z direction (direction of B_0) after the longitudinal relaxation. This net magnetization M_0 is the useful quantity that we measure in NMR. The z-component of M_0 is equal to,

$$M_z^0 = \gamma^2 \hbar^2 N \frac{B_0}{4k_B T} \qquad \text{eq 1.10}$$

where M_z^0 is the net longitudinal magnetisation, N is the number of identical spins in the sample, k_B is the Boltzmann constant, T is the absolute temperature, B_0 is the external magnetic field, γ is the gyromagnetic ratio, and $\hbar$ is the reduced Planck's constant.

For NMR experiments to work, this M_z^0 is perturbed by the application of a 90° radiofrequency (RF) pulse which brings the M_0 into the transverse plane, where it undergoes oscillations and a free-induction decay (FID) is detected while it returns to the thermal equilibrium state. This process is called relaxation and will be discussed later.

The fundamental observable in modern NMR spectrometers is the FID (Figure 1.14). This is a time-dependent induced and detected current in the receiver coil by all the precessing nuclei in the sample. The observed FID is a mixture of all the individual FIDs for each nucleus with a characteristic frequency. The FID decays over time in an exponential fashion due to loss in coherence. The rate of this decay can be quantified by the transverse relaxation rate constant R_2. The FID is then Fourier transformed (FT) from the time domain to the frequency domain to obtain important information such as chemical shift, intensity, and linewidth.

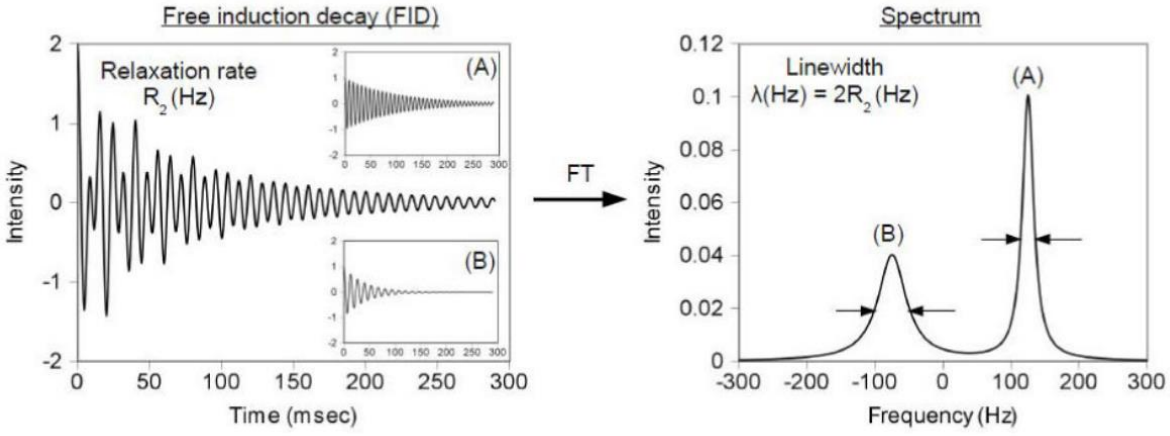

Figure 1.14. FID profile that encapsulates decaying signals from all the nuclei in the sample which is Fourier transformed (FT) on the right to give information about the chemical shift, intensity, and linewidth of each nucleus. Adapted from (44).

The Chemical Shift

Each nucleus in a molecule is bonded to other nuclei or interacts with other nuclei via non-covalent interactions, all of which results in a slightly different resonant frequency for the nucleus under study than its Larmour precession frequency. This number, when expressed in parts per million, is called the chemical shift and is the useful entity that provides detailed information about the molecule. Each peak in the NMR spectrum represents the unique chemical shift of the molecule. The chemical shift is affected by the pH, temperature, etc. which shifts it to downfield or upfield in the spectrum.

Intensity

Intensity represents the height or the area/volume under the peak. It can give information about the number of nuclei contributing to the observed signal and thus help quantify the signals. This is a dimensionless quantity and is compared relative to other signals in the spectra.

Linewidth ($v_{1/2}$)

It is defined as the full peak width at half of the maximum height. It reports on the transverse relaxation rate and gives information about the dynamic properties of the molecule. The broader peak corresponds to increased transverse relaxation rate in the NMR spectra, suggesting the nucleus under observation is affected by the phenomenon of chemical/conformational exchange.

$$v_{1/2} = \frac{R_2}{\pi} = \frac{R_2^{int} + R_{ex}}{\pi} \qquad \text{eq 1.11}$$

where, R_2 is the transverse relaxation rate, R_2^{int} is the intrinsic transverse relaxation rate, and R_{ex} is the relaxation rate due to chemical/conformational exchange.

1.8.6.1 Basic steps in the NMR experiment

The NMR experiment involves a combination of specific types of radio frequency (RF) pulses applied for specific durations at different powers and various delays before the FID is measured. Higher dimensional NMR experiments bring more complexity to their execution but can be simply characterized with building blocks of four basic steps:

1) **Recovery step** (or inter-scan delay): This period corresponds to the return of the net magnetization and population back to its thermal equilibrium. This is generally determined by the longitudinal relaxation rate (R_1) with the guideline of (3-5)/R_1.
2) **Preparation step**: This step is used to select nuclei and prepare different types of magnetizations such as single quantum (SQ), multiple quantum (MQ), zero quantum (ZQ), or double quantum (DQ) coherences. These provide independent measures of various relaxation properties at different timescales.
3) **Evolution step**: This step permits the evolution of additional time-dependent phenomena such as chemical shift evolution of an attached nucleus X. This is achieved using incremented delay to indirectly sample the FID of the attached nucleus and thus adds one more dimension to the NMR data, however, it also increases the measurement time.
4) **Detection step**: This step directly records the FID which contains information on the time-dependent intensities as modulated by the first three steps.

1.8.6.2 Spin relaxation

Spin relaxation is the process by which nuclear spins return to thermal equilibrium after being perturbed by an external magnetic field (63). It is caused by the fluctuations in the magnetic field to nearby nuclei through interactions between spins and their surroundings. These fields change in time (because of the molecules tumbling in solution) and induce random transitions between the NMR spin states, and these random transitions lead to decay of magnetisation back to equilibrium. The efficiency of relaxation depends on factors such as, molecular tumbling, the correlation times, and the frequency of the applied field (Larmour frequency). It is an important aspect of NMR and influences the experimental time as well as the spectral quality, including impact on linewidth. The relaxation times T_1 and T_2 are key to understanding molecular dynamics in NMR and provides information about the amplitude and timescale of motions (61).

1.8.6.2.1 Longitudinal relaxation (T_1)

Longitudinal relaxation (T_1) is defined as the growth of the z-magnetisation, M_z, to its initial value M_0, after an RF pulse, after time τ. The equation for T_1 is given as,

$$M_z = -M_0\left(1 - e^{-\frac{\tau}{T_1}}\right) \qquad \text{eq 1.12}$$

The z-magnetization grows from 0 to 63% after one T_1 and to 99% after 5 times T_1. So, it is a useful practice to wait for time $5*T_1$ after one scan is finished to reach the equilibrium value again and then acquire the next scan to obtain a reliable data. Thus, T_1 actually determines how rapidly we can obtain NMR data. Longitudinal relaxation is also known as spin-lattice relaxation, and thermal relaxation.

T_1 is typically measured using a simple 180°–τ–90° inversion recovery pulse sequence. The longitudinal net magnetization is first inverted with a 180° pulse, flipping M_z to $-M_z$. After delay time τ, 90° pulse rotates the partially recovered magnetisation into the transverse plane for signal detection. By varying τ, a series of experiments are recorded. For $\tau = 0$, the signal is maximally negative due to full inversion, as it is increased, signal passes through zero and then becomes positive. For longer τ value, the spectrum looks like a normal spectrum. The resulting signal intensities are then fitted to an exponential function to extract T_1.

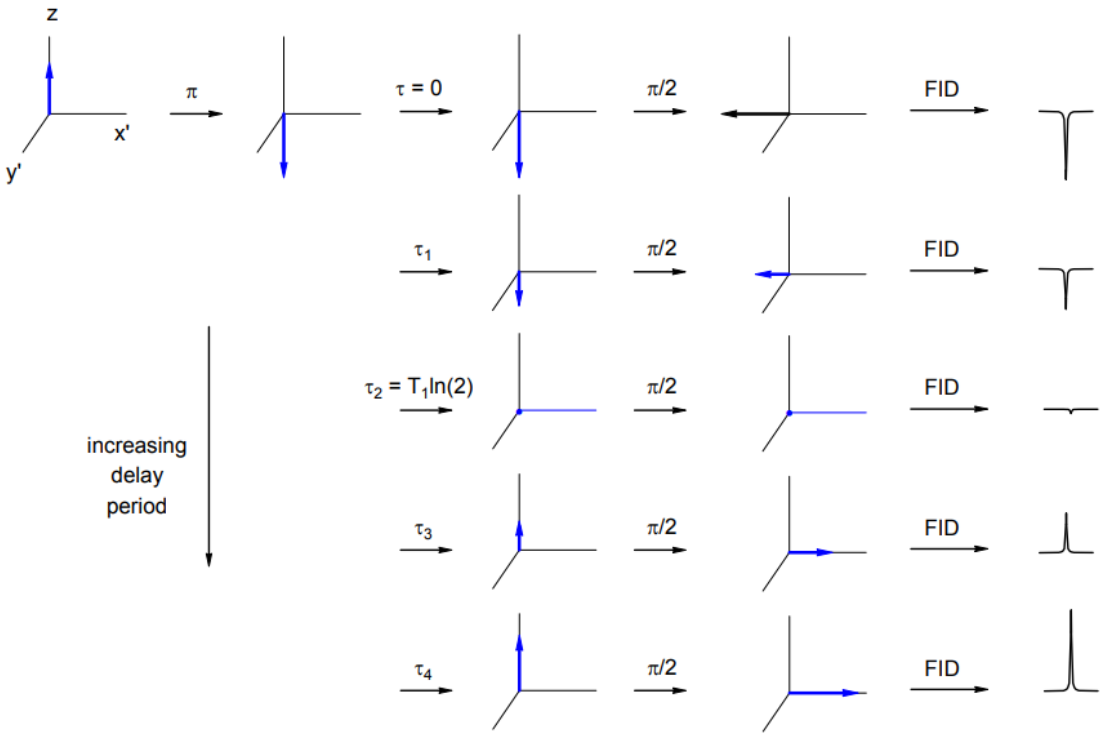

Figure 1.15. T_1 relaxation process. It shows the process of T_1 relaxation after a 180° RF pulse. The z component of the net magnetisation, M_z is reduced to zero, but then recovers gradually back to its equilibrium value. Adapted from https://www.chem.wisc.edu/areas/reich/nmr/notes-8-tech-1-relax.pdf

1.8.6.2.2 Transverse relaxation (T_2)

Transverse relaxation (T_2) is defined as the loss of coherence in the x-y plane after a 90° RF pulse. The loss of coherence is caused by the magnetic field inhomogeneity and due to chemical exchange. These effects result in phase differences, which lead to a decrease in the net magnetization in the x-y plane. The result is an exponential decay and is represented as,

$$M_y = -M_0 \cos(2\pi v_0 \tau) e^{-\frac{\tau}{T_2}} \qquad \text{eq 1.13}$$

$$M_x = M_0 \sin(2\pi v_0 \tau) e^{-\frac{\tau}{T_2}} \qquad \text{eq 1.14}$$

where, M_y and M_x are the net magnetisation in the x-y plane, v_0 is the frequency, and τ is the delay time.

The decaying exponential represents the fanning out of magnetization and after $0.693*T_2$, the magnetization reduces to half of its original value. When $\tau = T_2$, we would see only 36.8%(e^{-1}) magnetization of its original value after a 90° RF pulse. Transverse relaxation is also known as spin-spin relaxation.

To determine T_2, the standard pulse sequence employed is the spin-echo sequence 90°-τ-180°-τ-FID. After 90° pulse, transverse magnetisation is created, which starts to dephase due to field inhomogeneities and exchange processes. An 180° pulse causes the refocusing of spins, leading to the formation of an echo at time 2τ. By varying τ, a plot of echo amplitude (peak height) versus total echo time (2τ) yields an exponential decay, which is fitted to extract the transverse relaxation time T_2.

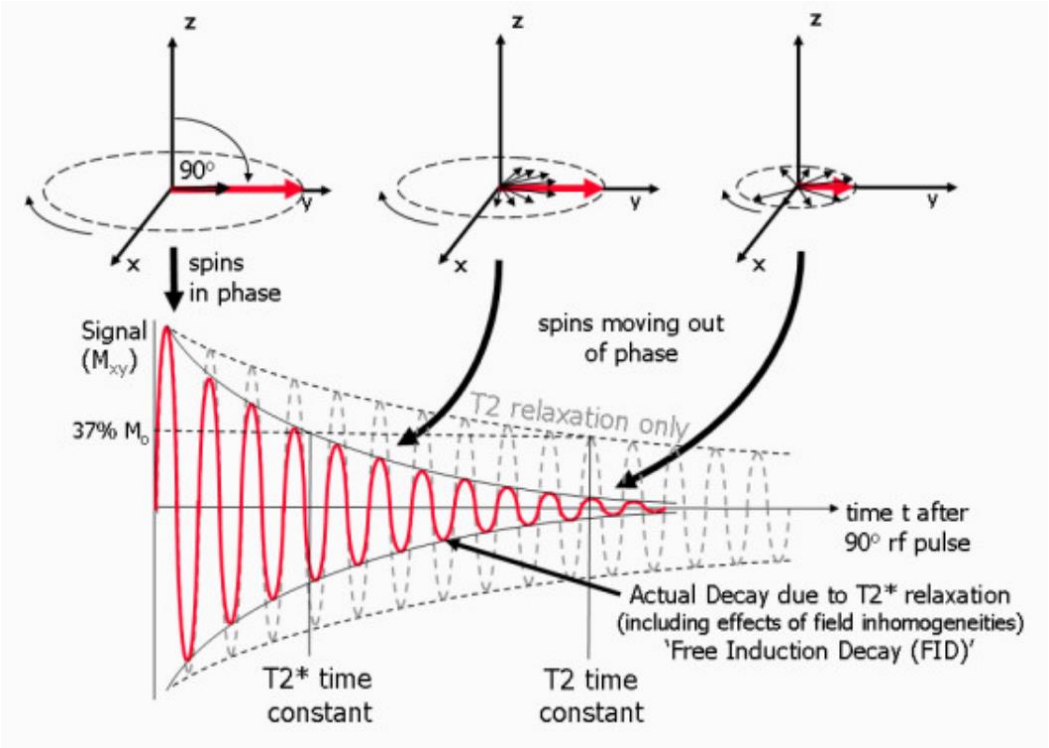

Figure 1.16. T_2 relaxation process. T_2 is an instrumentally dependent parameter and it determines the line width of an NMR resonance. T_2, on the other hand, is a physically meaningful parameter independent of field inhomogeneity, J coupling and other factors. T_2 is always greater than T_2*. Adapted from (64).*

1.8.6.2.3 Nuclear Overhauser Effect (NOE)

Nuclear Overhauser Effect (NOE) is another relaxation phenomenon. It involves irradiation of nuclei with continuous low-power RF pulse which causes saturation of the two states and hence decreases the signal in the spectrum. Spin transitions either due to ZQ, SQ, or DQ or combinations of them perturb the populations of the nearby nuclei (≤5Å), a process called as cross-relaxation. It is defined as a process in which magnetization is transferred between two different spins due to dipolar coupling, leading to zero, positive, or negative NOEs, and is useful for determining spatial proximity. In contrast, self-relaxation affects the same nucleus due to local fluctuating fields, primarily governed by T_1 and T_2, and is useful for understanding local dynamics. The NOE gives distance information of the nearby nuclei and hence is widely used to gain the 3D structure of the molecule.

A simple NOE experiment would involve a selective 180° pulse which causes the spins to be out of equilibrium and transfers the magnetisation to other spins through cross-relaxation. The NOE enhancement factor, η, is defined as,

$$\eta = \frac{I - I_0}{I} \qquad \text{eq 1.15}$$

Another situation involves irradiating one spin with a very weak RF pulse for long enough so that it is saturated (no net magnetisation). The simultaneous process of self-relaxation and cross-relaxation leads to steady-state NOE, where the population difference of one spin becomes zero. The NOE enhancement factor η_{SS} is defined as,

$$\eta_{SS} = \frac{\sigma_{IS}}{R_I}\frac{S_z^0}{I_z^0} \qquad \text{eq 1.16}$$

where, σ_{IS} is the cross-relaxation rate, R_I is the longitudinal relaxation rate of I spin, S_z^0 and I_z^0 are the equilibrium z-magnetisation of S and I spins respectively. The size of NOE enhancement gives information about spatial proximity and/or local flexibilty.

1.8.6.2.4 Dipole-dipole relaxation in liquids

For a pair of nuclei *ij* the magnetic field around nucleus *i* will be affected due to dipolar field of nucleus *j*. The dipolar interactions are caused by the magnetic flux lines affecting the magnetic field at another nucleus. The strength of the interaction is dependent upon the internuclear distance and on the orientation of the spin *i* relative to the B_0. The dipolar interaction is expressed as follows:

$$D^{ij} = -\frac{\mu_0 \hbar \gamma_i \gamma_j}{4\pi^2 r_{ij}^3}\left\langle\frac{(3\cos^2\theta - 1)}{2}\right\rangle = D_{max}^{ij}\left\langle\frac{(3\cos^2\theta - 1)}{2}\right\rangle = D_{max}^{ij}\langle P_2(\cos\theta(t))\rangle \qquad \text{eq 1.17}$$

where θ is the angle between the internuclear vector relative to the B_0, r is the internuclear distance, and μ_0 is the permittivity of free space. For solution NMR, especially for proteins, the dipolar couplings are averaged out due to isotropic motion of the molecules.

This dipolar interaction is one the mechanisms for relaxation. Following equations describe the relaxation rate due to dipole-dipole interactions,

$$\frac{1}{T_1^i} = \frac{1}{10}\left(\frac{\mu_0}{4\pi}\right)^2 \frac{\gamma_i^2\gamma_j^2\hbar}{r^6}\left(\frac{3\tau_c}{1+\omega_i^2\tau_c^2} + \frac{6\tau_c}{1+(\omega_i+\omega_j)^2\tau_c^2} + \frac{\tau_c}{1+(\omega_i-\omega_j)^2\tau_c^2}\right) \qquad \text{eq 1.18}$$

$$\frac{1}{T_2^i} = \frac{1}{20}\left(\frac{\mu_0}{4\pi}\right)^2 \frac{\gamma_i^2\gamma_j^2\hbar^2}{r^6}\left(4\tau_c + \frac{3\tau_c}{1+\omega_i^2\tau_c^2} + \frac{6\tau_c}{1+\omega_j^2\tau_c^2} + \frac{6\tau_c}{1+(\omega_i+\omega_j)^2\tau_c^2} + \frac{\tau_c}{1+(\omega_i-\omega_j)^2\tau_c^2}\right) \qquad \text{eq 1.19}$$

$$\sigma_{ij} = \frac{1}{10}\left(\frac{\mu_0}{4\pi}\right)^2 \frac{\gamma_i^2\gamma_j^2\hbar^2}{r_{ij}^6}\left[\frac{6\tau_c}{1+(\omega_i+\omega_j)^2\tau_c^2} - \frac{\tau_c}{1+(\omega_i-\omega_j)^2\tau_c^2}\right] \qquad \text{eq 1.20}$$

For fast motion $\omega_i\tau_c << 1, \omega_j\tau_c << 1$

$$\frac{1}{T_1^i} = \left(\frac{\mu_0}{4\pi}\right)^2 \frac{\gamma_i^2\gamma_j^2\hbar}{r^6}\tau_c = \frac{1}{T_2^i} \qquad \text{eq 1.21}$$

$$\sigma_{ij}^{\text{fast}} \approx \frac{1}{2}\left(\frac{\mu_0}{4\pi}\right)^2 \frac{\gamma_i^2\gamma_j^2\hbar^2}{r_{ij}^6} \cdot \tau_c \quad \text{eq 1.22}$$

For slow motion, same nuclei (^{1}H-^{1}H) $\omega_i\tau_c >> 1$

$$\frac{1}{T_1^i} = \frac{1}{10}\left(\frac{\mu_0}{4\pi}\right)^2 \frac{\gamma_i^2\gamma_j^2\hbar}{r^6}\tau_c \quad \text{eq 1.23}$$

For slow motion, different nuclei (^{1}H-^{13}C) $\omega_i\tau_c >> 1, \omega_j\tau_c >> 1$

$$\frac{1}{T_1^i} = \frac{1}{10}\left(\frac{\mu_0}{4\pi}\right)^2 \frac{\gamma_i^2\gamma_j^2\hbar^2}{r^6\tau_c}\left(\frac{3}{\omega_i^2} + \frac{6}{(\omega_i+\omega_j)^2} + \frac{1}{(\omega_i-\omega_j)^2}\right) \quad \text{eq 1.24}$$

$$\frac{1}{T_2^i} = \frac{1}{5}\left(\frac{\mu_0}{4\pi}\right)^2 \frac{\gamma_i^2\gamma_j^2\hbar^2}{r^6}\tau_c \quad \text{eq 1.25}$$

$$\sigma_{ij}^{\text{slow}} = \frac{1}{10}\left(\frac{\mu_0}{4\pi}\right)^2 \cdot \frac{\gamma_i^2\gamma_j^2\hbar^2}{r_{ij}^6\tau_c}\left[\frac{6}{(\omega_i+\omega_j)^2} - \frac{1}{(\omega_i-\omega_j)^2}\right] \quad \text{eq 1.26}$$

where, μ_0 is magnetic permeability of free space, γ_i,γ_j are gyromagnetic ratios of nuclei *i* and *j* respectively (these represent how strongly each nucleus interacts with the magnetic field), *ħ* is reduced Planck's constant, r is the distance between the two nuclei. Since it's raised to the power of 6, the interaction is highly distance-dependent - relaxation is much stronger when nuclei are closer, τ_c is rotational correlation time (a measure of how fast the molecule is tumbling. Longer τ_c means slower motion (e.g., in larger molecules)), and ω_i,ω_j are Larmor angular frequencies of nuclei *i* and *j*, respectively.

1.8.6.2.5 Chemical Shift Anisotropy (CSA)

Besides dipolar interaction, CSA is another mechanism which restores the Boltzmann equilibrium. CSA depends on the orientation of the molecule, and as the molecule tumbles in solution this is also averaged out and the chemical shift can be represented by,

$$\delta_{\text{iso}} = \frac{1}{3}(\delta_{XX} + \delta_{YY} + \delta_{ZZ}) \quad \text{eq 1.27}$$

where δ_{XX}, δ_{YY} and δ_{ZZ} are the chemical shift tensors defined by axes X, Y and Z respectively.

Following equations describe the relaxation rate due to CSA,

$$\frac{1}{T_1} = \frac{2\Delta_{\text{CSA}}^2\omega_N^2}{15}\frac{\tau_c}{1+\omega_N^2\tau_c^2} \quad \text{eq 1.28}$$

$$\frac{1}{T_2} = \frac{\Delta_{\text{CSA}}^2\omega_N^2}{45}\left(4\tau_c + \frac{3\tau_c}{1+\omega_N^2\tau_c^2}\right) \quad \text{eq 1.29}$$

For fast motion $\omega_N\tau_c << 1$

$$\frac{1}{T_1} = \frac{2\Delta_{\text{CSA}}^2\omega_N^2\tau_c}{15} \quad \text{eq 1.30}$$

$$\frac{1}{T_2} = \frac{7\Delta_{\text{CSA}}^2\omega_N^2\tau_c}{45} \quad \text{eq 1.31}$$

For slow motion $\omega_N \tau_c >> 1$

$$\frac{1}{T_1} = \frac{2\Delta_{CSA}^2 \omega_N^2}{15} \frac{\tau_c}{\omega_N^2 \tau_c^2} = \frac{2\Delta_{CSA}^2}{15\tau_c} \quad \text{eq 1.32}$$

$$\frac{1}{T_2} = \frac{\Delta_{CSA}^2 \omega_N^2}{45} \left(4\tau_c + \frac{3}{\omega_N^2 \tau_c}\right) \approx \frac{4\Delta_{CSA}^2 \omega_N^2 \tau_c}{45} \quad \text{eq 1.33}$$

where Δ_{CSA} is the chemical shift anisotropy of the nucleus, ω_N is Larmor angular frequency of the ^{15}N, and τ_c is rotational correlation time. The factor $\frac{\tau_c}{1+\omega_N^2 \tau_c^2}$ is a spectral density function which tells how efficiently molecular tumbling at frequency ω_N contributes to relaxation.

1.8.6.2.6 Effect of molecular tumbling on relaxation

Due to spin interactions the individual magnetic moments that make up the magnetization experience slightly different local magnetic fields. These local fields fluctuate over time as the molecules tumble through solution leading to random transitions between the NMR spin states. For small molecules, the tumbling is relatively fast, and many molecules can efficiently transfer energy to the surrounding lattice at the Larmor frequency, leading to decrease in T_1 (Figure 1.17). This occurs fastest when molecule is tumbling exactly at Larmour frequency. And concomitantly it has the opposite effect when molecular size increases (τ_c increases). But T_2 always tends to decrease with an increase in the molecular weight. With an increase in the molecular weight, molecules tumble slowly and nuclei oscillate either slowly or faster than the average precession rate which leads to rapid de-coherence. T_2 determines how fast the FID decays, a short T_2 corresponds to a faster decaying FID and a long T_2 corresponds to a long FID. Since time-domain data is converted to frequency-domain data, it has the opposite effect i.e. for a short T_2, the peaks broaden, and for a long T_2, we obtain a sharp peak in the spectrum. Therefore, it becomes difficult to study larger molecules using NMR. Even for a perfectly shimmed magnet, the FID is determined by the T_2, which is determined by the tumbling process.

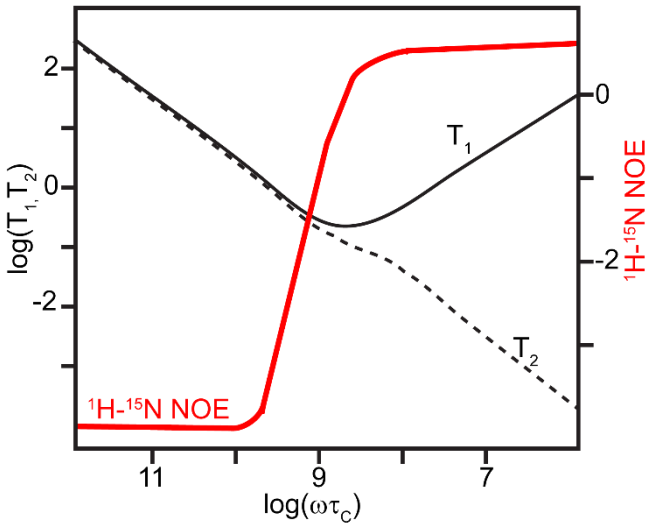

Figure 1.17. Plots of log(T_1 and T_2) and ^{1}H-^{15}N NOE vs log($\omega\tau_c$) for ^{15}N. Adapted from (69).

1.8.6.3 Heteronuclear adiabatic relaxation dispersion (HARD)

HARD method is used to characterize µs to ms dynamics (k_{ex}~ 10^4–10^6 s^{-1}), where dispersion in rotating frame relaxation rate constants (longitudinal $R_{1\rho}$ and transverse $R_{2\rho}$) is created by modulating the shape and duration of adiabatic full passage (AFP) pulses (65, 66). Adiabatic pulses are a special class of RF pulses that are used to achieve a uniform flip angle for all the resonances; that is, they are offset independent. These pulses are routinely used in NMR imaging to capture $R_{1\rho}$ and $R_{2\rho}$ rates. In addition, these adiabatic pulses are amplitude and frequency/phase modulated when compared to the normal square pulses.

For adiabaticity to be achieved, it is important that the following relation should hold true:

$$\left|\gamma B_{eff}(t)\right| \gg \left|\frac{d\alpha}{dt}\right| \qquad \text{eq 1.34}$$

where, γ is the gyromagnetic ratio, B_{eff} is the effective field, and $\left|\frac{d\alpha}{dt}\right|$ is the instantaneous angular velocity (rate) with α being the sweep (flip) angle. If the sweep rate is sufficiently slow so that the magnetization vector, M is continuously aligned with B_{eff} (Figure 1.18). If the condition is satisfied, then the net magnetisation follows the B_{eff} and is finally excited or inverted.

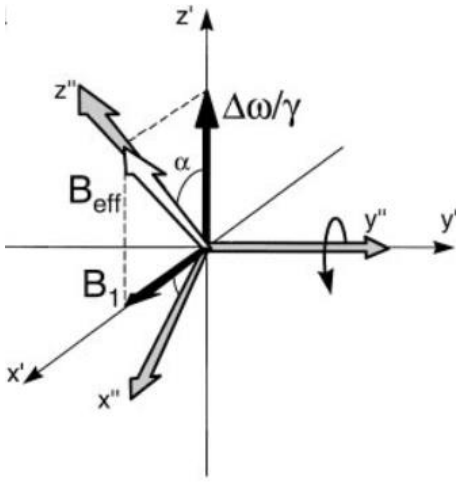

Figure 1.18. Vector diagram for the adiabatic excitation, showing the relationship between the frequency modulated frame, x',y',z' (thin axes) and the B_{eff} frame, x'',y'',z'' (thick axes). Δω/γ is the longitudinal field and B_1 is the applied RF field. Adapted from (65).

There are many different types of adiabatic pulses based on different amplitude and frequency modulation, but the one used in this study is the hyperbolic secant inversion pulse (HS). The equation for HS pulse is given by:

$$B_1(t) = A(t)\exp^{-i\int \omega_1(t')dt'} \qquad \text{eq 1.35}$$

where,

$$A(t) = A_0\,\mathrm{sech}(\beta t) \qquad \text{eq 1.36}$$

$$\omega_1(t) = -\mu\beta\tanh(\beta t) \qquad \text{eq 1.37}$$

and A_0 is the peak amplitude (μT), β is frequency modulation (rad/s), and μ is the phase modulation parameter (dimensionless).

The method that has been used in this study is called heteronuclear adiabatic relaxation dispersion (HARD). This method utilises a series of HS pulses (HS_n) to measure ^{15}N $R_{1\rho}$ and $R_{2\rho}$ rates during adiabatic rotations of the +z magnetisation. For the $R_{1\rho}$ experiment, the ^{15}N magnetization is positioned longitudinally and then subjected to a train of adiabatic pulses (HS_n). For the $R_{2\rho}$ experiment, the ^{15}N magnetization is positioned in the transverse plane and then subjected to a train of adiabatic pulses (HS_n). The dispersion in the rates is created by the type of HS pulse. Typically, it is expected that $R_{1\rho}$ should increase with the increase in the HS stretching factor (n) and $R_{2\rho}$ should decrease with an increase in the stretching factor (Figure 1.19). Unlike measuring relaxation rates under free precession, this method reduces the relaxation rates and allows for greater signal to noise. Thus, aiding to capture dynamics on the order of 10^4-10^6 s^{-1}.

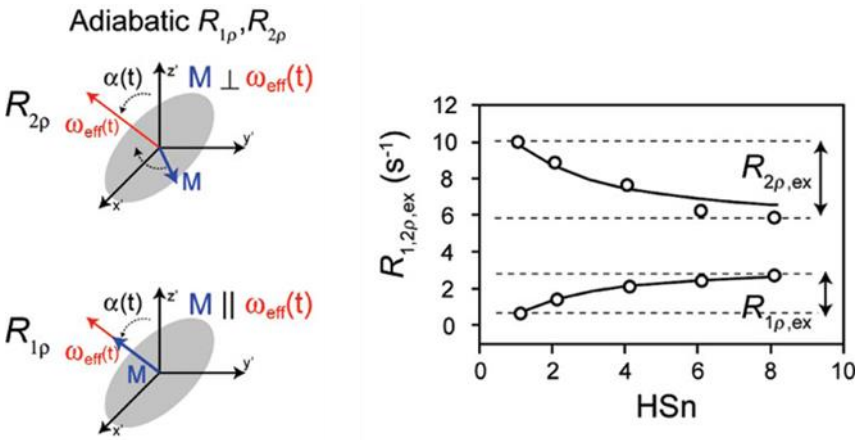

Figure 1.19. $R_{1\rho}$ (longitudinal rates) and $R_{2\rho}$ (transverse rates) dispersion curves as obtained by changing the HS pulse shape. $R_{1\rho}$ increases with the increase in the HS stretching factor (n) and $R_{2\rho}$ decreases with an increase in the stretching factor. M is the magnetisation and is modulated by effective ω_{eff} field. α being the sweep (flip) angle. Adapted from (67).

1.8.6.4 ^{15}N chemical exchange saturation transfer (CEST) for slow µs-ms dynamics

CEST methodology gives us dynamic information on a timescale closer to the CPMG relaxation dispersion (RD), applicable to 10-500 s^{-1} (4). This method allows extracting information where the populations are highly skewed ($p_A >> p_B$). The method works by applying a weak RF field B_1 at various offset positions in the NMR spectrum for a period of T_{ex} and measuring the intensities of the major state (Figure 1.20). The CEST data are plotted as a function of the offset values and I/I_0, where I_0 is the intensity of the major state with no T_{ex}. During weak B_1 field, when it is on-resonance to major state A, the M_{zA} is saturated, and the I/I_0 is close to 0. When it is on-resonance to the minor state B, the M_{zA} decreases due to stochastic transitions of spins from state A to B and then back to A, which also results in a decrease in the I/I_0. Thus, CEST profiles are characterised by two or more dips in the intensity, one at the major state offset and the rest at the minor state offset. Hence, it helps to make the invisible state, visible.

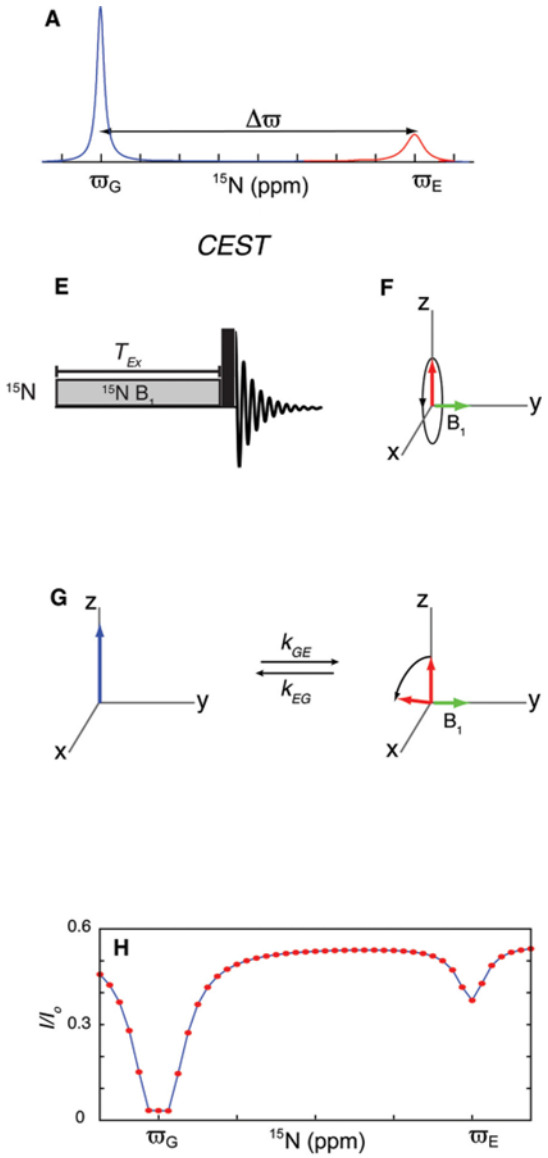

Figure 1.20. ^{15}N CEST experiment. A weak B_1 field is applied along the y axis (green) for a time T_{EX} before acquisition of the spectrum. When the B_1 field is on resonance with the minor state, precession occurs around the y axis. The ratio I/I_0 is plotted, as a function of offset where I is the intensity after an irradiation period of duration T_{EX} and I_0 is the intensity when $T_{EX} = 0$. There is a loss of intensity when the weak continuous-wave field is resonant with the major (ω_G) and minor states (ω_E). k_{GE} is the forward exchange rate between ground and excited states and k_{EG} is the backward exchange rate. Adapted from (68).

1.9 Scope of the Thesis

This thesis investigates the role of conformational heterogeneity of FUS-RRM in its aggregation behavior, with a particular focus on how changes in conformational plasticity may influence FUS-RRM's propensity to form aggregates. We aim to identify and characterize distinct conformational states using a range of NMR techniques, alongside pH and ATP-induced perturbations. By combining CEST, adiabatic $R_{1\rho}$ and $R_{2\rho}$ relaxation dispersion, and

other biophysical techniques, this study uncovers the existence of different excited states in FUS-RRM. These findings expand our understanding of the dynamic nature of FUS-RRM and its possible functional implications in cellular processes, such as binding to different nucleic acids or other cofactors. Additionally, the study unravels the importance of fast dynamics in suppressing FUS-RRM aggregation, while slower dynamics promoting it. Using such perturbations, we seek to understand the molecular mechanisms behind FUS-RRM's involvement in diseases like ALS and FTD. This research may pave the way for potential therapeutic strategies that target the conformational states, offering new avenues for intervention in neurodegenerative disorders.

1.10 References

1. <Molecular structure and function.pdf>.
2. <Alberts, Johnson, Levis, Raff - Molecular Biology Of The Cell (2002, Garland Science) - libgen.li.pdf>.
3. Schlick T. Protein Structure Hierarchy. Molecular Modeling and Simulation: An Interdisciplinary Guide: An Interdisciplinary Guide. 2010;21:105-28.
4. Jumper J, Evans R, Pritzel A, Green T, Figurnov M, Ronneberger O, et al. Highly accurate protein structure prediction with AlphaFold. Nature. 2021;596(7873):583-9.
5. Baldwin RL. The nature of protein folding pathways: the classical versus the new view. J Biomol NMR. 1995;5(2):103-9.
6. Bryngelson JD, Onuchic JN, Socci ND, Wolynes PG. Funnels, pathways, and the energy landscape of protein folding: a synthesis. Proteins. 1995;21(3):167-95.
7. Dill KA, Chan HS. From Levinthal to pathways to funnels. Nat Struct Biol. 1997;4(1):10-9.
8. Baldwin RL, Rose GD. Is protein folding hierarchic? I. Local structure and peptide folding. Trends Biochem Sci. 1999;24(1):26-33.
9. Martin AC, Orengo CA, Hutchinson EG, Jones S, Karmirantzou M, Laskowski RA, et al. Protein folds and functions. Structure (London, England : 1993). 1998;6(7):875-84.
10. Wright PE, Dyson HJ. Intrinsically disordered proteins in cellular signalling and regulation. Nature reviews Molecular cell biology. 2015;16(1):18-29.
11. Bullock AN, Fersht AR. Rescuing the function of mutant p53. Nat Rev Cancer. 2001;1(1):68-76.
12. Thomas PJ, Qu BH, Pedersen PL. Defective protein folding as a basis of human disease. Trends Biochem Sci. 1995;20(11):456-9.
13. Horwich A. Protein aggregation in disease: a role for folding intermediates forming specific multimeric interactions. J Clin Invest. 2002;110(9):1221-32.
14. Kelly JW. The alternative conformations of amyloidogenic proteins and their multi-step assembly pathways. Curr Opin Struct Biol. 1998;8(1):101-6.
15. Sunde M, Blake C. The structure of amyloid fibrils by electron microscopy and X-ray diffraction. Adv Protein Chem. 1997;50:123-59.
16. Gade Malmos K, Blancas-Mejia LM, Weber B, Buchner J, Ramirez-Alvarado M, Naiki H, et al. ThT 101: a primer on the use of thioflavin T to investigate amyloid formation. Amyloid. 2017;24(1):1-16.

17. Fandrich M, Forge V, Buder K, Kittler M, Dobson CM, Diekmann S. Myoglobin forms amyloid fibrils by association of unfolded polypeptide segments. Proc Natl Acad Sci U S A. 2003;100(26):15463-8.
18. Patni D, Jha SK. Thermodynamic modulation of folding and aggregation energy landscape by DNA binding of functional domains of TDP-43. Biochimica et biophysica acta Proteins and proteomics. 2023;1871(4):140916.
19. Glisovic T, Bachorik JL, Yong J, Dreyfuss G. RNA-binding proteins and post-transcriptional gene regulation. FEBS Lett. 2008;582(14):1977-86.
20. Mishra P, Jha SK. The native state conformational heterogeneity in the energy landscape of protein folding. Biophysical Chemistry. 2022;283:106761.
21. King OD, Gitler AD, Shorter J. The tip of the iceberg: RNA-binding proteins with prion-like domains in neurodegenerative disease. Brain Res. 2012;1462:61-80.
22. Lasagna-Reeves CA, Castillo-Carranza DL, Sengupta U, Sarmiento J, Troncoso J, Jackson GR, et al. Identification of oligomers at early stages of tau aggregation in Alzheimer's disease. FASEB J. 2012;26(5):1946-59.
23. Neumann M, Sampathu DM, Kwong LK, Truax AC, Micsenyi MC, Chou TT, et al. Ubiquitinated TDP-43 in frontotemporal lobar degeneration and amyotrophic lateral sclerosis. Science (New York, NY). 2006;314(5796):130-3.
24. Prusiner SB, Woerman AL, Mordes DA, Watts JC, Rampersaud R, Berry DB, et al. Evidence for alpha-synuclein prions causing multiple system atrophy in humans with parkinsonism. Proc Natl Acad Sci U S A. 2015;112(38):E5308-17.
25. Neumann M, Bentmann E, Dormann D, Jawaid A, DeJesus-Hernandez M, Ansorge O, et al. FET proteins TAF15 and EWS are selective markers that distinguish FTLD with FUS pathology from amyotrophic lateral sclerosis with FUS mutations. Brain. 2011;134(Pt 9):2595-609.
26. Law WJ, Cann KL, Hicks GG. TLS, EWS and TAF15: a model for transcriptional integration of gene expression. Brief Funct Genomic Proteomic. 2006;5(1):8-14.
27. Patel A, Lee HO, Jawerth L, Maharana S, Jahnel M, Hein MY, et al. A Liquid-to-Solid Phase Transition of the ALS Protein FUS Accelerated by Disease Mutation. Cell. 2015;162(5):1066-77.
28. Szewczyk B, Günther R, Japtok J, Frech MJ, Naumann M, Lee HO, et al. FUS ALS neurons activate major stress pathways and reduce translation as an early protective mechanism against neurodegeneration. Cell Reports. 2023;42(2).
29. Luo F, Gui X, Zhou H, Gu J, Li Y, Liu X, et al. Atomic structures of FUS LC domain segments reveal bases for reversible amyloid fibril formation. Nat Struct Mol Biol. 2018;25(4):341-6.
30. Murthy AC, Dignon GL, Kan Y, Zerze GH, Parekh SH, Mittal J, et al. Molecular interactions underlying liquid-liquid phase separation of the FUS low-complexity domain. Nat Struct Mol Biol. 2019;26(7):637-48.
31. Liu X, Niu C, Ren J, Zhang J, Xie X, Zhu H, et al. The RRM domain of human fused in sarcoma protein reveals a non-canonical nucleic acid binding site. Biochim Biophys Acta. 2013;1832(2):375-85.
32. Afroz T, Cienikova Z, Clery A, Allain FHT. One, Two, Three, Four! How Multiple RRMs Read the Genome Sequence. Methods Enzymol. 2015;558:235-78.
33. Agrawal S, Kuo PH, Chu LY, Golzarroshan B, Jain M, Yuan HS. RNA recognition motifs of disease-linked RNA-binding proteins contribute to amyloid formation. Scientific reports. 2019;9(1):6171.
34. Sun Z, Diaz Z, Fang X, Hart MP, Chesi A, Shorter J, et al. Molecular determinants and genetic modifiers of aggregation and toxicity for the ALS disease protein FUS/TLS. PLoS biology. 2011;9(4):e1000614.

35. Kang J, Lim L, Song J. ATP binds and inhibits the neurodegeneration-associated fibrillization of the FUS RRM domain. Communications biology. 2019;2:223.
36. Balch WE, Morimoto RI, Dillin A, Kelly JW. Adapting proteostasis for disease intervention. Science (New York, NY). 2008;319(5865):916-9.
37. Hartl FU, Bracher A, Hayer-Hartl M. Molecular chaperones in protein folding and proteostasis. Nature. 2011;475(7356):324-32.
38. Perlaza K, Toutkoushian H, Boone M, Lam M, Iwai M, Jonikas MC, et al. The Mars1 kinase confers photoprotection through signaling in the chloroplast unfolded protein response. eLife. 2019;8.
39. Austin RH, Beeson KW, Eisenstein L, Frauenfelder H, Gunsalus IC. Dynamics of ligand binding to myoglobin. Biochemistry. 1975;14(24):5355-73.
40. Evenäs J, Forsén S, Malmendal A, Akke M. Backbone dynamics and energetics of a calmodulin domain mutant exchanging between closed and open conformations. Journal of molecular biology. 1999;289(3):603-17.
41. Henzler-Wildman K, Kern D. Dynamic personalities of proteins. Nature. 2007;450(7172):964-72.
42. Johnson CK. Calmodulin, conformational states, and calcium signaling. A single-molecule perspective. Biochemistry. 2006;45(48):14233-46.
43. Lisi GP, Loria JP. Using NMR spectroscopy to elucidate the role of molecular motions in enzyme function. Progress in nuclear magnetic resonance spectroscopy. 2016;92-93:1-17.
44. Kleckner IR, Foster MP. An introduction to NMR-based approaches for measuring protein dynamics. Biochim Biophys Acta. 2011;1814(8):942-68.
45. Greenfield NJ. Using circular dichroism spectra to estimate protein secondary structure. Nature protocols. 2006;1(6):2876-90.
46. Monsellier E, Bedouelle H. Quantitative measurement of protein stability from unfolding equilibria monitored with the fluorescence maximum wavelength. Protein engineering, design & selection : PEDS. 2005;18(9):445-56.
47. Sindrewicz P, Li X, Yates EA, Turnbull JE, Lian LY, Yu LG. Intrinsic tryptophan fluorescence spectroscopy reliably determines galectin-ligand interactions. Scientific reports. 2019;9(1):11851.
48. James NG, Jameson DM. Steady-state fluorescence polarization/anisotropy for the study of protein interactions. Methods in molecular biology (Clifton, NJ). 2014;1076:29-42.
49. Semisotnov GV, Rodionova NA, Razgulyaev OI, Uversky VN, Gripas AF, Gilmanshin RI. Study of the "molten globule" intermediate state in protein folding by a hydrophobic fluorescent probe. Biopolymers. 1991;31(1):119-28.
50. Wen J, Arakawa T, Philo JS. Size-exclusion chromatography with on-line light-scattering, absorbance, and refractive index detectors for studying proteins and their interactions. Analytical biochemistry. 1996;240(2):155-66.
51. Li H, Cocco MJ, Steitz TA, Engelman DM. Conversion of phospholamban into a soluble pentameric helical bundle. Biochemistry. 2001;40(22):6636-45.
52. Temiryazev AG, Krayev AV, Temiryazeva MP. Two dynamic modes to streamline challenging atomic force microscopy measurements. Beilstein journal of nanotechnology. 2021;12:1226-36.
53. Pica A, Leone S, Di Girolamo R, Donnarumma F, Emendato A, Rega MF, et al. pH driven fibrillar aggregation of the super-sweet protein Y65R-MNEI: A step-by-step structural analysis. Biochimica et biophysica acta General subjects. 2018;1862(4):808-15.
54. de sa Peixoto P, Roiland C, Thomas D, Briard-Bion V, Le Guellec R, Parayre S, et al. Recrystallized S-layer protein of a probiotic Propionibacterium: structural and nanomechanical changes upon temperature or pH shifts probed by solid-state NMR and AFM. Langmuir : the ACS journal of surfaces and colloids. 2015;31(1):199-208.

55. Ferreira CF, Benelli EM, Klein JJ, Schreiner W, Camargo PC. Effect of protein solution components in the adsorption of Herbaspirillum seropedicae GlnB protein on mica. Colloids and surfaces B, Biointerfaces. 2009;73(2):289-93.
56. Sung JJ, Pardeshi NN, Mulder AM, Mulligan SK, Quispe J, On K, et al. Transmission electron microscopy as an orthogonal method to characterize protein aggregates. J Pharm Sci. 2015;104(2):750-9.
57. Malatesta M. Transmission Electron Microscopy as a Powerful Tool to Investigate the Interaction of Nanoparticles with Subcellular Structures. International journal of molecular sciences. 2021;22(23).
58. Winey M, Meehl JB, O'Toole ET, Giddings TH, Jr. Conventional transmission electron microscopy. Molecular biology of the cell. 2014;25(3):319-23.
59. Correia I, Sung J, Burton R, Jakob CG, Carragher B, Ghayur T, et al. The structure of dual-variable-domain immunoglobulin molecules alone and bound to antigen. mAbs. 2013;5(3):364-72.
60. Mulder AM, Carragher B, Towne V, Meng Y, Wang Y, Dieter L, et al. Toolbox for non-intrusive structural and functional analysis of recombinant VLP based vaccines: a case study with hepatitis B vaccine. PloS one. 2012;7(4):e33235.
61. Bothe JR, Nikolova EN, Eichhorn CD, Chugh J, Hansen AL, Al-Hashimi HM. Characterizing RNA dynamics at atomic resolution using solution-state NMR spectroscopy. Nat Methods. 2011;8(11):919-31.
62. Marion D. An introduction to biological NMR spectroscopy. Mol Cell Proteomics. 2013;12(11):3006-25.
63. <chapter_8_relaxations_Keeler.pdf>.
64. Ridgway JP. Cardiovascular magnetic resonance physics for clinicians: part I. Journal of cardiovascular magnetic resonance : official journal of the Society for Cardiovascular Magnetic Resonance. 2010;12(1):71.
65. Tannus A, Garwood M. Adiabatic pulses. NMR Biomed. 1997;10(8):423-34.
66. Traaseth NJ, Chao FA, Masterson LR, Mangia S, Garwood M, Michaeli S, et al. Heteronuclear Adiabatic Relaxation Dispersion (HARD) for quantitative analysis of conformational dynamics in proteins. J Magn Reson. 2012;219:75-82.
67. Mangia S, Traaseth NJ, Veglia G, Garwood M, Michaeli S. Probing slow protein dynamics by adiabatic R(1rho) and R(2rho) NMR experiments. J Am Chem Soc. 2010;132(29):9979-81.
68. Vallurupalli P, Bouvignies G, Kay LE. Studying "invisible" excited protein states in slow exchange with a major state conformation. J Am Chem Soc. 2012;134(19):8148-61.
69. Kay LE, Torchia DA, Bax A. Backbone dynamics of proteins as studied by 15N inverse detected heteronuclear NMR spectroscopy: application to staphylococcal nuclease. Biochemistry. 1989;28(23):8972-9.

Chapter 2: Investigating conformational heterogeneity and fibril formation in FUS-RRM

2.1 Introduction

A recent study by Lu et al. (1) shows compelling evidence regarding the structural characteristics of the FUS-RRM domain. The use of CD and NMR spectroscopy demonstrates that the FUS-RRM maintains a well-folded structure at the pH 5 and 6.8, distinguishing it from the disordered regions at the N- and C-termini of this protein. The observation of irreversible thermal denaturation and renaturation suggests a stable, yet potentially delicate, folding landscape for the FUS-RRM. The NMR spin relaxation measurements—specifically T_1, T_2, and het-nOe indicate that while FUS-RRM exhibits ps-ns dynamics, it does not engage in microsecond to millisecond dynamics. This implies that the folding dynamics are relatively fast, but the domain does not undergo significant conformational changes over longer timescales (1). The low het-nOe value (0.7) combined with the average order parameter (S^2 = 0.77) indicates that the FUS-RRM is not in a tightly compacted conformation (1), a condition which may facilitate interactions with other molecules, including RNA or other proteins. This less compact structure could be a factor in its potential involvement in aggregation. However, its link to aggregation is not straightforward.

Many biological processes, such as protein folding and conformational changes, occur on the slow μs-to-ms time scale and are of general interest for understanding protein function. Advanced experimental techniques like time-resolved Förster resonance energy transfer (FRET), single-molecule force spectroscopy, and molecular dynamics (MD) simulations have provided insights into the motions of different proteins (2, 3). Amongst these, NMR spectroscopy has been widely used to investigate the structure and dynamics of biomolecules. Indeed, the link between dynamics and function of a protein has been strengthened by the recent advances that have allowed for the detection of sparsely and transiently populated biomolecular conformations. In this direction, the advanced NMR experiments such as chemical exchange saturation transfer (CEST) (4, 5), dark exchange saturation transfer (DEST) (6, 7), Carr-Purcell-Meiboom-Gill (CPMG) (8, 9), off-resonance rotating frame ($R_{1\rho}$) (10, 11), and paramagnetic relaxation enhancement (PRE) (12) have been particularly useful for the detection of low-populated, transient states of proteins with lifetimes ranging from 10^{-4} to 10^{-1} s. By enabling the study of these states, these techniques enhance our understanding of a correlation between protein function and conformational dynamics, thereby delineating the molecular mechanisms behind various diseases related to protein misfolding and aggregation. Therefore, insights into the conformational dynamics of a protein are required to obtain better insights into the process by which it undergoes aggregation. In this chapter, we have

investigated fast and slow μs-ms dynamics of FUS-RRM using two different NMR tools as explained below.

2.2 Methods

2.2.1 Protein overexpression and purification

The cDNA fragment encoding the FUS-RRM (aa 282-376) domain, cloned in the pET 28a vector, was obtained as a kind gift from Prof. Neel Sarovar Bhavesh, International Centre for Genetic Engineering and Biotechnology (ICGEB), New Delhi, India. The recombinant construct carried a thrombin cleavable $(His)_6$ tag at the N-termini. Recombinant protein overexpression was carried out in *Escherichia coli* (BL21). Initial optimisation was performed with different IPTG concentrations and temperature. Good induction was observed with 0.5 mM IPTG at 28°C. Subsequently, the cells were induced at an OD_{600} of 0.8-1.2 using 0.5 mM isopropyl β-D-1-thiogalactopyranose (IPTG) at 28°C with 180 rpm for 8 hrs. The harvested culture was lysed in Tris buffer (20 mM Tris-Cl, 150 mM NaCl, pH 8) containing lysozyme and EDTA-free protease inhibitors. Sonication of the cells was carried out at 60% amplitude with 5 sec ON and 5 sec OFF pulse for 3 minutes in an ice bath, with the cycle repeated 3 times to ensure lysis. The cell lysate, thus obtained, was centrifuged at 14000 x g for 1 h at 4°C to obtain the total soluble protein (TSP). The TSP was circulated through a pre-equilibrated Ni-NTA affinity column (GE Healthcare) for 1 h and was finally eluted using 300 mM imidazole at 4°C. The eluted protein was further purified using a size-exclusion chromatography column, Hi-Prep Sephacryl S-100 16/60 (GE Healthcare). For NMR studies, ^{13}C and/or ^{15}N labeled FUS-RRM samples were purified by growing bacteria in M9 media using ^{13}C-glucose and $^{15}NH_4Cl$ as the sole source of carbon and nitrogen, respectively. The protein was concentrated in 10 mM sodium phosphate buffer, pH 6.4, and 100 mM NaCl.

2.2.2 NMR Spectroscopy

All the NMR experiments were recorded at 298 K on an Ascend^{TM} Bruker AVANCE III HD 14.1 Tesla (600 MHz) NMR spectrometer equipped with a quad-channel ($^1H/^{13}C/^{15}N/^{19}F$) Cryoprobe (in-house). NMR spectra were collected with 2048 x 128 total points in F_2 (^1H) and F_1 (^{15}N) dimensions. Spectral widths of 12 ppm (^1H) and 32 ppm (^{15}N) were used, for which an acquisition time of 141 ms was obtained in the direct dimension (F_2). All the NMR spectra were processed in NMRPipe (13) and analyzed using POKY (14). The resonances were

directly transferred from the already available assignments by Liu *et al*. and confirmed using triple resonance experiments like TOCSY, HNCA, and CBCANH (15).

2.2.2.1 ^{15}N HARD

Heteronuclear Adiabatic Relaxation Dispersion (HARD) experiments were recorded for different samples on the 600 MHz NMR spectrometer. Each HS pulse was 4-msec and applied in groups of four to spin-lock the ^{15}N magnetisation. Relaxation delays for adiabatic $R_{1\rho}$ and $R_{2\rho}$ experiments were then varied by changing the number of composite pulses such as 0, 1, 2, 4, and 8. The relaxation delays used for $R_{1\rho}$ were 0, 16, 32, 64, and 128 ms. For $R_{2\rho}$ experiments, the relaxation delays used were 0, 16, 32, and 64 ms. The R_1 experiments were acquired similarly to $R_{1\rho}$ and $R_{2\rho}$ experiments but without using the adiabatic pulse during evolution. The delays used for the R_1 experiment were 0, 48, 96, 192, 320, 480, and 640 ms.

The $R_1/R_{1\rho}/R_{2\rho}$ rates were calculated by fitting the peak intensities plotted against the corresponding set of relaxation delays to a mono-exponential decay model in a Mathematica script (16). The errors were obtained using 500 Monte-Carlo simulations. $R_{1\rho}$ and $R_{2\rho}$ relaxation rates are dependent upon the time evolution of the effective frequency and tilt angle α,

$$R_{1\rho,ex}(t) = \int_0^{T_p} p_A p_B \Delta\omega^2 \sin^2 \alpha(t) \frac{\tau_{ex}}{1+(\omega_{eff}(t)\tau_{ex})^2} dt \qquad \text{eq 2.1}$$

$$R_{2p,ex}(t) = \int_0^{T_p} p_A p_B \Delta\omega^2 \left[\cos^2 \alpha(t)\tau_{ex} + \frac{1}{2}\sin^2 \alpha(t) \frac{\tau_{ex}}{1+(\omega_{eff}(t)\tau_{ex})^2}\right] dt \qquad \text{eq 2.2}$$

where, p_A and p_B are the populations of the two exchanging sites, Δω is the chemical shift difference, and τ_{ex} is the exchange-correlation time. The R_1, $R_{1\rho}$, and $R_{2\rho}$ relaxation rates obtained from the HARD experiments were used to obtain subsequent k_{ex} and p_A by fitting the R_1, $R_{1\rho}$, and $R_{2\rho}$ data to time-dependent Bloch-McConnell equations under a two-site exchange model using numerical fittings, due to the lack of an analytical solution.

2.2.2.2 ^{15}N CEST experiment

The ^{15}N CEST data was acquired using a B_1 field of 30 Hz with an exchange time (T_{ex}) of 400 ms. A total of 64 planes were recorded between -912 and 972.8 Hz with a spacing of 30 Hz. The B_1 field was calibrated using the method described by Guenneugues *et al.* (17) and used

in the analyses. The data was also recorded at a B_1 field of 10 Hz and 60 Hz, but were not used in the fit.

Global lineshape fitting was used to extract peak intensities from different planes of the CEST, using the FuDA package (https://www.ucl.ac.uk/hansen-lab/fuda/). The output data was then fit to the two-state exchange models using ChemEx (https://github.com/gbouvignies/ChemEx) to extract pb and k_{ex} values by constraining R_{2A}=R_{2B}. For CEST analysis, ratio of intensities I/I_0 was plotted as a function of ^{15}N-offset position, where I is the intensity of peaks in the presence of a weak B_1 field and I_0 is the intensity of the reference peak with T_{ex} of 0.

For urea denaturation ^{15}N labeled FUS-RRM was equilibrated with 1M urea, and the CEST data was recorded and analysed, as before.

2.2.3 Random coil chemical shift prediction using POTENCI

Chemical shifts are important indicators of structural and dynamics changes (18). Deviations from the random coil chemical shifts are often used to gain insights into order-disorder of protein segments. However, one of the obstacles in chemical shift prediction has been the complicated conformational dependencies of the chemical shifts. POTENCI (19) is one of the tools designed to predict chemical shifts of IDPs using a large, validated database of disordered chemical shifts. It takes into account the effects of temperature and pH on chemical shifts and incorporates corrections for the neighbour effects, resulting in improved accuracy (https://st-protein02.chem.au.dk/potenci/).

The prediction of an unfolded state was carried out at 298 K, 0.1 M ionic strength at pH 6.4.

2.2.4 Circular dichroism (CD) spectroscopy

Far-UV CD spectroscopy was recorded on a Jasco-815 spectrometer equipped with a thermal controller for 20 μM protein, incubated overnight in different urea concentrations (0 M to 8 M at an interval of 0.5 M). The scans were acquired from 210-260 nm in a 1 mm path length quartz cuvette with a bandwidth of 1 nm and a scanning speed of 50 nm/min. Data have been represented as Mean ± SD of two independent experiments after blank subtraction. The fraction

of unfolded protein was calculated using CD ellipticity at 222 nm (equation 2.3), and was used to fit to a two-state model using (equation 2.4),

$$f_U(x) = \frac{\theta_{222}^{\text{obs}}(x) - \theta_{222}^{N}(x)}{\theta_{222}^{U}(x) - \theta_{222}^{N}(x)} \quad \text{eq 2.3}$$

where, $\theta_{222}^{N}(x) = a_N + b_N x$, $\theta_{222}^{U}(x) = a_U + b_U x$,

where, x is denaturant concentration (M), a and b are baseline intercepts and slopes, respectively.

$$exp((-dG + (m * x))/(0.001987 * 298.15))/(1 + exp((-dG + (m * x))/(0.001987 * 298.15))) \quad \text{eq 2.4}$$

where, *dG* is the free energy of unfolding, and *m* is the slope.

2.2.5 Aggregation kinetics

The pH-dependent aggregation kinetics were assessed for 200 µL reactions with different protein concentrations using 30 µM of thioflavin T (ThT) in aggregation buffer (10 mM sodium phosphate and/or sodium acetate, 100 mM NaCl, pH 6.4) at 25°C, with agitation at 60 rpm in a 96-well plate (Fluoroskan, Thermo Scientific). The fibril formation was monitored by continuously measuring the ThT intensity at 475 nm upon excitation at 440 nm. The ThT fluorescence data for the FUS-RRM without agitation was measured for the control experiments. The fit parameters were estimated using the least-squares method in OriginPro 8.5,

$$y = \frac{A_1 - A_2}{1 + (x/x_0)^p} + A_2 \quad \text{eq 2.5}$$

where, A_1 is the minimum and A_2 is the maximum ThT intensity value, x_0 is 50% of the maximum ThT intensity value, and p is the power. The lag time is obtained as the derived parameter EC10 – time taken to reach the 10% of the maximum intensity attained. All the kinetics data has been reported as an average of three biological repeats (each repeat is measured from a new overexpressed and purified protein batch) and two technical repeats (each repeat is measured using the same overexpressed and purified protein).

2.2.6 AFM imaging

After the kinetics data were recorded, the samples were centrifuged, and the fibrils, thus formed, were resuspended in 50 µL Milli-Q water. 50 µL of the sample was deposited onto a freshly cleaved mica sheet at room temperature for 5 minutes, then washed multiple times with Milli-Q water and air-dried. The AFM images were acquired in the tapping mode (Agilent technologies). The control experiments were carried out by recording AFM images on the samples before agitation. The AFM data was analyzed using WSxM 5.0 software (20).

2.2.7 SEC-MALS (Size-Exclusion Chromatography with Multi-Angle Light Scattering)

SEC-MALS analysis of the purified FUS-RRM was performed on a Superdex 200 10/300 GL column (GE Healthcare) connected to an Agilent HPLC system. This system is further connected to the Wyatt Dawn HELEOS II Light scattering device with the 18-angle light scattering detector and a refractive index detector (Wyatt Optilab T-rEX). The system was calibrated with BSA at a 2 mg/mL concentration. Breifly, 100 µL of the protein sample (1mg/ml) was injected, and the molecular weight was calculated using ASTRA 2.0 software (Wyatt Technologies).

2.3 Results

2.3.1 Protein overexpression and purification

Upon induction with IPTG, the overexpression of FUS-RRM was observed using SDS-PAGE (Figure 2.1). Significant amount of protein eluted out from the Ni-NTA column and the recombinant FUS-RRM was purified as a native protein under non-denaturing conditions after gel filtration chromatography (GFC) was performed. The protein eluted at its relative volume fraction in size exclusion chromatography. Upon concentrating the protein till 0.5 mL using a 3 kDa filter, the purity of the protein was checked using SDS PAGE (Figure 2.1).

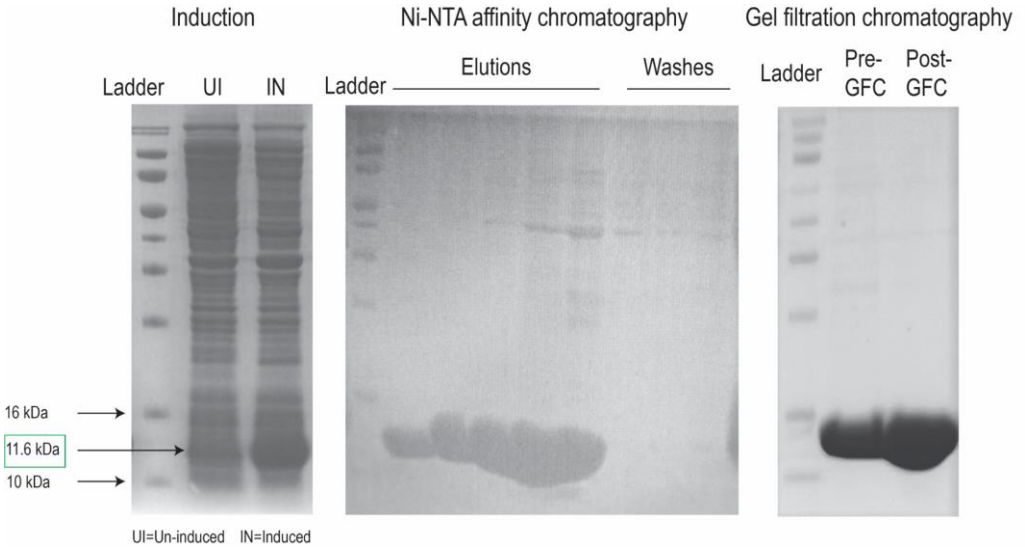

Figure 2.1. SDS-PAGE profile of FUS-RRM domain during the different steps of protein purification. A prominent band between 10 and 16 kDa was obtained upon induction with IPTG. The presence of single thick band after post-GFC confirms that the protein is purified to utmost purity.

2.3.2 Protein size confirmation

The purified protein was further characterised by SEC-MALS and was found to be monomeric in nature (Figure 2.2). The obtained molecular weight corresponded well to the expected size of the protein (11.6 kDa).

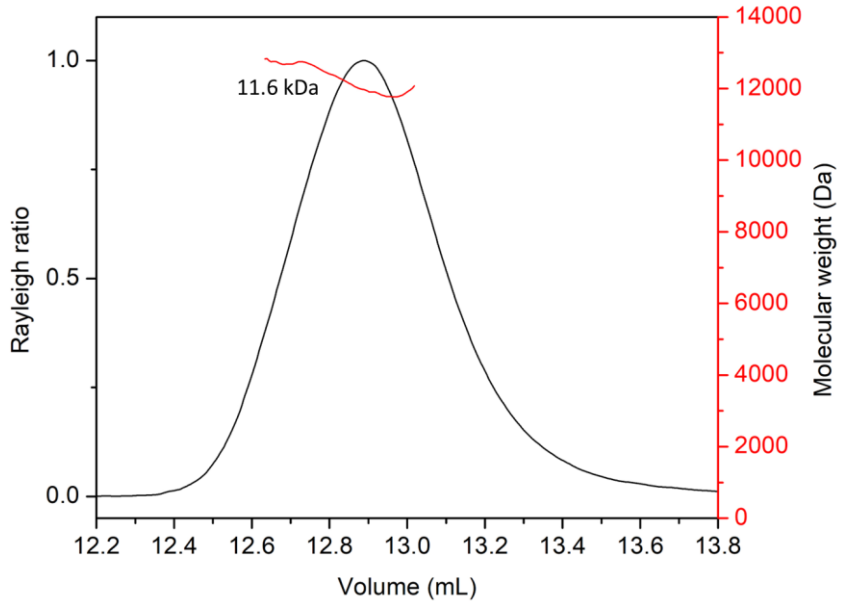

Figure 2.2. The overexpressed and purified FUS-RRM domain is monomeric in nature, as confirmed by SEC-MALS and elutes at its expected molecular weight (11.6 kDa).

For the ^{15}N labelled sample, the 2D ^{15}N-^{1}H HSQC spectrum showed characteristics of a well-folded protein, and the HSQC corresponded well to the published spectrum (1) (Figure 2.3). Overall, these results suggest that FUS-RRM at pH 6.4 is monomeric, highly stable, and adopts its native conformation.

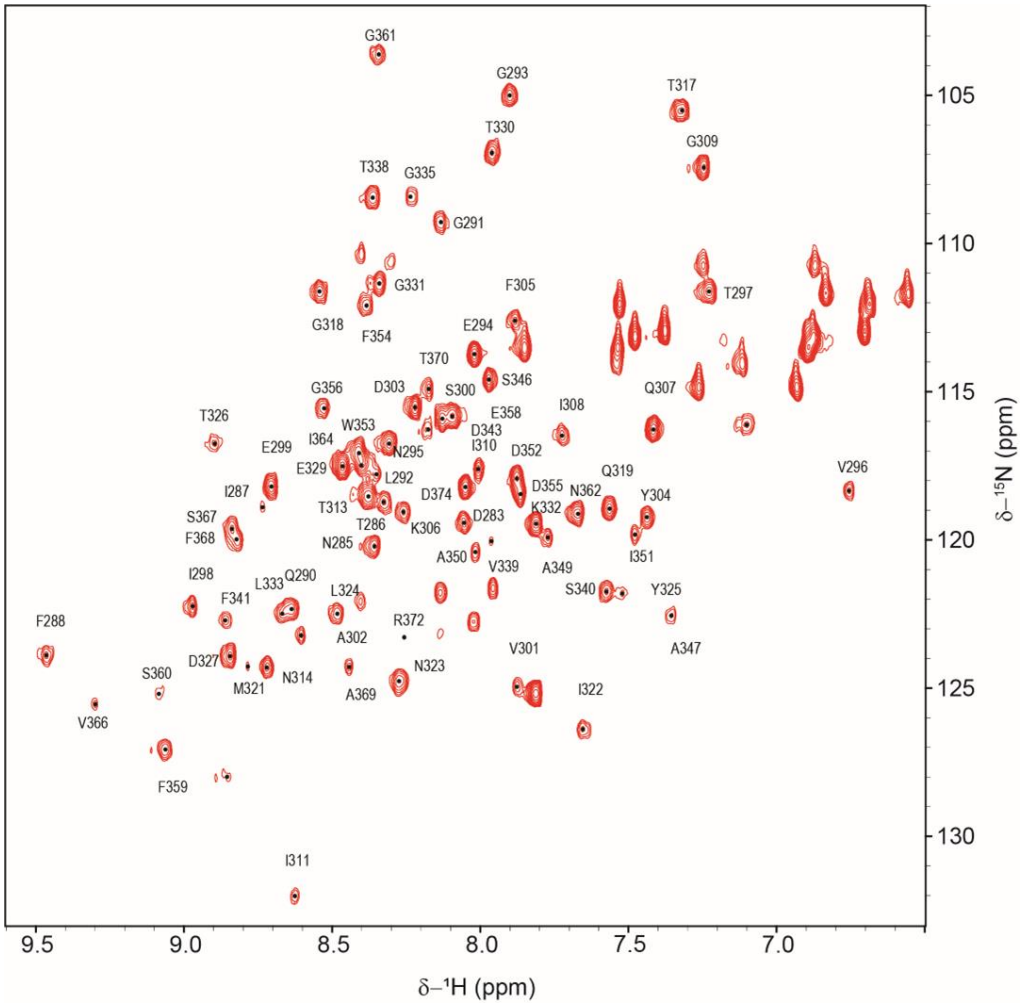

Figure 2.3. The well-dispersed peaks in 2D ^{15}N-^{1}H HSQC shows that FUS-RRM is well folded at pH 6.4, with resonance assignments marked.

2.3.3 FUS-RRM aggregation kinetics

To test for the aggregation of the FUS-RRM domain, ThT assay was used. The assessment of aggregation kinetics was performed in a concentration-dependent manner upon agitation in a 96-well plate reader (see methods). A concentration-dependent aggregation was observed in the FUS-RRM domain; with increase in concentration, a significant reduction in the lag time was observed (Figure 2.4A). Upon characterisation of the aggregate at the end of the reaction

using AFM, fibril formation was observed (Figure 2.4B). Considering only the isolated fibril, we observe a length of about 0.6 µM and a height of about 12 nm.

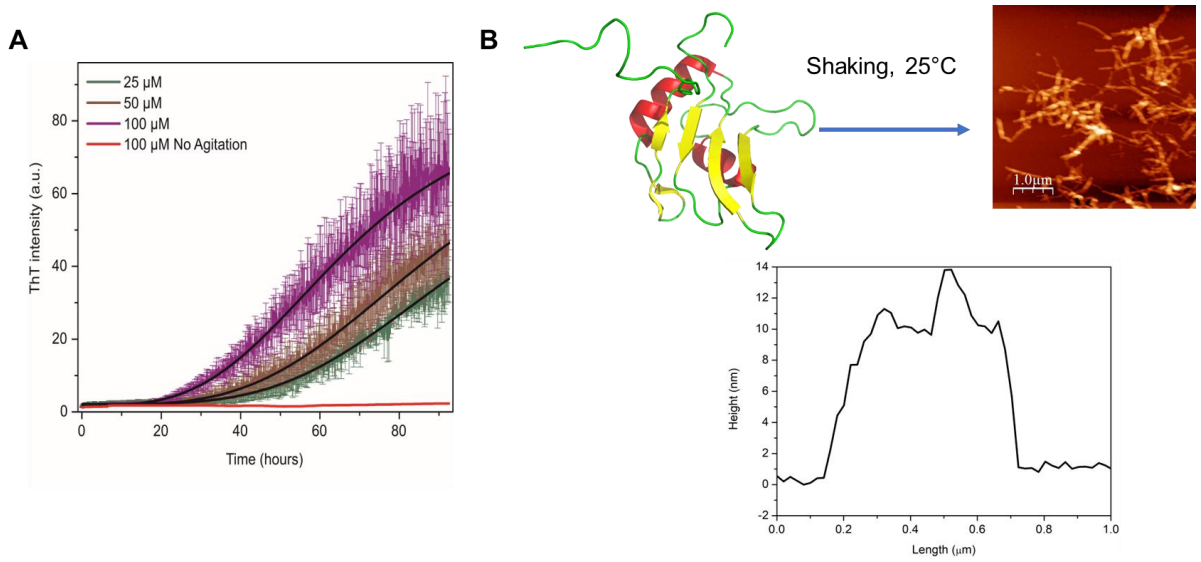

Figure 2.4. Recombinant FUS-RRM aggregates at pH 6.4. (A) The concentration-dependent aggregation of FUS-RRM upon agitation (60 rpm) at 25°C. The solid lines represent the fit to the equation 2.5. Data has been represented as Mean ± SD of three independent biological repeats. It was clearly observed that ThT intensity of FUS-RRM domain does not increase without agitation (red). (B) AFM image recorded at the end of the experiment and analysis of the length (x-axis; µM) and height (y-axis; nm) of an isolated fibril.

Despite agitation for up to 90 hours, no saturation was observed. In order to get saturation, we recorded with higher protein concentration and extended measurements up to 160 hours but still no plateau was achieved (Figure 2.5).

.

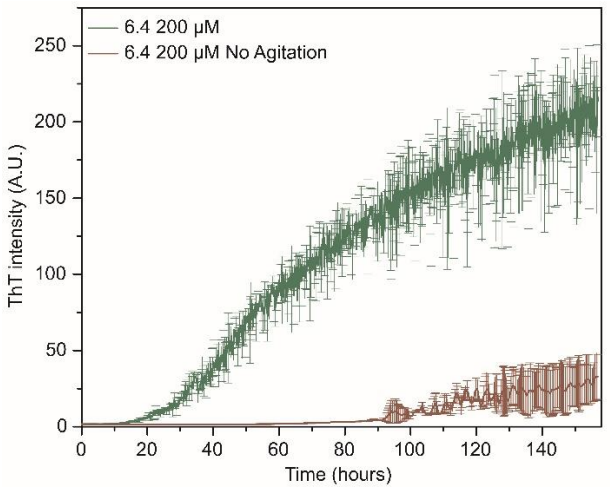

Figure 2.5. Aggregation kinetics at pH 6.4 monitored by ThT intensity while agitating the protein (200 µM) at 60 rpm. Data are represented as Mean ± SD of two biological and two technical repeats.

2.3.4 Adiabatic $R_{1\rho}$ and $R_{2\rho}$ for characterisation of fast µs-ms dynamics

To understand about role of slow dynamics in FUS-RRM aggregation, we first used adiabatic $R_{1\rho}$ and $R_{2\rho}$ relaxation dispersion experiment to detect fast µs-ms timescale of motion. R_1, $R_{1\rho}$ (Figure 2.6A), and $R_{2\rho}$ (Figure 2.6B) relaxation rates were recorded and fit to a simple two-state exchange model, using equations 2.1 and 2.2 to extract k_{ex}, pb, and $\Delta\omega$. The k_{ex} rates vary from 0.1-130 x 10^3 s^{-1}, and most residues are found to exhibit fast exchange dynamics at this timescale. The measured k_{ex} rates have been further mapped onto the structure of the FUS-RRM in (Figure 2.6C). The monomer represents about 68-99% of the population in a residue-wise plot with an average value of 93.7% (Figure 2.6D). These experiments provide evidence that the FUS-RRM exchanges to an excited state ($_{ES}^{HARD}$) in this timescale of motion (Figure 2.6E).

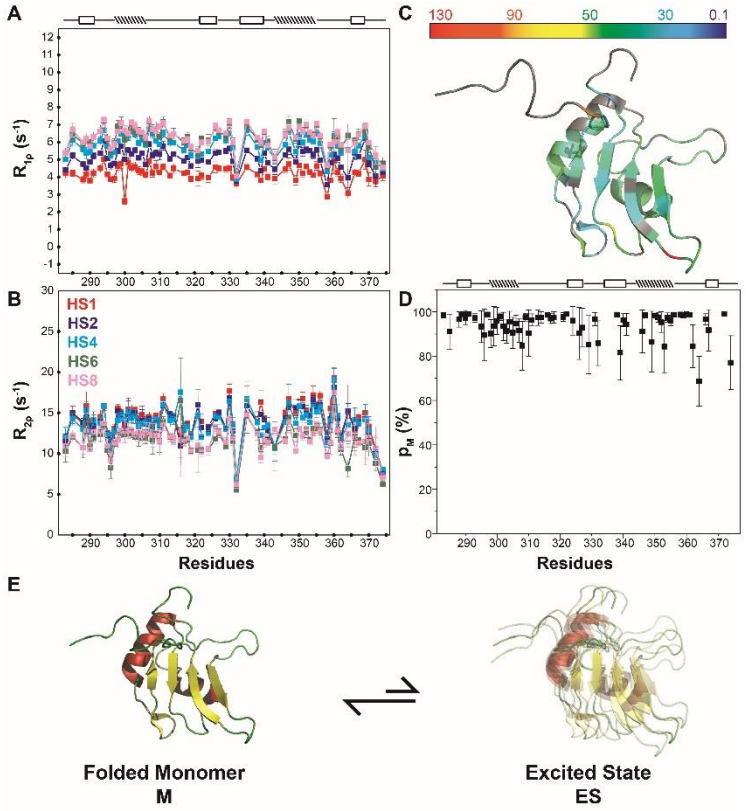

Figure 2.6. The µs-ms dynamics of the recombinant FUS-RRM domain measured at pH 6.4. (A) The measured $R_{1\rho}$ and $R_{2\rho}$ relaxation rates for FUS-RRM at 25 °C. The trends in the relaxation rates for $R_{1\rho}$ are HS1 (red) < HS2 (blue) < HS4 (sky blue) < HS6 (green) < HS8 (pink) and, (B) for $R_{2\rho}$ trends are HS1 > HS2 > HS4 > HS6 > HS8. (C) The k_{ex} rates were mapped to the FUS-RRM tertiary structure. The residues highlighted in grey do not fit any model and, hence, are not included in the discussion. (D) The population of the monomer. The secondary structure of FUS-RRM is indicated on the top of A and D, with boxed and dashed rectangles denoting strands and helices, respectively. (E) A schematic of an exchange between the monomer, M, and an excited state, ES.

2.3.5 Characterisation of slow µs-ms dynamics using ^{15}N CEST

In order to capture motions slower than adiabatic $R_{1\rho}$ and $R_{2\rho}$, the ^{15}N-CEST data was acquired at B_1 field of 30 Hz. Increasing or decreasing the B_1 field leads to broadening of the minor dips, thereby allowing us to only get information from the 30 Hz B_1 field (Figure 2.7).

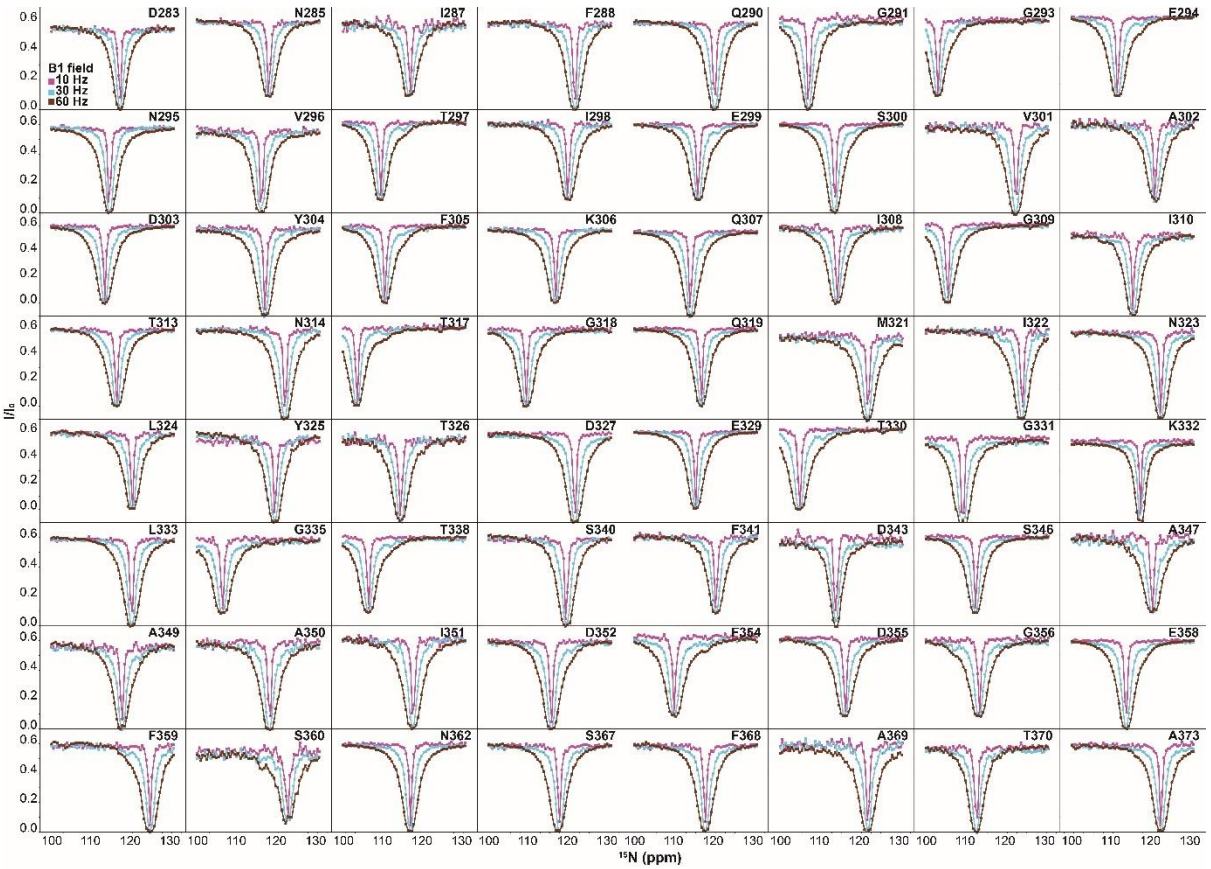

Figure 2.7. ^{15}N CEST profiles of FUS-RRM at different B_1 fields (10Hz, 30Hz, and 60Hz).

The presence of a distinct excited state can be discerned from the minor dip in the ^{15}N-CEST profiles of a number of residues at 30Hz. A total of 16 residues were globally modelled to a two-state exchange process using the Bloch-McConnell equations (Figure 2.8).

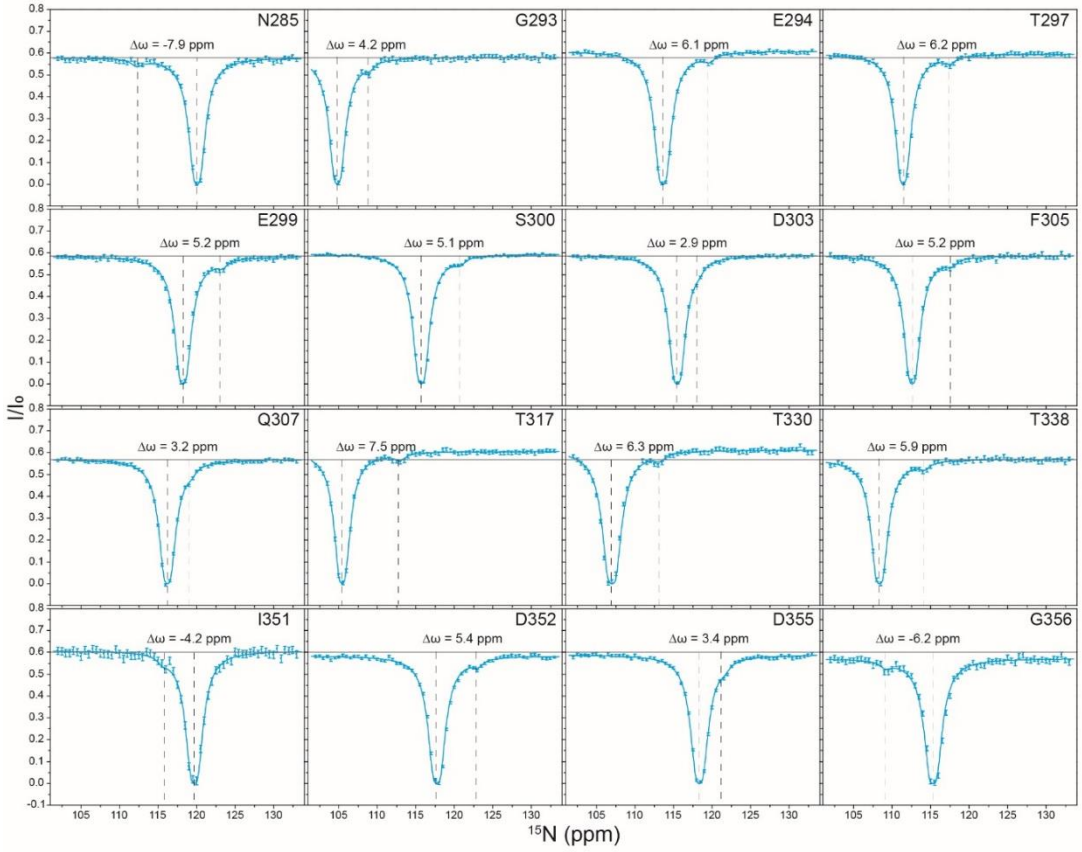

Figure 2.8. ^{15}N CEST profiles of FUS-RRM indicates the presence of a conformationally excited state. Solid lines represent the global fit to CEST data, while dashed lines represent the chemical shift of the ground and excited states. The obtained χ^2_{red} is of 2.3 using a fit to a two-state model.

The fits of the CEST data reveal that the population of the excited state (p_{ES}) is 0.14 ± 0.007 % exchanging with a rate (k_{ex}) of 257 ± 36 s^{-1}. The excited state conformation was thus calculated to be 3.9 kcal/mol higher in free energy than the ground state (Figure 2.9).

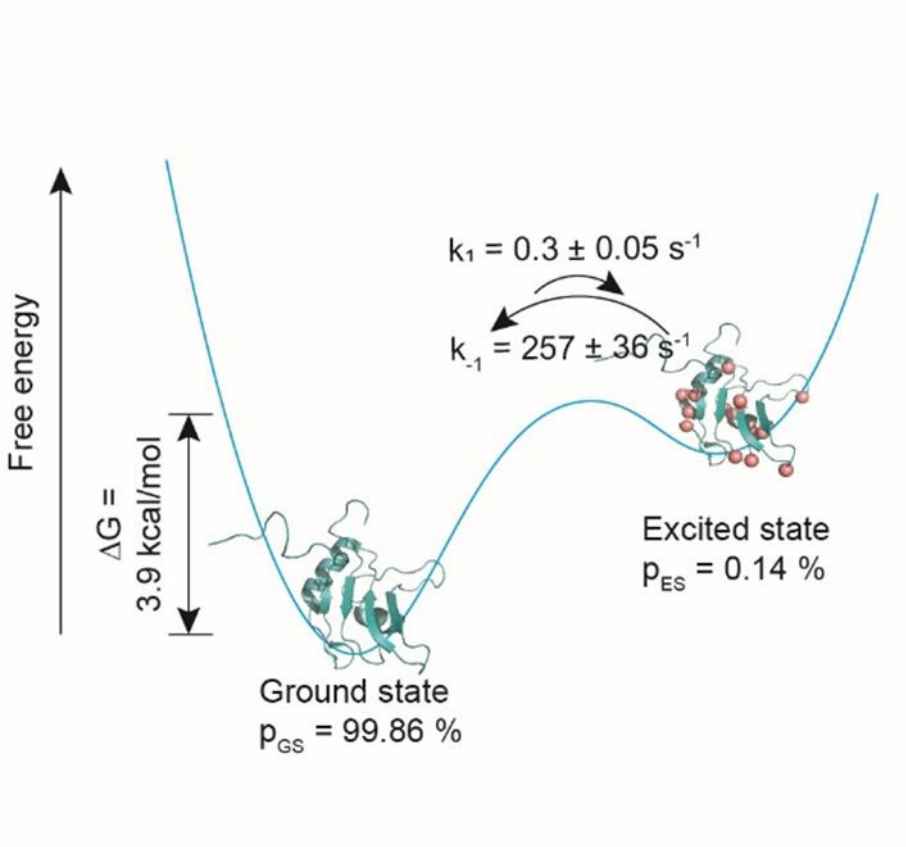

Figure 2.9. A cartoon representation of the energy landscape of FUS-RRM showing the two states (ground and excited state) and their interconversion rates with the fractional populations.

2.3.6 The ES^{CEST} of FUS-RRM is an unfolded state

To further investigate the nature of ES^{CEST}, we acquired the ^{15}N-CEST data in the presence of 1 M urea (Figure 2.10), a chaotropic agent known to induce unfolding in folded proteins (21). The analysis showed that the addition of urea further stabilized the ES^{CEST} population, as evidenced by the global fit parameters (k_{ex} = 208 ± 18.6 s^{-1}, p_{ES} = 0.53 ± 0.01) from a two-state model fit of the data (Figure 2.11A). A similar approach has been used recently by Deshmukh and co-workers to demonstrate that the dsRBD excited state is an unfolded state (22).

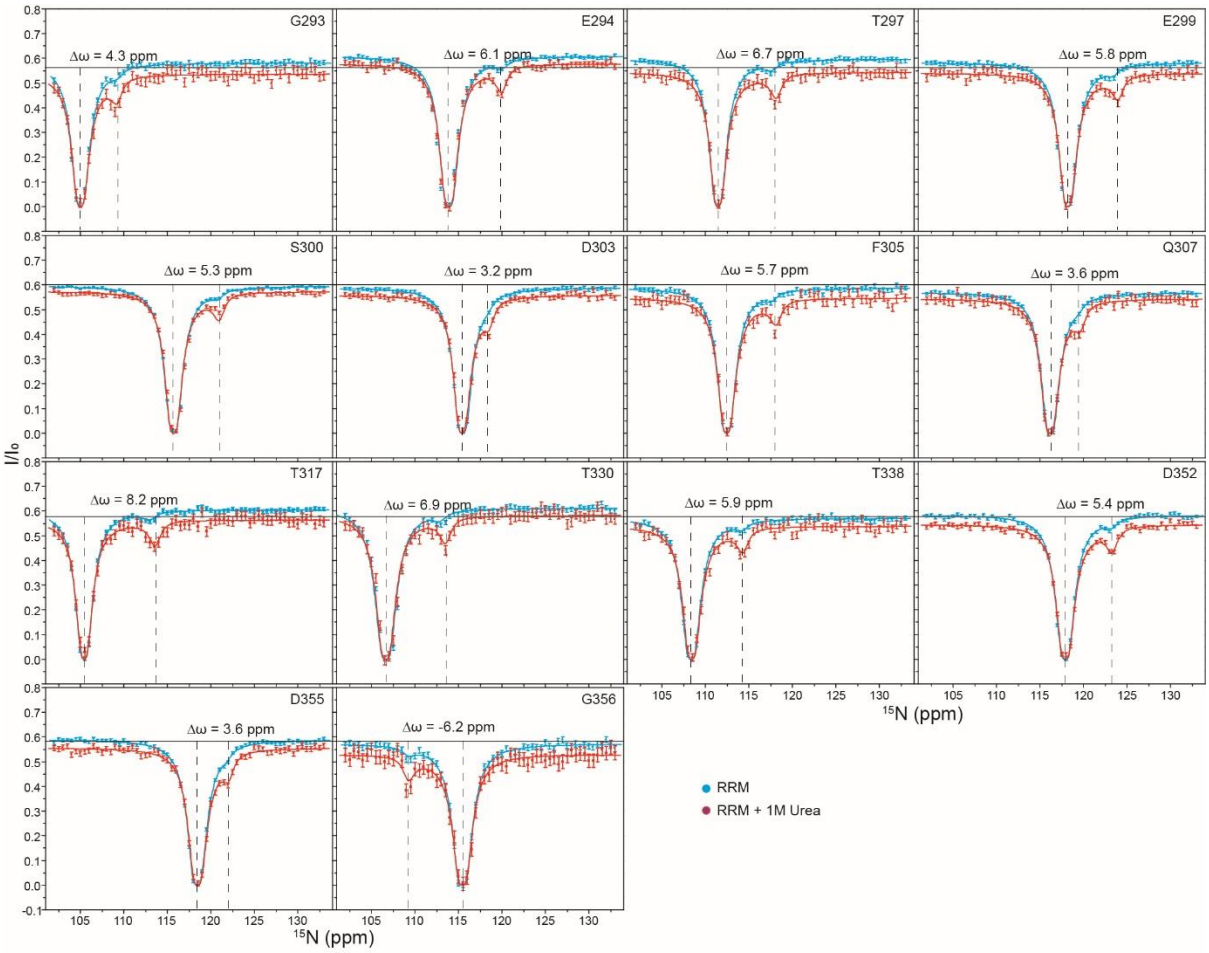

Figure 2.10. ^{15}N CEST profiles of FUS-RRM in absence (cyan) and presence (red) of 1M urea. The vertical dashed lines show the large chemical shift changes between the ground (GS) and the excited state (ES). The obtained χ^2_{red} is of 1.5 using a fit to a two-state model.

Further, on comparing the Δω (between the random coil backbone ^{15}N chemical shifts of FUS-RRM predicted by POTENCI (19) and native chemical shifts) with the Δω derived using ^{15}N-CEST, with those measured using ^{15}N-CEST, we find a strong correlation ($R^2 = 0.76$) between the two datasets. This indicates that ES^{CEST} represents an unfolded conformation (Figure. 2.11B).

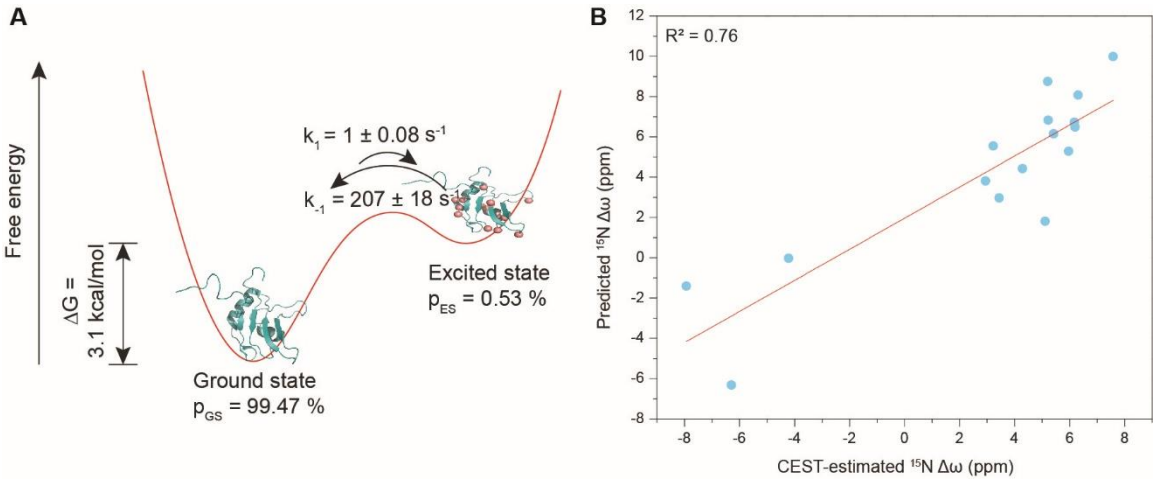

Figure 2.11. The excited state of FUS-RRM, as detected by ^{15}N-CEST, corresponds to an unfolded state. (A) A cartoon representation of the energy landscape of FUS-RRM showing the two states and their interconversion rates with fractional populations. (B) A residue-wise correlation between Δω values obtained from POTENCI ($\omega_{random\text{-}coil} - \omega_{folded}$) and that derived from the ^{15}N-CEST measured at pH 6.4 ($\omega_{ES} - \omega_{GS}$).

We then compared the $\Delta G_{GS\text{-}ES}$ as obtained using ^{15}N-CEST experiment with the $\Delta G_{unfolding}$ calculated using urea-induced unfolding of the FUS-RRM as measured by far-UV CD spectroscopy (Figure 2.12). The $\Delta G_{unfolding}$ was found to be 4.8 kcal/mol confirming that the ES^{CEST} is somewhere between the folded and unfolded state and thus is assigned to a partially unfolded state.

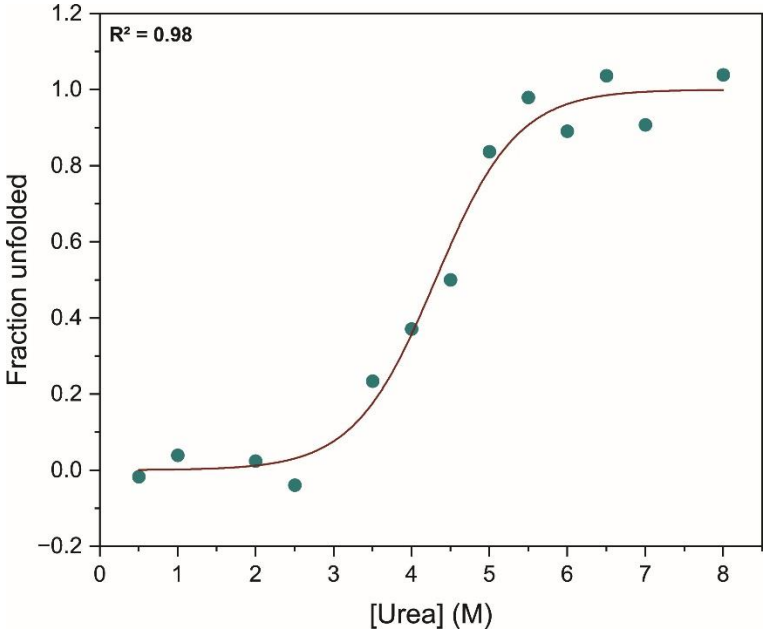

Figure 2.12. Two-state (folded and unfolded) fit to the plot of fraction unfolded (measured using far-UV CD) vs urea concentration to obtain $\Delta G_{unfolding}$.

2.4 Discussion

The above results provide important insights into the conformational dynamics of FUS-RRM. By combining CEST, $R_{1\rho}$ and $R_{2\rho}$ relaxation dispersion, and global fitting of exchange parameters, this study uncovers the existence of different excited states in the FUS-RRM domain. The presence of 6% of ES^{HARD} as compared to only 0.14% of ES^{CEST} indicates that FUS-RRM prefers fast µs-ms dynamics. This preference likely contributes to its weak binding with different types of nucleic acids. However, very low population of ES^{CEST} could also be important for bringing significant structural changes and driving aggregation, a process associated with slower timescales of motion. A good correlation between predicted ^{15}N Δω of the unfolded protein and the CEST-estimated Δω, suggests that the ES^{CEST} represents a partially unfolded or locally disordered ensemble. This is also supported by the stabilization of the ES^{CEST} in the presence of 1 M urea and by urea-induced unfolding monitored by CD.

ThT kinetics and AFM data show that the M (GS) goes to the A state upon agitation. The ES^{HARD}/ES^{CEST} could be an on- or off-pathway intermediate to aggregation. To fully understand the pathway, it is necessary to perturb either the monomer or the excited state, which is the next direction of this thesis. We propose that the conformational heterogeneity observed in the M-state is linked with the formation of the fibrils (Figure 2.13). Thus, the next question arises: what is the possible pathway to aggregation?

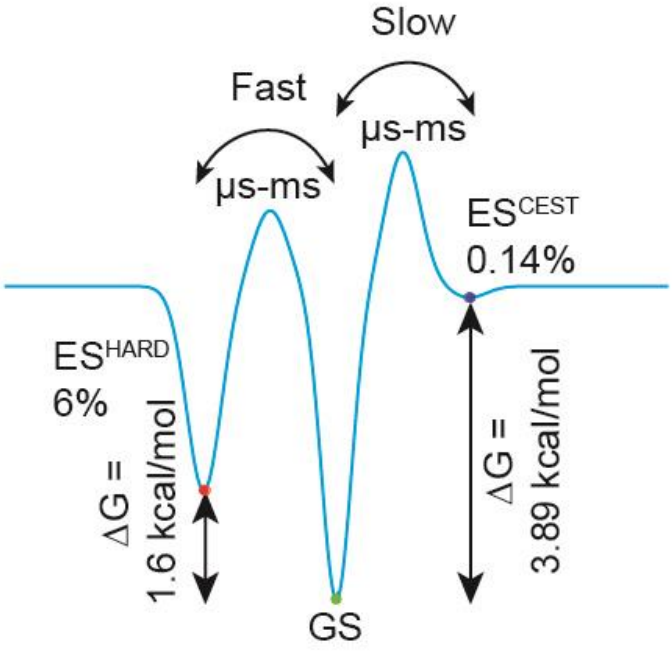

Figure 2.13. Conformational heterogeneity of FUS-RRM as measured by HARD $R_{1\rho}/_{2\rho}$ and CEST experiments at pH 6.4 and the corresponding ΔG between GS and the two ES states.

To answer this, an external perturbation is required to cause a change in the dynamics. If the dynamics are perturbed, which leads either to a change in fibril state or the kinetics of fibril formation, then it strongly supports a coupling of conformational heterogeneity with the fibril formation, and if it does not, then there exists no such coupling. We next wanted to identify a suitable perturbation that would only affect the exchange dynamics between GS and ES without perturbing the overall fold of the protein.

2.5 References

1. Lu Y, Lim L, Song J. RRM domain of ALS/FTD-causing FUS characteristic of irreversible unfolding spontaneously self-assembles into amyloid fibrils. Scientific reports. 2017;7(1):1043.
2. Bhatia S, Krishnamoorthy G, Dhar D, Udgaonkar JB. Observation of Continuous Contraction and a Metastable Misfolded State during the Collapse and Folding of a Small Protein. Journal of molecular biology. 2019;431(19):3814-26.
3. Raab SA, El-Baba TJ, Woodall DW, Liu W, Liu Y, Baird Z, et al. Evidence for Many Unique Solution Structures for Chymotrypsin Inhibitor 2: A Thermodynamic Perspective Derived from vT-ESI-IMS-MS Measurements. J Am Chem Soc. 2020;142(41):17372-83.
4. Vallurupalli P, Bouvignies G, Kay LE. Studying "invisible" excited protein states in slow exchange with a major state conformation. J Am Chem Soc. 2012;134(19):8148-61.
5. Vallurupalli P, Sekhar A, Yuwen T, Kay LE. Probing conformational dynamics in biomolecules via chemical exchange saturation transfer: a primer. J Biomol NMR. 2017;67(4):243-71.
6. Fawzi NL, Ying J, Ghirlando R, Torchia DA, Clore GM. Atomic-resolution dynamics on the surface of amyloid-β protofibrils probed by solution NMR. Nature. 2011;480(7376):268-72.
7. Tugarinov V, Ceccon A, Clore GM. NMR methods for exploring 'dark' states in ligand binding and protein-protein interactions. Progress in nuclear magnetic resonance spectroscopy. 2022;128:1-24.
8. Hansen DF, Vallurupalli P, Kay LE. An improved 15N relaxation dispersion experiment for the measurement of millisecond time-scale dynamics in proteins. The journal of physical chemistry B. 2008;112(19):5898-904.
9. Ishima R, Torchia DA. Extending the range of amide proton relaxation dispersion experiments in proteins using a constant-time relaxation-compensated CPMG approach. J Biomol NMR. 2003;25(3):243-8.
10. Korzhnev DM, Orekhov VY, Kay LE. Off-resonance R(1rho) NMR studies of exchange dynamics in proteins with low spin-lock fields: an application to a Fyn SH3 domain. J Am Chem Soc. 2005;127(2):713-21.
11. Palmer AG, 3rd, Massi F. Characterization of the dynamics of biomacromolecules using rotating-frame spin relaxation NMR spectroscopy. Chemical reviews. 2006;106(5):1700-19.
12. Iwahara J, Clore GM. Detecting transient intermediates in macromolecular binding by paramagnetic NMR. Nature. 2006;440(7088):1227-30.

13. Delaglio F, Grzesiek S, Vuister GW, Zhu G, Pfeifer J, Bax A. NMRPipe: a multidimensional spectral processing system based on UNIX pipes. J Biomol NMR. 1995;6(3):277-93.
14. Lee W, Rahimi M, Lee Y, Chiu A. POKY: a software suite for multidimensional NMR and 3D structure calculation of biomolecules. Bioinformatics. 2021;37(18):3041-2.
15. Liu X, Niu C, Ren J, Zhang J, Xie X, Zhu H, et al. The RRM domain of human fused in sarcoma protein reveals a non-canonical nucleic acid binding site. Biochim Biophys Acta. 2013;1832(2):375-85.
16. Spyracopoulos L. A suite of Mathematica notebooks for the analysis of protein main chain 15N NMR relaxation data. J Biomol NMR. 2006;36(4):215-24.
17. Guenneugues M, Berthault P, Desvaux H. A method for determining B1 field inhomogeneity. Are the biases assumed in heteronuclear relaxation experiments usually underestimated? J Magn Reson. 1999;136(1):118-26.
18. Wishart DS, Case DA. Use of chemical shifts in macromolecular structure determination. Methods Enzymol. 2001;338:3-34.
19. Nielsen JT, Mulder FAA. POTENCI: prediction of temperature, neighbor and pH-corrected chemical shifts for intrinsically disordered proteins. J Biomol NMR. 2018;70(3):141-65.
20. Horcas I, Fernandez R, Gomez-Rodriguez JM, Colchero J, Gomez-Herrero J, Baro AM. WSXM: a software for scanning probe microscopy and a tool for nanotechnology. Rev Sci Instrum. 2007;78(1):013705.
21. Rocco AG, Mollica L, Ricchiuto P, Baptista AM, Gianazza E, Eberini I. Characterization of the protein unfolding processes induced by urea and temperature. Biophys J. 2008;94(6):2241-51.
22. Patra D, Paul J, Rai U, P SA, Deshmukh MV. Conformational Plasticity in dsRNA-Binding Domains Drives Functional Divergence in RNA Recognition. J Am Chem Soc. 2025;147(20):17088-100.

Chapter 3: pH-perturbation on dynamics and FUS-RRM fibril formation

3.1 Introduction

The maintenance of the intracellular pH (pHi) is important for all cellular functions, and small changes in intracellular pH can significantly impact all cellular processes. During tissue inflammation, the accumulation of lactic acid results in a marked reduction in pH. For example, during severe ischemia, the brain pH can be as low as pH 6 (1). Consistent with this, it can be stated that the cytosolic pH is tightly regulated with the involvement of plasma membrane electroneutral ion transport proteins.

Reduced pHi is also a hallmark of several diseases including cancers of different tissue types and a number of neurodegenerative disorders (2, 3). There is ample evidence of structure-based regulation by pH for ion channels (4), ion transport proteins and pumps (5), and enzymes (6). The protonation state of titratable residues defines the electrostatic energy of molecular interactions. Also, pH puts a constraint for protein localization, including the recruitment of cytosolic proteins to plasma membrane or to intracellular membranes (7). In mammalian cells, the cytoplasm, nucleus, and endoplasmic reticulum have neutral pH, mitochondria are basic, and lysosomes, endosomes, and the Golgi apparatus are acidic (8).

The thermodynamic stability of protein conformations results from a delicate balance between electrostatic interactions, hydrophobic forces, and the environmental cues perturbing these interactions (9-11). A change in pH is one such perturbation that can disrupt this balance, leading to structural transitions and functional alterations in proteins (Figure 3.1). For example, low pH can enhance amyloid formation in the case of the prion protein (12). A change in the pH can affect the folding pathway of mouse prion protein (13). Low pH causes BSA to exhibit increased hydrophobicity, which facilitates its aggregation (14). Likewise, low pH has been shown to inhibit amyloid formation by an amyloidogenic protein, hIAPP (15).

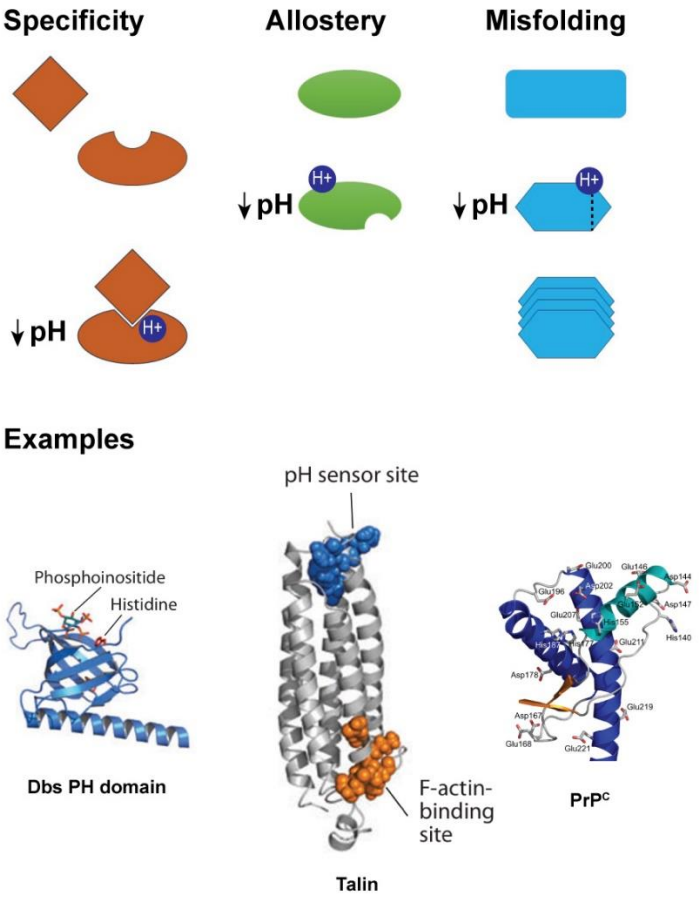

Figure 3.1. pH can regulate different cellular functions. Protonation and deprotonation have profound effects on binding affinity, allostery and protein misfolding (16).

Out of different pH values tested for the FUS-RRM domain, we observed that the pH change from 6.4 to 4.6 caused minimal perturbation to the protein backbone fold and thermal stability (Figure 3.2) but could effectively perturb the exchange dynamics. Further decreasing the pH led to broadening of the peaks in the HSQC spectrum. Thus, we used the pH 4.6 condition as an external perturbation to test the hypothesis proposed in Chapter 2 of this thesis.

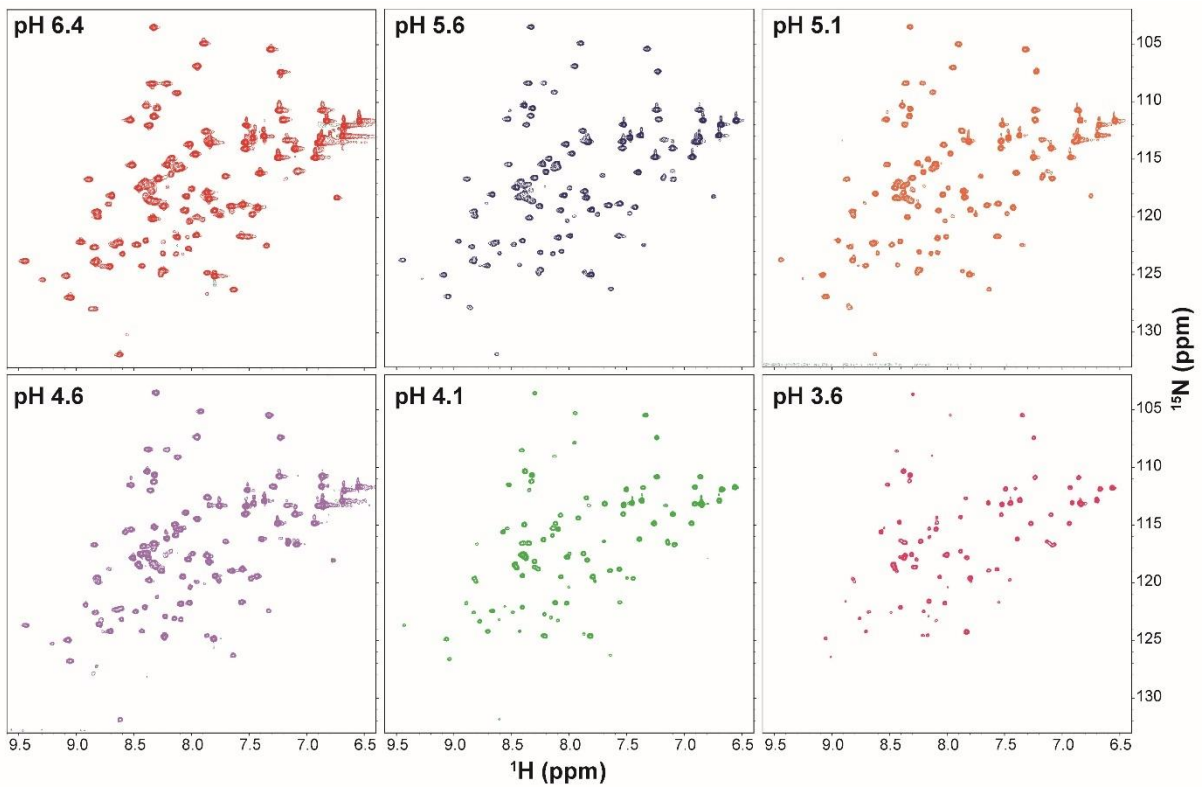

Figure 3.2. pH-dependent ^{15}N-^{1}H HSQC of FUS-RRM.

3.2 Methods

For this study, the recombinant FUS-RRM protein at pH 6.4 was buffer exchanged to pH 4.6 using acetate buffer containing 20 mM acetate and 100 mM NaCl.

3.2.1 NMR Spectroscopy

All the NMR experiments were recorded in a similar way to those recorded for the protein at pH 6.4 (as described in Chapter 2). For $R_{2\rho}$ experiments, the relaxation delays used were 0, 16, 32, 64, and 128 ms.

3.2.2 Chemical shift perturbation (CSP)

The chemical shift perturbations (CSPs) between pH 6.4 and pH 4.6 were calculated in POKY (17) using the following equation:

$$CSP = \sqrt{\left(\Delta\delta\ ^{1}H\right)^{2} + \left(\frac{\Delta\delta^{15}N}{5}\right)^{2}} \qquad \text{eq 3.1}$$

where, Δδ is the chemical shift difference between the resonances in 2D ^{15}N-^{1}H HSQC measured at the two pH values.

3.2.3 Circular dichroism (CD) spectroscopy

Far-UV CD spectroscopy was recorded on a Jasco-815 spectrometer equipped with a thermal controller for 20 μM protein in a 1 mm path length quartz cuvette with a bandwidth of 1 nm. The scans were acquired from 200-260 nm with a scanning speed of 50 nm/min. Data have been represented as Mean ± SD of three independent experiments after blank subtraction. The secondary structures from the CD spectrum were deconvoluted using BeStSel (18).

3.2.4 Fluorescence spectroscopy

Tryptophan fluorescence for different pH values with 20 μM FUS-RRM protein was carried out on a Fluoromax-4 spectrofluorometer (Horiba Scientific). The fluorescence spectrum for each sample was obtained by exciting tryptophan at 280 nm and collecting emission spectrum from 290-500 nm with slit widths: excitation at 5 nm and emission at 1 nm. Data have been represented as Mean ± SD of three independent experiments after blank subtraction.

3.2.5 8-Anilinio-1-naphthalenesulphonic acid (ANS) fluorescence spectroscopy

A stock solution of ANS was prepared in MilliQ water. The concentration of ANS was measured by absorbance at 350 nm using an extinction coefficient of 5000 M^{-1} cm^{-1}. Briefly, 10 μM of the protein was incubated with 100 μM of ANS for 15 minutes at room temperature. The experiment was carried out on a Fluoromax-4 spectrofluorometer (Horiba Scientific). The emission spectra were recorded by exciting ANS at 380 nm and collecting emission spectra from 400 to 700 nm. The slits used were 1 and 8 nm for excitation and emission, respectively. Data have been represented as Mean ± SD of three independent experiments after blank subtraction.

3.2.6 Thermal stability

The thermal stability of the FUS-RRM protein was measured using Peltier attached to CD instrument (JASCO-815). The temperature was varied from 15°C to 80°C. 20 μM sample in a 1 mm path length quartz cuvette was incubated for 10 minutes at each temperature, and then far-UV CD spectra were recorded. The scans were acquired from 200-260 nm with a bandwidth of 1 nm and scanning speed of 50 nm/min. The molar ellipticity at 207 nm was used to monitor the unfolding and used in the analysis in Origin.

3.2.7 Aggregation kinetics

The aggregation kinetics at pH 4.6 were measured in a similar way as described in Chapter 2.

3.2.8 AFM imaging

AFM imaging was performed similarly for FUS-RRM domain at pH 4.6, as described in Chapter 2.

3.3 Results

3.3.1 Adiabatic $R_{1\rho}$ and $R_{2\rho}$ for characterisation of fast µs-ms dynamics

The adiabatic $R_{1\rho}$ and $R_{2\rho}$ relaxation rates were measured at pH 4.6 (Figure 3.3). The dispersion rates significantly reduced for $R_{2\rho}$ at pH 4.6 (Figure 3.3A), suggesting the rigidification of the protein at this timescale. Upon fitting to a two-state model, k_{ex} rates and excited state population were determined. The protein indeed is rigidified at pH 4.6, as observed by a significant decrease in k_{ex} (0.1-2 x 10^3 s^{-1}) (Figure 3.3B). The population of the ground state (M) increased significantly (average p_M = 98%) (Figure 3.3C). This indicates that pH perturbation significantly quenched the conformational exchange to the excited state (ES^{HARD}).

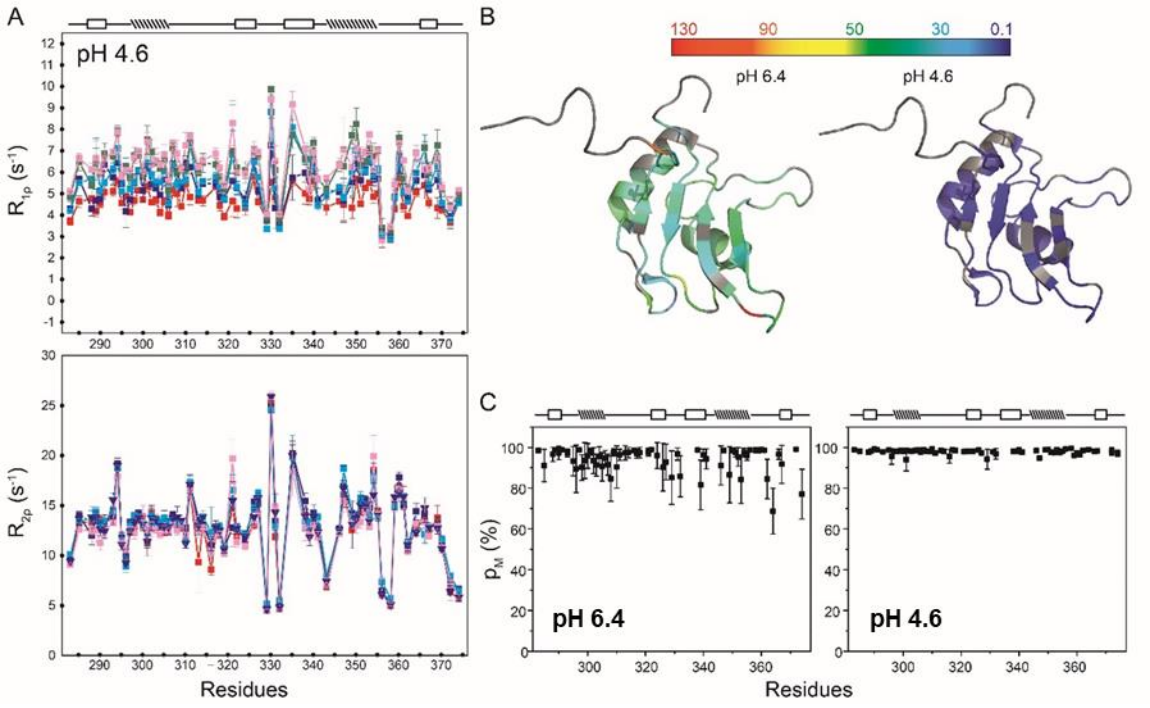

Figure 3.3. pH-induced dynamic perturbations in the FUS-RRM domain. (A) The $R_{1\rho}$ and the $R_{2\rho}$ relaxation rates measured for FUS-RRM monomer at pH 4.6 at 25 °C. (B) A comparison of k_{ex} rates mapped to the FUS-RRM tertiary structure for pH 6.4 and pH 4.6. The residues highlighted in grey do not fit to any model and hence are not included in the discussion. (C) The population of the ground state for pH 6.4 and pH 4.6. The secondary structure of FUS-RRM is indicated above the plots depicted in A and C panels, with boxed and dashed rectangles denoting strands and helices, respectively.

In order to determine whether a residue has dispersion, we calculated $\Delta R_{1\rho} = R_{1\rho,\mathrm{HS8}} - R_{1\rho,\mathrm{HS1}}$ and $\Delta R_{2\rho} = R_{2\rho,\mathrm{HS1}} - R_{2\rho,\mathrm{HS8}}$, and plotted the results as a function of residue (Figure 3.4). If we compare the $\Delta R_{1\rho}$ and $\Delta R_{2\rho}$ we find that while $\Delta R_{1\rho}$ does not decrease significantly, $\Delta R_{2\rho}$ does decrease beyond the error bar on going from pH 6.4 to pH 4.6. The model fitting to extract k_{ex} and population is done using $R_{1\rho}$ and $R_{2\rho}$ together, and thus the effect of perturbation in at least one of the data sets is a necessary and sufficient condition to cause the observed perturbation in k_{ex} and population.

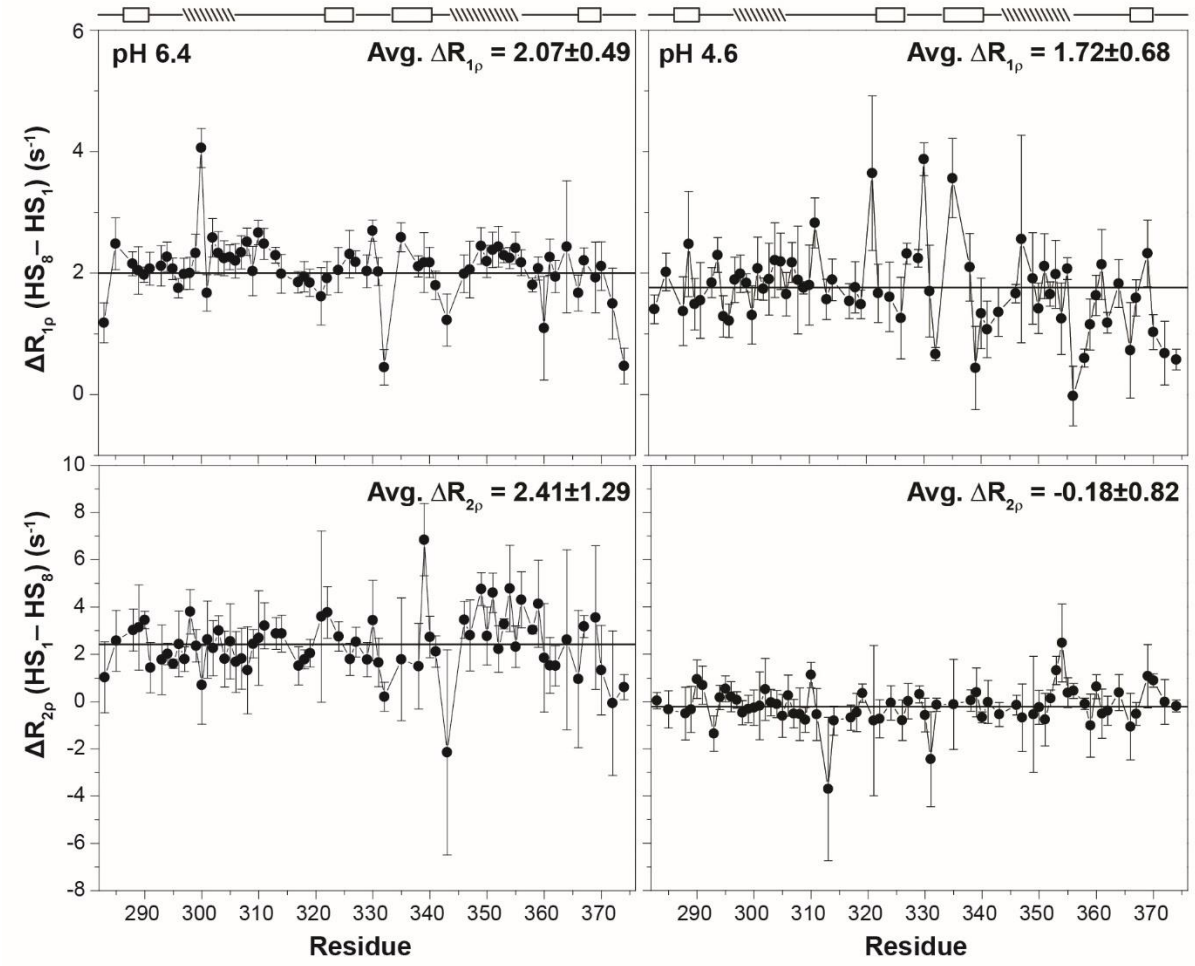

Figure 3.4. $\Delta R_{1\rho}$ and $\Delta R_{2\rho}$ measured at two stretching factors, HS1 and HS8, of adiabatic pulse to highlight the relaxation dispersion observed at different residues and at two different pH values (6.4 and 4.6). Average values have been marked using a horizontal line. The secondary structure is shown on the top of each panel with boxed and dashed rectangles denoting strands and helices, respectively.

3.3.2 Characterisation of slow µs-ms dynamics using ^{15}N CEST at pH 4.6

Since, we had earlier observed pH-induced quenching of a fast µs timescale excited state (ES^{HARD}) in FUS-RRM by ^{15}N HARD measurements, we probed the pH-induced perturbation on the excited state using ^{15}N-CEST (ES^{CEST}). The ^{15}N CEST profiles observed at pH 4.6 are

similar to those at pH 6.4, as shown in (Figure 3.5), though fewer residues with minor dips were identified. After global fitting in ChemEx, a k_{ex} of 142 ± 36 s^{-1} and p_{ES} of 0.5 ± 0.06% were obtained.

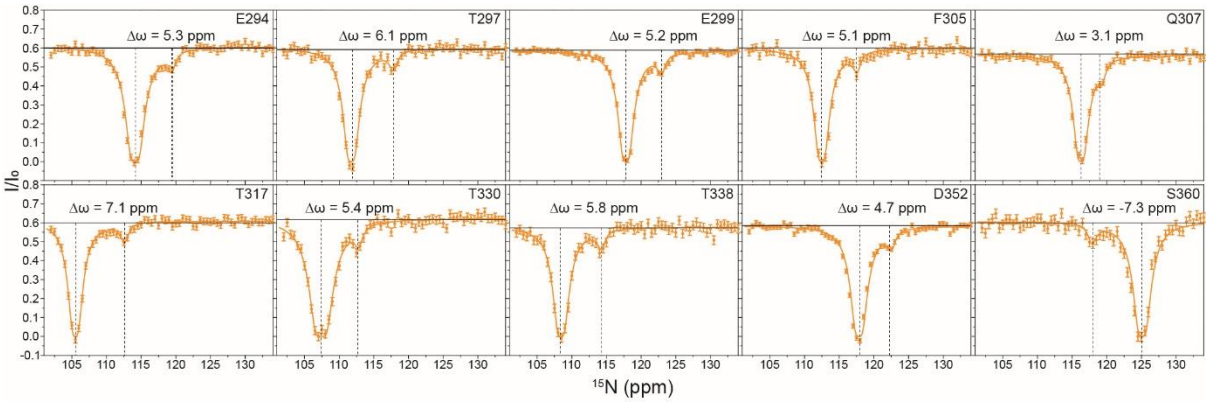

Figure 3.5. ^{15}N CEST profiles of FUS-RRM indicates the presence of a conformationally excited state, pH 4.6. Solid lines represent the global fit to CEST data, while dashed lines represent the chemical shift of the ground and excited state. The obtained χ^2_{red} is of 1.3 using a fit to a two-state model.

Figure 3.6B shows a cartoon representation of the free energy of interconversion to the excited state. Compared to pH 6.4, ΔG reduces from 3.9 kcal/mol to 3.13 kcal/mol, indicating a more stable interconversion.

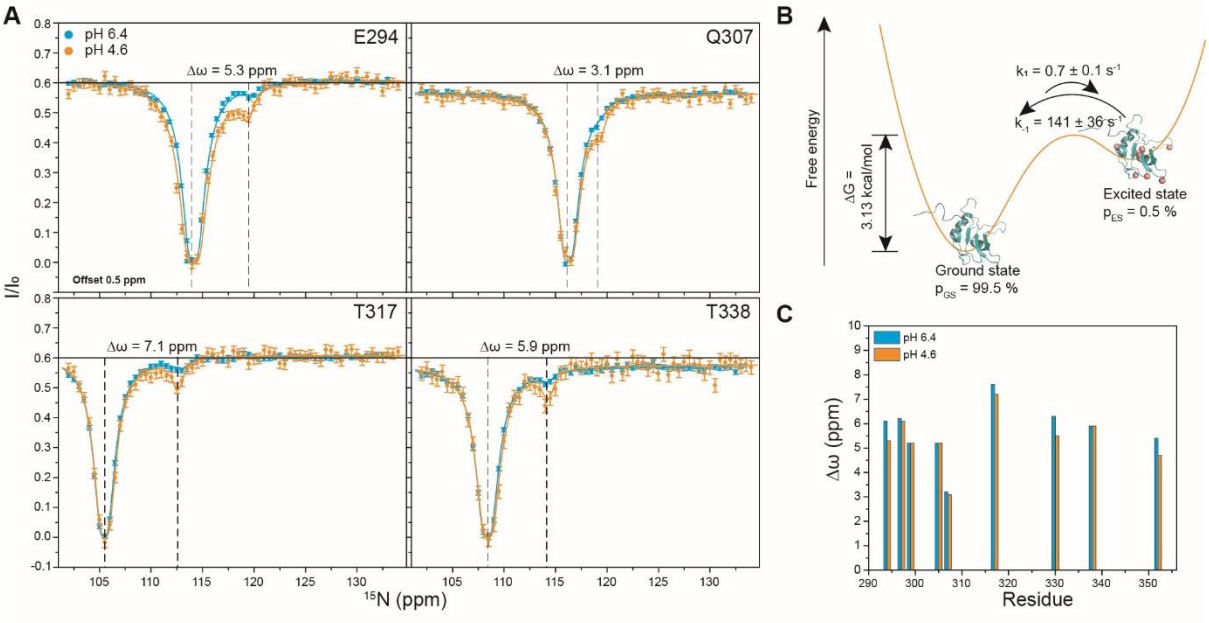

Figure 3.6. The characterisation of the slow µs-ms dynamics in FUS-RRM domain using ^{15}N CEST at pH 4.6. (A) The comparison of the ^{15}N CEST profiles of representative FUS-RRM residues at both pH values (pH 4.6 and 6.4, respectively). The vertical dashed lines show the large chemical shift changes between the ground (GS) and the excited state (ES) (B) The energy landscape of FUS-RRM showing the two states and their interconversion rates with fractional populations at pH 4.6. (C) A comparison of the delta omega (Δω) values at pH 4.6 (orange) and 6.4 (cyan).

The residues undergoing exchange exhibit similar Δω values (Figure 3.6C), suggesting comparable but significant structural rearrangements. These residues belong to different

clusters, residues N284-I287, T313-T317, L324-G331, and E336-V339 which are located within or near the known interaction interface of FUS-RRM with nucleic acids and/or ATP (19) (Figure 3.7). This suggests that although the dynamic residues are spatially dispersed, they may contribute collectively to functionally relevant interactions.

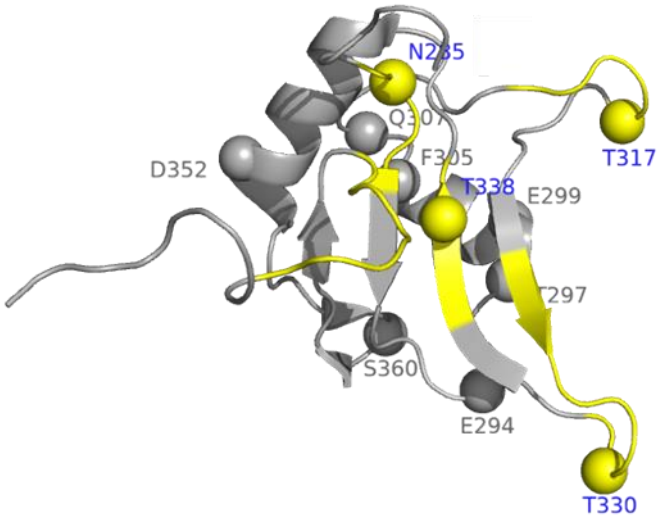

Figure 3.7. The mapping of the residues in FUS-RRM domain that undergo slow µs-ms exchange to known nucleic acid-binding clusters (highlighted in yellow), and the residues belonging to that particular cluster have been shown with the help of yellow spheres.

3.3.3 pH-induced structural perturbations

We have observed differences in the dynamics at two timescales (fast and slow µs-ms) of motions, which could also be attributed to a change in the monomer itself, such as a change in secondary or tertiary structures that affects residues involved in fibril formation. To investigate that further, we performed various experiments to check the overall fold of the FUS-RRM at the two pH values 4.6 and 6.4, respectively. CD and fluorescence spectroscopy were performed to find changes in secondary or tertiary structure. Figure 3.8A compares the far-UV CD spectroscopy data for the FUS-RRM domain at pH 6.4 and pH 4.6, respectively, which shows similar spectra with a prominent dip at 207 nm (Table S2). Figure 3.8B shows the tryptophan fluorescence with fluorescence maxima observed at 355 nm for the protein at both pH values, indicating that the tertiary structure remains largely unchanged. Further ANS fluorescence was used to test the change in hydrophobic packing at the lower pH. Figure 3.8C shows that upon ANS binding at pH 4.6, there is no major change in intensity but a slight blue-shift in the wavelength (from 523 nm to 518 nm). The only difference at low pH could be attributed to an increased unfolded characteristics or to its interaction with the polar groups present on the surface. These observations imply that the unfolding is partial and does not lead to significant

exposure of hydrophobic patches. Similarly, the heat-induced unfolding was monitored to estimate the midpoint of unfolding (T_m) to measure stability. Figure 3.8D shows that the protein at both the pH values exhibits a similar T_m of 50-55°C. These results show that the protein exhibits similar fold and stability at both pH 4.6 and 6.4.

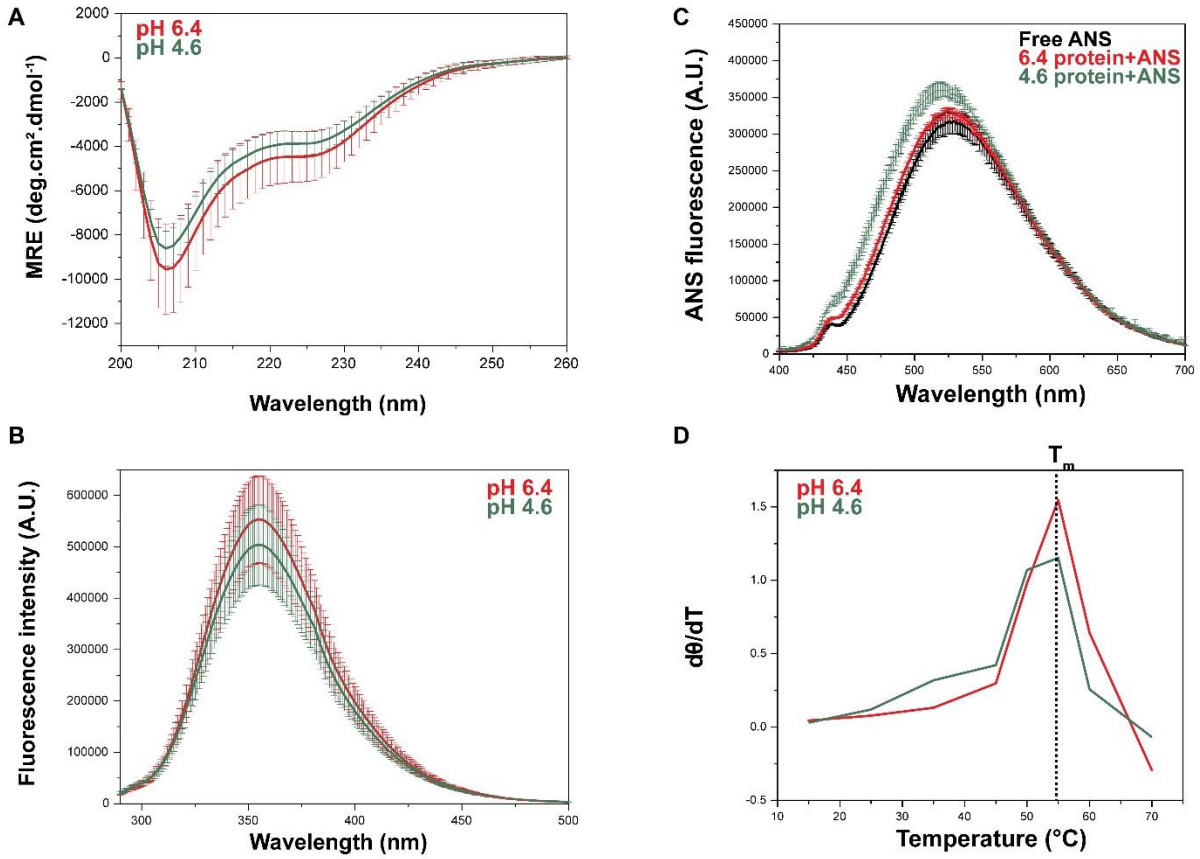

Figure 3.8. pH-induced global structural perturbations in FUS-RRM domain. (A) Comparison of far-UV CD spectroscopy data obtained for FUS-RRM at pH 6.4 (red) and pH 4.6 (green). (B) Tryptophan fluorescence spectroscopy for FUS-RRM domain at pH 6.4 (red) and pH 4.6 (green). (C) ANS fluorescence measurement for FUS-RRM protein at pH 6.4 (red) and pH 4.6 (green). (D) The thermal stability for FUS-RRM protein, as measured by the first derivative of the signal obtained at 207 nm upon CD melting at pH 6.4 (red) and pH 4.6 (green). The data have been represented as Mean ± SD of three independent experiments after blank subtraction (except for thermal stability check).

We also performed 2D ^{15}N-^{1}H HSQC, and found that the protein remained well-folded at both pH 4.6 (green) and 6.4 (red) (Figure 3.9A). Figure 3.9B shows the chemical shift perturbations (CSPs) from pH 6.4 to pH 4.6 for the backbone amides. The twelve residues showing CSPs above the plus one standard deviation (SD) line have been considered to be significantly perturbed and have been mapped on the tertiary structure of the protein (Figure 3.9C). It indicates that out of the twelve residues, ten residues are surface-exposed and thus may not perturb the overall tertiary fold of the molecule. These results indicate that the protein

structure of the state M is only minimally perturbed, while the exchange dynamics between M and ES is significantly quenched.

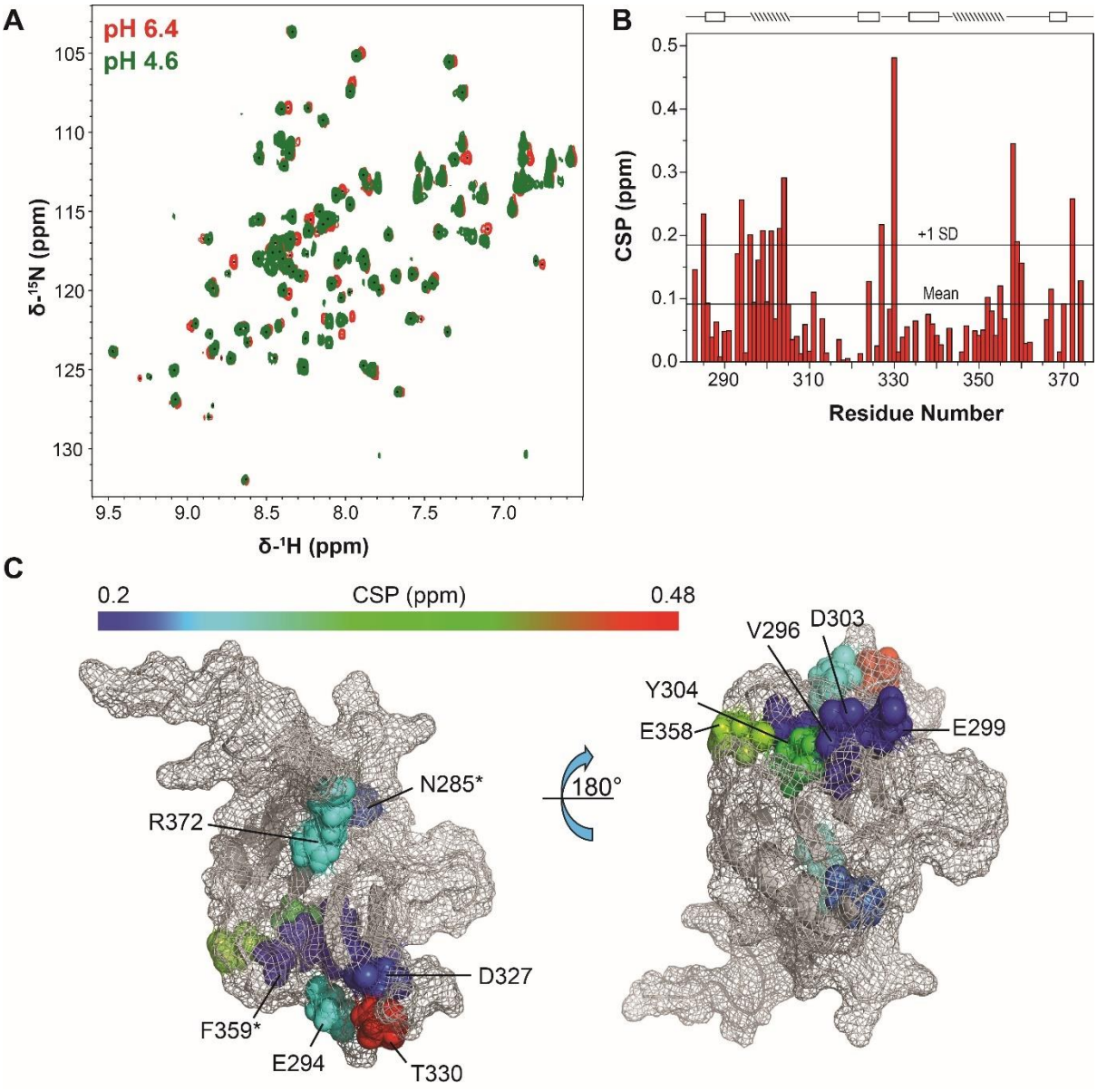

Figure 3.9. pH-induced global structural perturbations in the FUS-RRM domain. (A) An overlay of 2D ^{15}N-^{1}H HSQC for FUS-RRM recorded at pH 6.4 (red) and at pH 4.6 (green). (B) The chemical shift perturbation obtained from ^{15}N-^{1}H chemical shifts plotted against the residue number for FUS-RRM, as described in Methods. Two horizontal lines show the mean and the Mean ± 1 SD. The residues showing CSPs above the mean ± 1 SD line have been considered as significantly perturbed. The secondary structure is shown on the top with boxed and dashed rectangles denoting strands and helices, respectively. (C) The twelve significantly perturbed residues obtained from (B) have been mapped on the tertiary structure to indicate that ten of these residues are surface-exposed and do not perturb the overall tertiary fold of the molecule. The color gradient shows the extent of CSPs within the 12 residues. The residues marked with stars (N285 and F359) are buried inside.

We tested the pH-induced perturbations to the fast dynamics (ps-ns timescale motions) using traditional T_1 (=1/R_1), T_2 (=1/R_2), and [^{1}H]-^{15}N nOe experiments. It can be seen that the fast dynamics – to which R_1, R_2, and [^{1}H]-^{15}N nOe experiments are sensitive – is not significantly perturbed by the pH

(Figure 3.10). The average values for R_1 remain well within one standard deviation. For the R_2 and nOe, the average values remain within two standard deviations due to two residues in the loop being significantly perturbed. In addition to the motion of the NH bond vector, the fast dynamics also provide information on the rotational correlation time of the protein, which in turn reports on the overall size of the molecule. Thus, similar average values of R_1, R_2, and [^{1}H]-^{15}N nOe parameters at two pH values suggest that the change in the pH does not perturb the overall size of the molecule in solution.

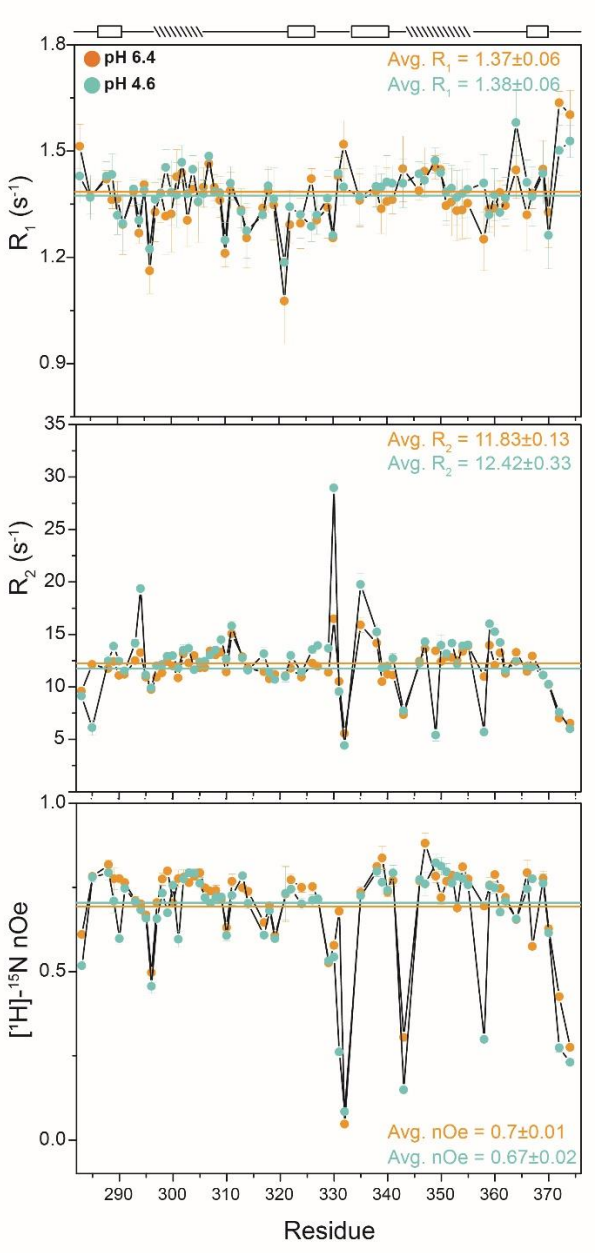

Figure 3.10. Overlay of the R_1 (=1/T_1), R_2 (=1/T_2) and [^{1}H]-^{15}N nOe relaxation rates measured for FUS-RRM at pH 6.4 and 4.6. The average line has been shown on the data, and the average values for the rates have been mentioned in the figure. The secondary structure is shown on the top with boxed and dashed rectangles denoting strands and helices, respectively.

3.3.4 pH-induced perturbation on aggregation kinetics

Subsequently, we investigated the impact of pH variation on aggregation kinetics. Figures 3.11A and 3.11B illustrate the concentration-dependent aggregation kinetics for FUS-RRM domain using ThT at pH 6.4 and 4.6, respectively. Notably, the protein exhibited accelerated aggregation kinetics at pH 4.6, characterized by a significant reduction in lag time compared to pH 6.4. The lag time significantly decreased from 54 hours to 8.5 hours at a concentration of 25 µM (Table S1). Intriguingly, at pH 4.6, the lag time was eliminated across all concentrations suggesting the role of secondary nucleation (or saturated secondary nucleation) in enhancing aggregation. However, there was an overall decrease in ThT intensity at pH 4.6, which could be attributed to structural or morphological differences and hence also modifying the rate of aggregation.

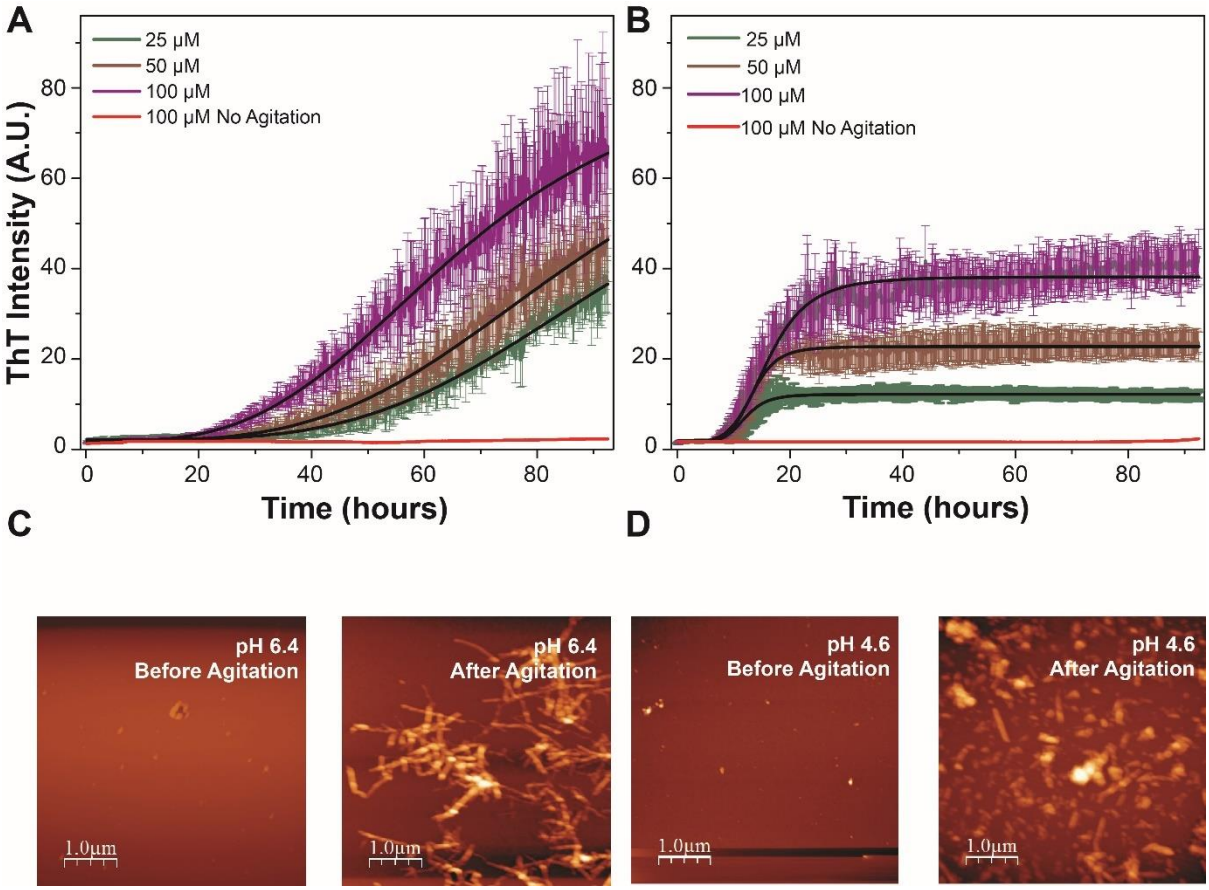

Figure 3.11. Aggregation kinetics for the FUS-RRM as measured by monitoring ThT intensity while agitation at (A) pH 6.4 and (B) pH 4.6. The data have been represented as Mean ± SD of three independent experiments. The solid line represents the fit to the kinetics data. Fibril formation for FUS-RRM as imaged by AFM at (C) pH 6.4 and (D) pH 4.6. AFM measurement on protein samples without agitation shows no fibril formation.

3.3.5 pH-induced perturbation in the fibril state

The corresponding AFM images at the two pH values reveal observable differences in fibril morphologies. At pH 6.4, we observe mostly the fibrils (~0.6 µm), while at pH 4.6 we find a

mixture of aggregates, comprising of both smaller fibrils and amorphous aggregates (Figures 3.11C and 3.11D). We strongly believe that the altered fibril morphologies at the two-pH used in this study, may explain the observed differences in the aggregation kinetics. Also, the differences in the dynamics due to pH perturbations can lead to varied local folding, which may affect aggregate formation. It is tempting to speculate that the observed variability in the aggregate formation may be due to differences in the excited state structural propensities which needs further investigation.

3.4 Proposed model

So far, the study indicates that FUS-RRM undergoes different timescales of motions. It also populates different excited states, populations of which depend upon external perturbations. Using adiabatic $R_{1\rho/2\rho}$ experiment, we find ES^{HARD} as the major population and a very low population of ES^{CEST} at pH 6.4, and a change in pH results in an increase in the population of the $ES^{CEST,}$ suggesting more stabilization. Further, depending on the stability of the ES state, the final fibrillar state gets modulated. ES^{HARD} promotes fibril-like formation while ES^{CEST} leads to a mixture of aggregates.

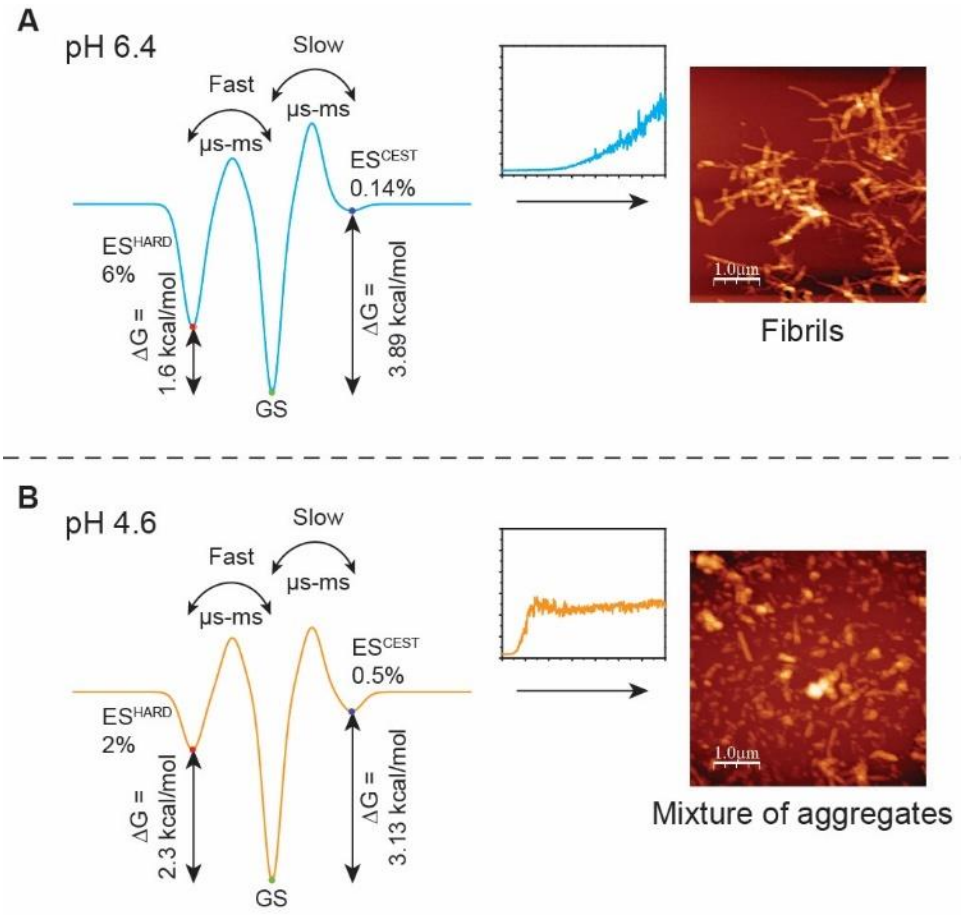

Figure 3.12. A cartoon representation of the free energy differences between GS and ES at pH 6.4 (A) and 4.6 (B), where corresponding populations have been mentioned. A perturbation in the conformational heterogeneity is shown to be coupled with the fibril state achieved upon agitation, with differences in the fibril formation.

3.5 Discussion

The data show that the external perturbation (a decrease in pH) quenches the intrinsic exchange dynamics between M (GS) and ES^{HARD} (as measured using $R_{1\rho}$ and $R_{2\rho}$ NMR experiments), which leads to an increase in the M population and also enhances fibril formation rates. A noteworthy finding from ^{15}N CEST is the presence of similar ES^{CEST} at both pH values, although it is populated very lowly at pH 6.4. This low population of ES^{CEST} could be involved in primary nucleation, and an increase will thus result in faster aggregation. This is what we observe at pH 4.6. However, from the ThT profiles at pH 4.6, we can also say the involvement of secondary nucleation in enhancing the aggregation.

We have shown that the structure of the monomer at both pH 6.4 and 4.6 remains similar (shown by far-UV CD, tryptophan fluorescence, 2D ^{15}N-^{1}H HSQC NMR spectroscopy, and T_1 ($=1/R_1$), T_2 ($=1/R_2$), and [^{1}H]-^{15}N nOe experiments). Since perturbation in all these experiments is within the error bar, it is safe to believe that the monomer conformation is minimally perturbed.

Despite monomer conformation being similar, the accelerated kinetics at pH 4.6 can be attributed to charge imbalance by the surface residues, which is highlighted by the high CSP values observed for such residues and some of these residues (N285, E294, T330) are also involved in slow conformational exchange as measured by CEST, suggesting a role in primary nucleation. Consistent with this, ANS fluorescence measurements show a subtle blue shift accompanied by a slight increase in fluorescence intensity, indicating partial structural rearrangements rather than extensive hydrophobic exposure. These observations are in agreement with the ^{15}N-CEST results, which indicate an increased population of a partially unfolded state. Together with charge-driven surface destabilization, these effects underlie the enhanced kinetic behaviour observed at low pH.

The morphology of the fibrils formed in the two buffer conditions are very different. Compared to pH 6.4, the AFM data showed an increased heterogeneity in the fibrils formed at pH 4.6. Mostly, we find a significant number of shortened fibrils of length <0.2 μm and amorphous aggregates. It remains to be established if the shorter fibrils formed at pH 4.6 are differently toxic to the cells and need to be explored. Such perturbations to conformational heterogeneity (and not structures and surface charges alone) as a function of pH might also be responsible for the loss or gain of related functions, which in this case is fibril formation by RRM.

Therefore, new strategies can be designed that can stabilise the ES^{HARD} or decrease the stability of the ES^{CEST}, to prevent amyloid formation.

3.6 References

1. Rehncrona S. Brain acidosis. Ann Emerg Med. 1985;14(8):770-6.
2. Harguindey S, Reshkin SJ, Orive G, Arranz JL, Anitua E. Growth and trophic factors, pH and the Na+/H+ exchanger in Alzheimer's disease, other neurodegenerative diseases and cancer: new therapeutic possibilities and potential dangers. Current Alzheimer research. 2007;4(1):53-65.
3. Syntichaki P, Samara C, Tavernarakis N. The vacuolar H+ -ATPase mediates intracellular acidification required for neurodegeneration in C. elegans. Curr Biol. 2005;15(13):1249-54.
4. Hu F, Luo W, Hong M. Mechanisms of proton conduction and gating in influenza M2 proton channels from solid-state NMR. Science (New York, NY). 2010;330(6003):505-8.
5. Hunte C, Screpanti E, Venturi M, Rimon A, Padan E, Michel H. Structure of a Na+/H+ antiporter and insights into mechanism of action and regulation by pH. Nature. 2005;435(7046):1197-202.
6. Gorfe AA, Caflisch A. Functional plasticity in the substrate binding site of beta-secretase. Structure (London, England : 1993). 2005;13(10):1487-98.

7. Chan P, Warwicker J. Evidence for the adaptation of protein pH-dependence to subcellular pH. BMC biology. 2009;7:69.
8. Casey JR, Grinstein S, Orlowski J. Sensors and regulators of intracellular pH. Nature reviews Molecular cell biology. 2010;11(1):50-61.
9. Mishra P, Patni D, Jha SK. A pH-dependent protein stability switch coupled to the perturbed pKa of a single ionizable residue. Biophys Chem. 2021;274:106591.
10. Pace CN. Polar group burial contributes more to protein stability than nonpolar group burial. Biochemistry. 2001;40(2):310-3.
11. Parvez F, Amin Z, Sangpal D, Chugh J. Role of pH in Modulating RNA-Protein Interactions in TRBP2-dsRBD2: An Interplay between Conformational Dynamics and Electrostatic Interactions. The journal of physical chemistry B. 2024;128(51):12698-709.
12. van der Kamp MW, Daggett V. Influence of pH on the human prion protein: insights into the early steps of misfolding. Biophys J. 2010;99(7):2289-98.
13. Moulick R, Goluguri RR, Udgaonkar JB. Ruggedness in the Free Energy Landscape Dictates Misfolding of the Prion Protein. Journal of molecular biology. 2019;431(4):807-24.
14. Lan H, Liu H, Ye Y, Yin Z. The Role of Surface Properties on Protein Aggregation Behavior in Aqueous Solution of Different pH Values. AAPS PharmSciTech. 2020;21(4):122.
15. Mishra R, Geyer M, Winter R. NMR spectroscopic investigation of early events in IAPP amyloid fibril formation. Chembiochem. 2009;10(11):1769-72.
16. Damaghi M, Wojtkowiak JW, Gillies RJ. pH sensing and regulation in cancer. Front Physiol. 2013;4:370.
17. Lee W, Rahimi M, Lee Y, Chiu A. POKY: a software suite for multidimensional NMR and 3D structure calculation of biomolecules. Bioinformatics. 2021;37(18):3041-2.
18. Micsonai A, Moussong E, Wien F, Boros E, Vadaszi H, Murvai N, et al. BeStSel: webserver for secondary structure and fold prediction for protein CD spectroscopy. Nucleic Acids Res. 2022;50(W1):W90-W8.
19. Liu X, Niu C, Ren J, Zhang J, Xie X, Zhu H, et al. The RRM domain of human fused in sarcoma protein reveals a non-canonical nucleic acid binding site. Biochim Biophys Acta. 2013;1832(2):375-85.

Chapter 4: ATP-induced perturbation on dynamics and fibrillation of FUS-RRM domain

4.1 Introduction

Adenosine 5′-triphosphate (ATP) acts as the major energy currency for many biochemical reactions within cells. ATP consists of an adenine base, a ribose sugar, and triphosphate chains with high-energy phosphate bonds. At ∼100 μM concentration, it is sufficient for most ATP-utilizing enzymes, while its physiological concentration (1−10 mM) is ~10- to 100-fold higher (1), thereby implying that its role in other essential physiological functions. During neurodegeneration, it has been suggested that mitochondria undergo alterations that lead to perturbation in ATP generation (2, 3). It has also been reported that high levels of proinflammatory cytokines increase ATP levels (4, 5). Several studies have reported that ATP plays an important role in modulating the fibrillation of amyloidogenic proteins including amyloid-β, tau, and FUS (6-9). High ATP in these cases increases the aggregation rate by mediating protein-protein interactions and liquid-liquid phase separation, while Patel et al. have proposed a new role for ATP in increasing the solubility of amyloidogenic proteins (10). These studies highlight that the role of ATP in amyloid fibrillation remains controversial and more studies are warranted on such systems.

In this chapter, we have tried to understand the role of ATP in modulating the conformational dynamics of FUS-RRM and its effect of FUS-RRM aggregation, in fast and slow μs-ms timescales.

4.2 Methods

4.2.1 Selective Optimized-Flip-Angle Short-Transient (SOFAST)-HMQC and data fitting in TITAN.

Multidimensional (nD) NMR is very useful to resolve spectral resolution of a large macromolecule. However, it is limited by the extensive time-consuming methods and involves multiple scans with stepwise incrementation of delay for each dimension. This result in long acquisition times and experimental time, up to several days. SOFAST-HMQC provides excellent sensitivity with short acquisition times (11). Fast data acquisition in SOFAST-HMQC is achieved by using very short inter-scan delays, small number of RF pulses, and longitudinal optimisation, which results in increased signal to noise ratio.

Taking the advantage of SOFAST-HMQC we recorded titration experiments with ATP and analysed the binding using TITAN (TITration ANalysis) software (12). Instead of just

using CSP to derive binding affinity, TITAN performs lineshape analysis to fit observed spectra to numerical solutions of the Bloch-McConnell or Liouville-von Neumann equations.

NMR spectra were collected with 690 x 128 total points in F_2 (^1H) and F_1 (^{15}N) dimensions. Spectral widths of 12 ppm (^1H) and 32 ppm (^{15}N) were used, for which an acquisition time of 48 ms was obtained in the direct dimension (F_2). All the NMR spectra were processed in NMRPipe (13) and used for TITAN analysis in NMRbox. The data was fitted globally to a two-state binding model by defining a region of interest (ROI) for different spins.

4.2.2 ^{15}N HARD

^{15}N HARD experiments were recorded for the FUS-RRM domain and analysed for different samples on the 600 MHz NMR spectrometer as described in Chapter 2.

The relaxation delays used for $R_{1\rho}$ and $R_{2\rho}$ were 0, 16, 32, 64, 128 and 176 ms. R_1 experiments were acquired similarly to $R_{1\rho}$ and $R_{2\rho}$ experiments but without using the adiabatic pulse during evolution. The delays used for the R_1 experiment were 0, 48, 96, 192, 320, 480, and 640 ms.

4.2.3 ^{15}N CEST

In order to reduce turbidity-related artifacts caused by ATP, the same sweep width as explained in Chapter 2 was used with a spacing of 30 Hz, but the total frequency points recorded were 26 using the equation as provided (14),

$$N = \frac{sw}{\Delta v_{1/2}^{min}} \qquad \text{eq 4.1}$$

where, *N* is the number of CEST frequency points, *sw* is the spectral width, and

$$\Delta v_{1/2}^{min}(Hz) = 2.15\frac{\omega_1}{2\pi} + 11.41 \qquad \text{eq 4.2}$$

where, $\frac{\omega_1}{2\pi}$ is the B_1 field strength.

The B_1 field was calibrated using the method described by Guenneugues et al. (15) and used for the analyses. Global line-shape fitting was carried out as described earlier in Chapter2 either by fixing p_{ES} or k_{ex}.

4.2.4 Aggregation kinetics

pH-dependent aggregation kinetics was assessed for FUS-RRM domain in 200 µL reactions with 50 µM purified protein and different molar equivalents of ATP, and 30 µM of thioflavin T (ThT) in aggregation buffer (10 mM sodium phosphate and/or sodium acetate, 100 mM NaCl, pH 6.4 and pH 4.6, respectively) at 25°C, with agitation at 60 rpm in a 96-well plate (Fluoroskan, Thermo Scientific). The fibril formation was monitored by continuously measuring the ThT intensity at 475 nm upon excitation at 440 nm.

4.2.5 TEM imaging

After kinetics data were recorded, the FUS-RRM samples were centrifuged, and the pellet was resuspended in Milli-Q water. Briefly, 5 µL of the sample was transferred to a 300-mesh Formvar carbon-coated copper grid and incubated for 3 minutes. After incubation, the solution was removed and the grid was negatively stained with uranyl acetate solution (1.5%). After 1 min, the solution was removed and grid was allowed to air-dry at room temperature before imaging with transmission electron microscopy (JEM-2200FS) (TEM) at an accelerating voltage of 200 kV.

4.3 Results

4.3.1 NMR titration study of ATP-binding to FUS-RRM

ATP-binding to FUS-RRM domain was tested using the two-dimensional SOFAST ^{15}N-^{1}H heteronuclear multiple quantum coherence (SOFAST-HMQC) spectra titrated with different ATP concentrations at pH 6.4 (Figure 4.1A). Upon titration with ATP, several residues show chemical shift perturbations (CSPs). The CSPs for the backbone amides have been shown in (Figure 4.1C). The significant CSP plus one standard deviation (SD) have been mapped onto the PDB structure (Figure 4.1D). These residues span from N-to C-terminal regions of the protein. In order to determine the binding affinity, the non-overlapping residues showing significant CSPs were fit globally to a two-state binding process using TITAN (Figure 4.1B) (12). The fitted binding constant (K_d) of 6.4 ± 0.1 mM was found to be consistent with ATP-binding for RRM reported previously (16).

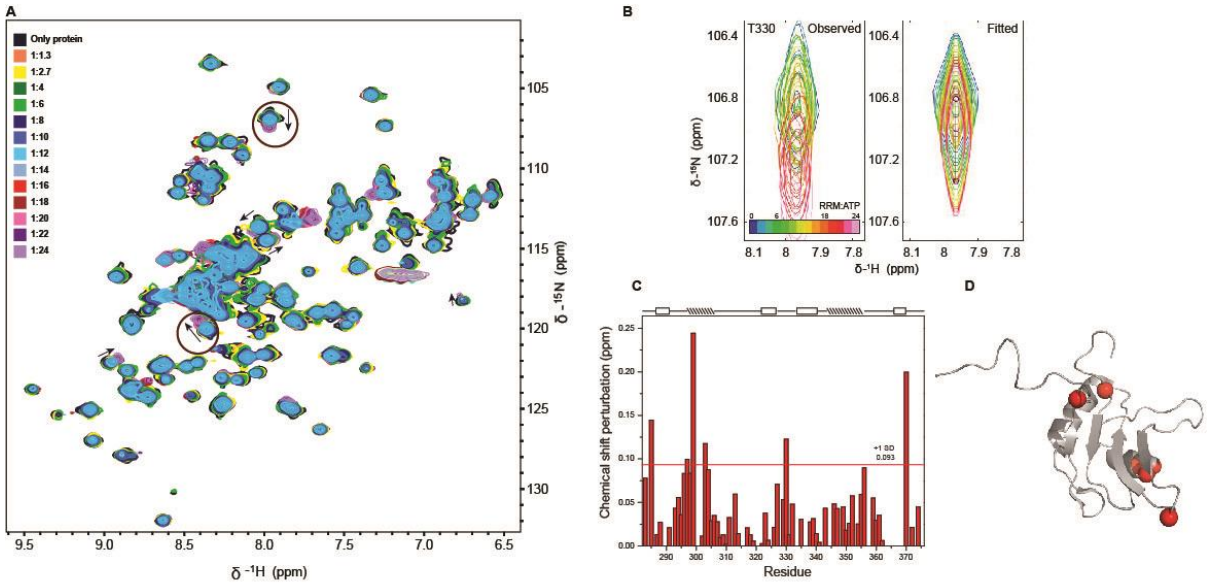

Figure 4.1. ATP titration study for the FUS-RRM protein at pH 6.4. (A) An overlay plot of ^{15}N-^{1}H HSQC of FUS-RRM titrated with different molar ratios of ATP at pH 6.4. (B) Observed and fitted ^{15}N-^{1}H HMQC spectra of FUS-RRM upon titration with ATP. (C) CSP plot of residues titrated with the highest molar ratio of ATP used (1:24). (D) The residues that show significantly different CSPs (above plus one standard deviation), mapped onto the FUS-RRM PDB structure.

Similarly, a binding constant of 4.7 ± 0.1 mM for ATP-binding to FUS-RRM was observed at pH 4.6 (Figure 4.2). The titration data show that mainly the loop residues are perturbed by the addition of ATP, thereby suggesting that loop movements correlate with the ATP binding. These observations have also been reported earlier using molecular dynamics (MD) simulation for RNA-binding to FUS-RRM (17).

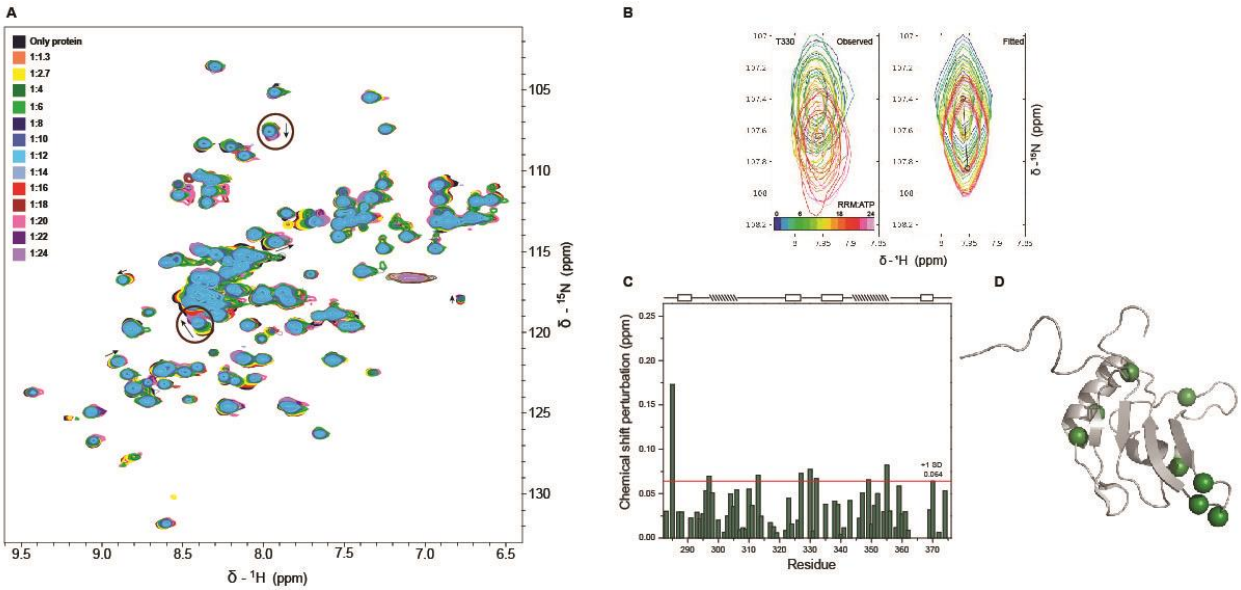

Figure 4.2. ATP titration study for the FUS-RRM protein at pH 4.6. (A) An overlay plot of ^{15}N-^{1}H HSQC of FUS-RRM titrated with different molar ratios of ATP at pH 4.6. (B) Observed and fitted ^{15}N-^{1}H HMQC spectra of FUS-RRM upon titration with ATP. (C) CSP plot of residues titrated with the highest molar ratio of ATP used (1:24). (D) The residues that show significantly different CSPs (above plus one standard deviation), mapped onto the FUS-RRM PDB structure.

4.3.2 ATP modulates the ES^{HARD} of FUS-RRM

In order to understand how ATP could affect the fast µs-ms dynamics of FUS-RRM at both pH values, we used a similar adiabatic $R_{1\rho}$ and $R_{2\rho}$ relaxation dispersion experiment. A 10-fold excess of ATP was used to study the dynamics of the ATP-bound state, as higher ATP ratios of 1:100 or 1:200 led to a significant increase in the aggregation kinetics at pH 6.4 (Figure 4.3).

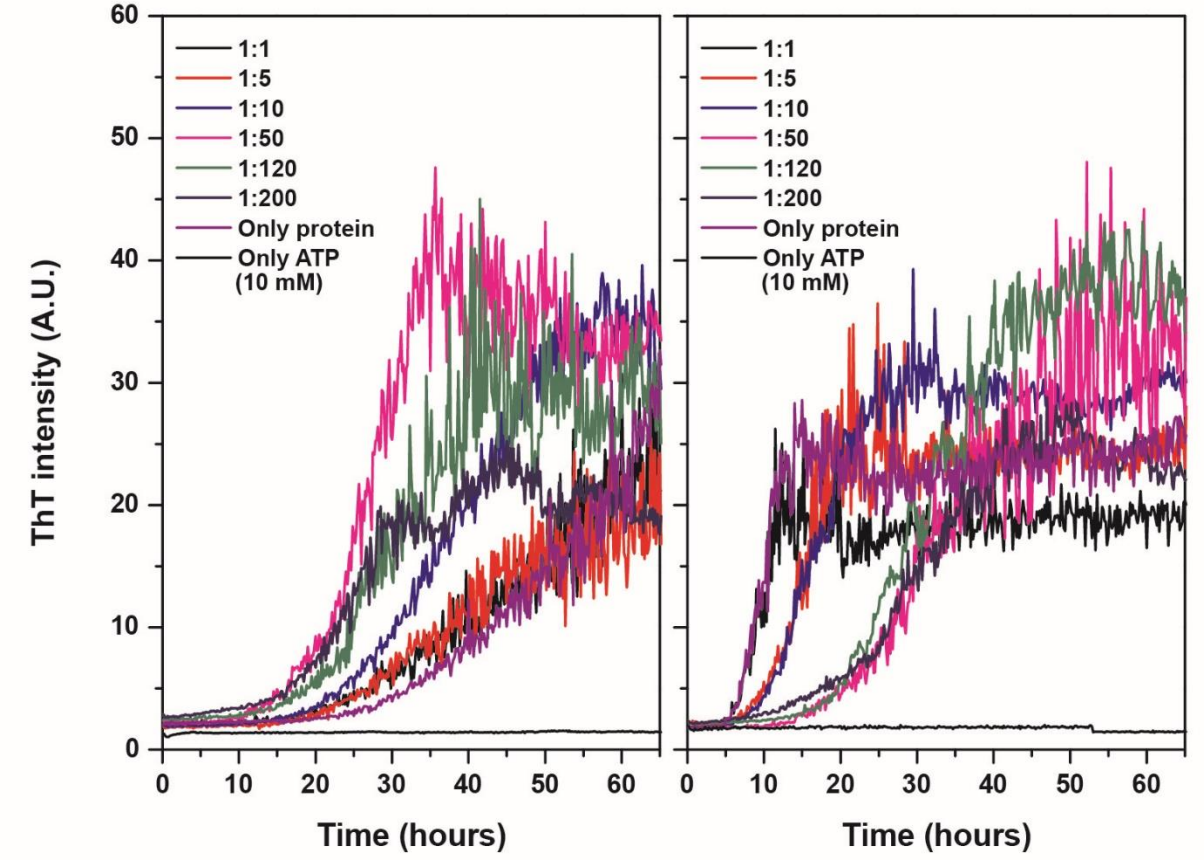

Figure 4.3. ATP-dependent aggregation kinetics of FUS-RRM measured at (A) pH 6.4 and (B) pH 4.6. Data are shown as Mean ± SD from two independent experiments. Error bars are omitted for visual clarity.

At pH 6.4, ATP significantly quenches the fast µs-ms dynamics as reflected by both the average k_{ex} values and the p_{ES} (Figures 4.4A and 4.4B). The average k_{ex} reduces to 3.7 kHz from 40.9 kHz as measured earlier in the absence of ATP. The average ground state population increases to 97.3% (in the presence of ATP) from 93.8% in the absence of ATP.

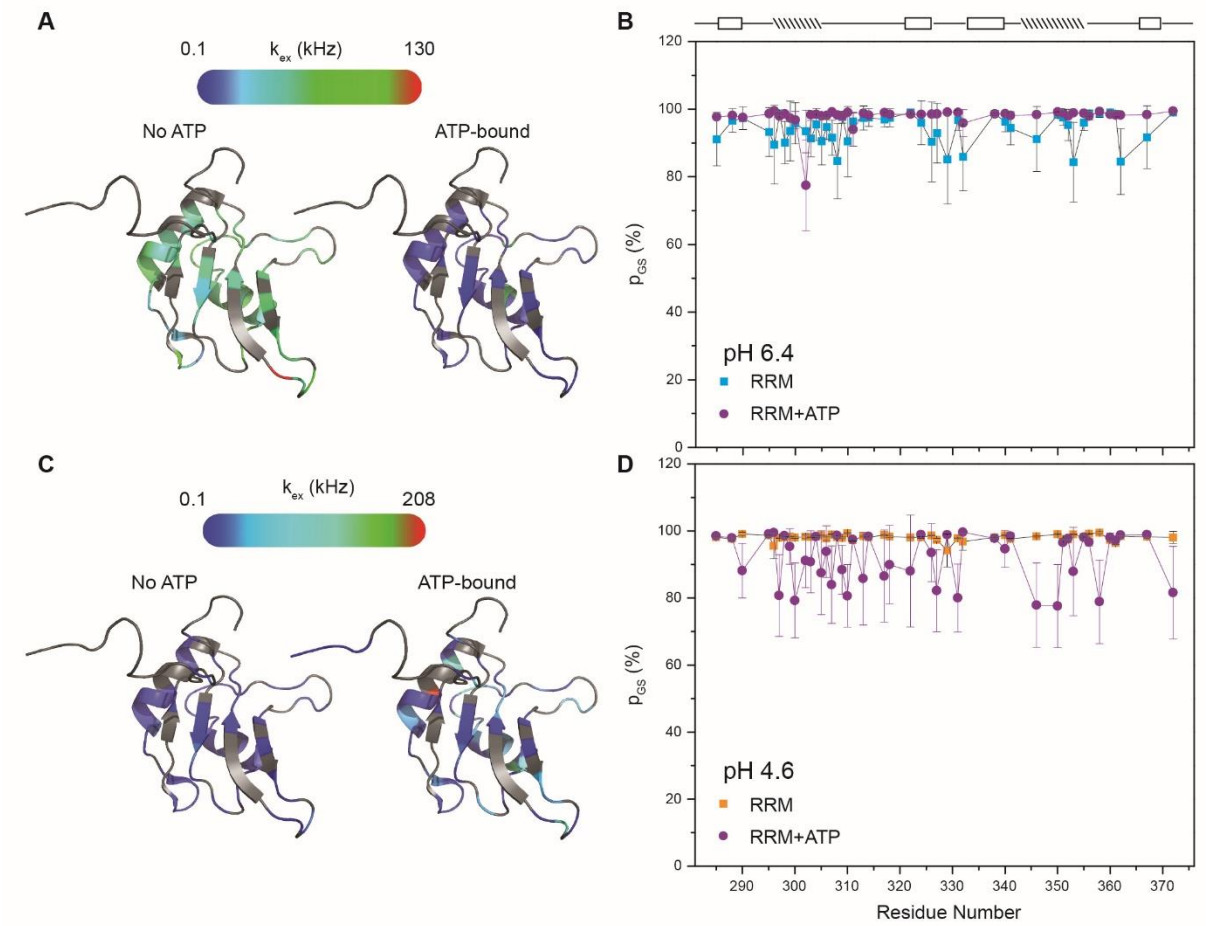

Figure 4.4. ATP-induced perturbation on fast µs-ms dynamics of FUS-RRM domain measured at pH 6.4 and pH 4.6. (A) kex rates mapped to the FUS-RRM tertiary structure and the population of the ground state in (B) at pH 6.4. (C) kex rates mapped to the FUS-RRM tertiary structure and the population of the ground state in (D) at pH 4.6. The residues highlighted in grey do not fit any model and, hence, are not included in the discussion. The secondary structure of FUS-RRM is indicated on the top of panel B, with boxed and dashed rectangles denoting strands and helices, respectively.

For pH 4.6, ATP addition led to an increase in both k_{ex} and the excited state population (p_{ES}). The average k_{ex} increases from 0.2 kHz to 24 kHz in the presence of ATP (Figure 4.4C). And the population of the ground state reduced significantly (average p_{GS} = 91%) (Figure 4.4D). This indicates that ATP binding significantly increases the fast µs-ms conformational dynamics at pH 4.6.

4.3.3 ATP modulates the ES^{CEST} of FUS-RRM

Similarly, we performed ^{15}N-CEST experiment in the presence of 10-fold of ATP. We find a similar set of residues (13 residues) showing the presence of a characteristic minor dip in the ^{15}N-CEST profiles at pH 6.4 (Figure 4.5).

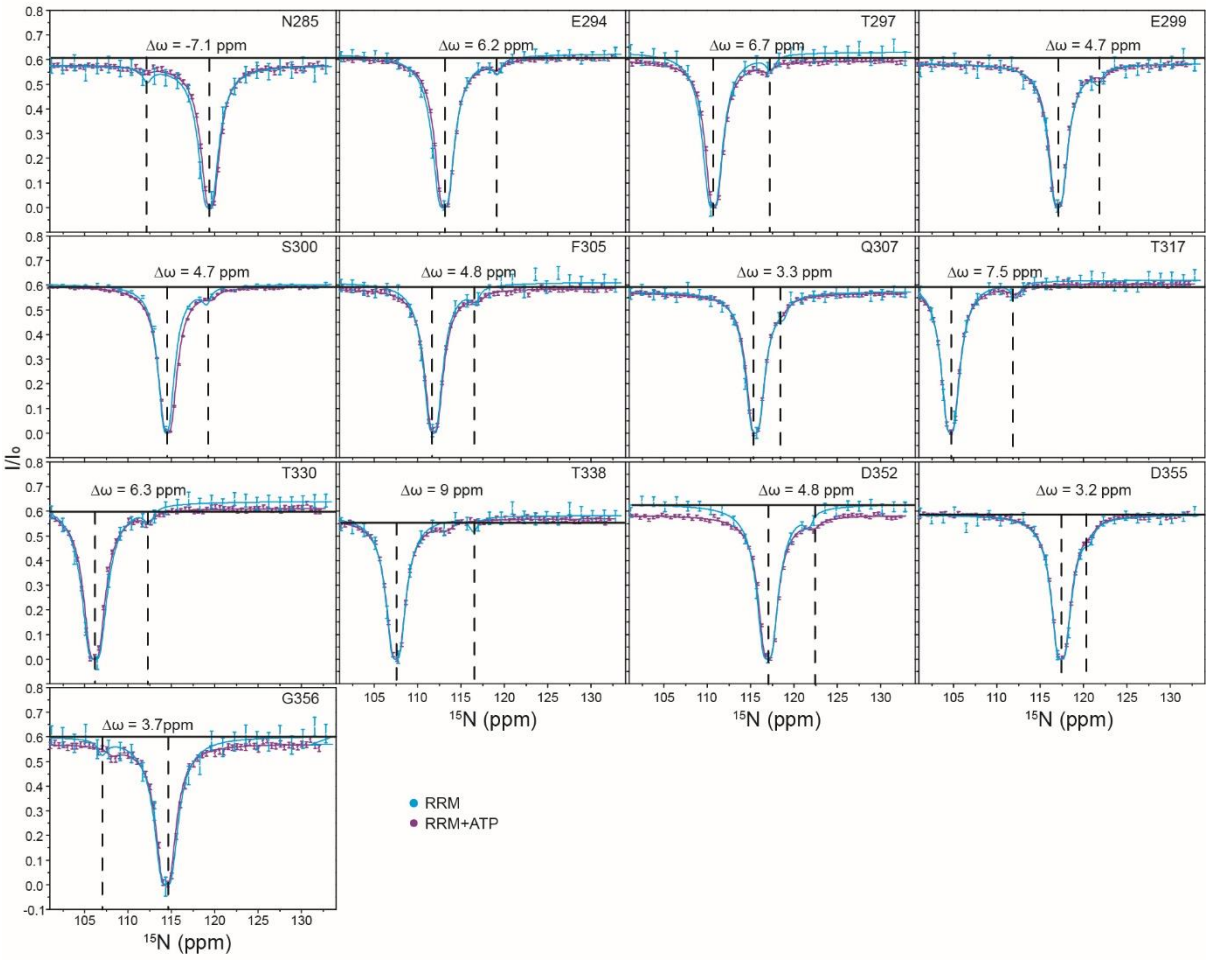

Figure 4.5. An overlay of ^{15}N CEST profiles with and without ATP at pH 6.4 and with corrected offsets for each ground state. The obtained χ^2_{red} is of 1.2 using a fit to a two-state model. The vertical dashed lines have been used to depict the large chemical shift changes between the ground and excited state.

For pH 4.6, we find a similar set of residues (9 residues) showing the presence of a characteristic minor dip in the ^{15}N-CEST profiles at pH 4.6 (Figure 4.6).

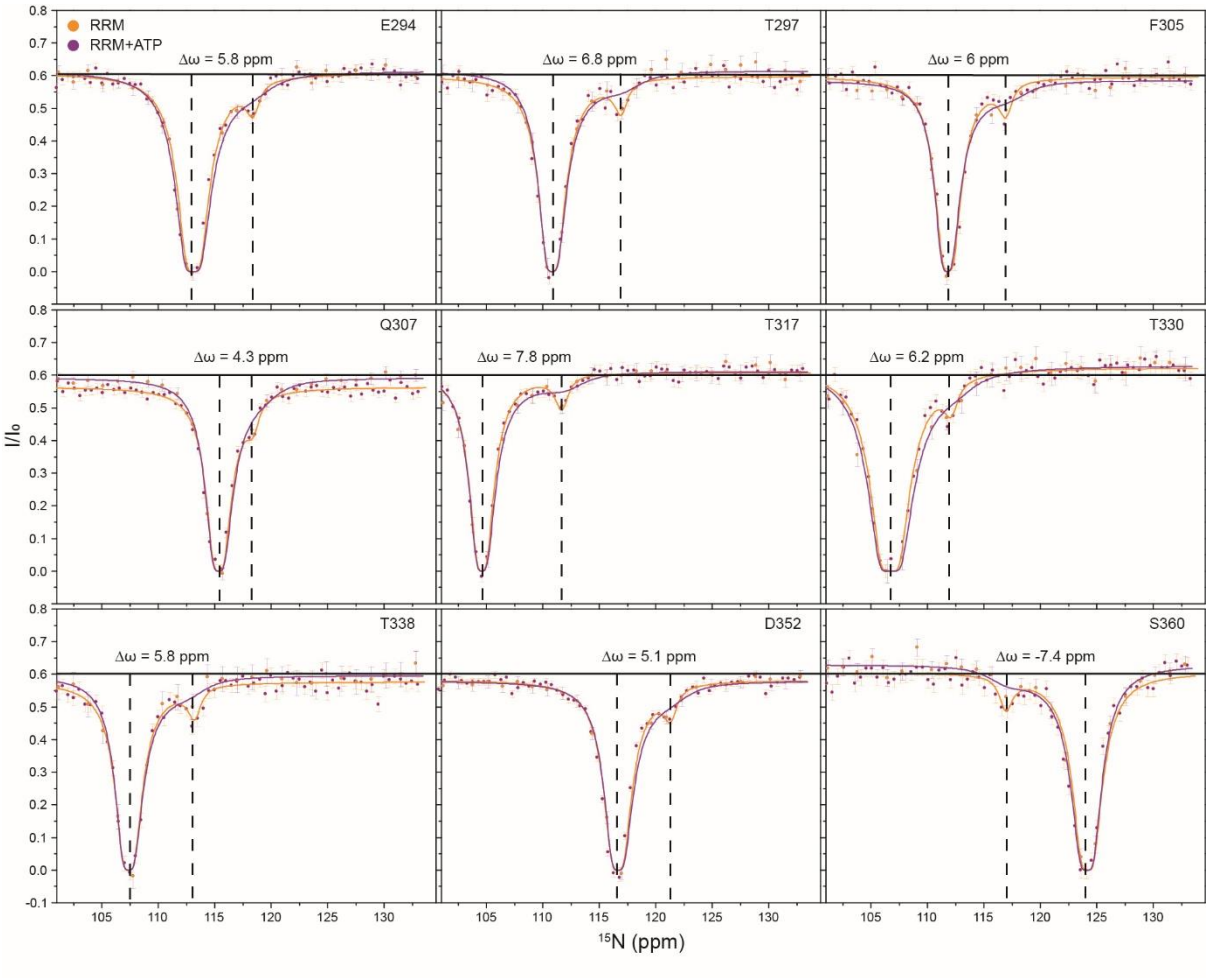

Figure 4.6. An overlay of ^{15}N CEST profiles with and without ATP at pH 4.6 and with corrected offsets for each ground state. The obtained χ^2_{red} is of 0.6 using a fit to a two-state model. The vertical dashed lines have been used to depict the large chemical shift changes between the ground and excited state.

When fit in ChemEx, we obtain a reduction in the observed k_{ex} to 58.9 s^{-1} and an increase in p_{ES} to 0.49%, thereby indicating an increase in ES^{CEST} population (Figures 4.7A and 4.7B) in comparison to the data measured in the absence of ATP (k_{ex} is 257 s^{-1} and p_{ES} is 0.14%). Interestingly, at pH 4.6, when fit to a two-state model in ChemEx, ATP does not perturb the ES^{CEST} population (p_{ES} is 0.48%) when compared with that in the absence of ATP (p_{ES} is 0.5%), it increases k_{ex} from 142 to 895 s^{-1} (Figures 4.7C and 4.7D).

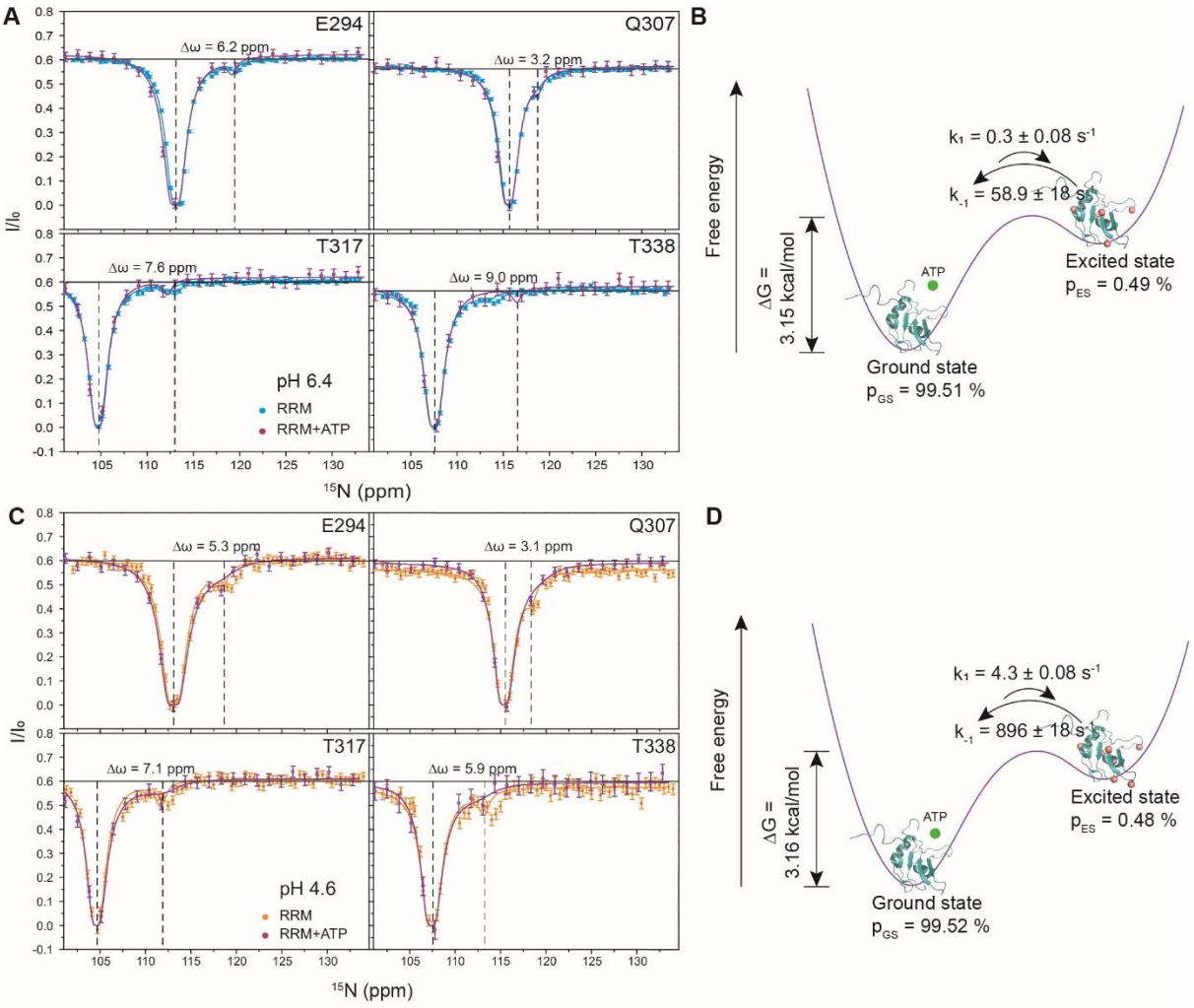

Figure 4.7. Slow µs-ms dynamics of FUS-RRM protein in the presence of ATP. (A) An overlay of the ^{15}N CEST profiles of representative FUS-RRM residues at pH 6.4 with (purple) and without ATP (cyan) and with corrected offsets for each ground state. (B) The energy landscape of FUS-RRM with ATP, showing the two states and their interconversion rates with fractional populations at pH 6.4. (C) The ^{15}N CEST profiles of representative FUS-RRM residues at pH 4.6 with (purple) and without ATP (orange), and with corrected offsets for each ground state. (D) The energy landscape of the FUS-RRM domain with ATP, showing the two states and their interconversion rates with fractional populations at pH 4.6. The green circle is shown as ATP. The vertical dashed lines have been used to depict the large chemical shift changes between the ground and excited state.

4.3.4 Aggregation kinetics

In chapter 3, we had observed that the rate of FUS-RRM aggregation increases significantly upon decreasing the pH from 6.4 to 4.6. The dynamics data shows a change in the ES populations and link to its aggregation. Therefore, to validate this further, we performed an ATP-dependent aggregation kinetics experiment on the FUS-RRM domain. At pH 6.4, the addition of ATP to FUS-RRM leads to an increase in the aggregation kinetics (lag time decreases from 36 hours to 24.2 hours in the presence of ATP) (Figure 4.8A). While at pH 4.6, it leads to a decrease in the rate of aggregation (lag time increases from 6 hours to 10.3 hours in the presence of ATP) (Figure 4.8B). The morphology of the aggregates, as observed by transmission electron microscope (TEM) image at the end of the kinetics experiment, appeared

highly heterogeneous in both shape and size, making quantitative analysis challenging (Figures 4.8C-D). This implies that ATP could modulate the final aggregate state of FUS-RRM, as has also been shown earlier for Aβ protein, where amorphous aggregates have been detected (8). The opposite effect of perturbed kinetics seen at the two pH values correlates well with the opposite perturbation of the observed slow and fast µs-ms dynamics, which suggests a direct role of conformational dynamics in modulating aggregation.

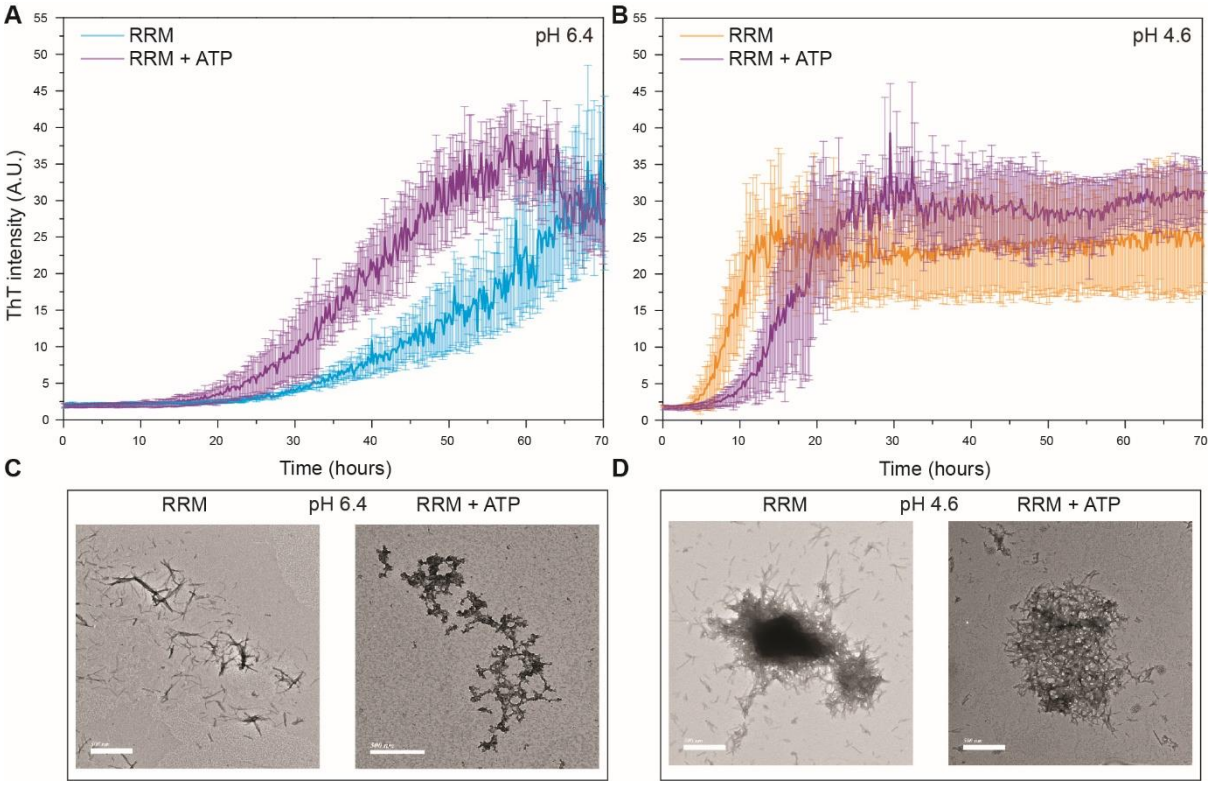

Figure 4.8. Aggregation kinetics for the FUS-RRM domain, as measured by monitoring ThT intensity, while agitation in the presence of ATP (10-fold) at (A) pH 6.4, and (B) pH 4.6. The aggregates of FUS-RRM, thus formed at the end of the measurements, imaged by TEM have been depicted in (C) for samples at pH 6.4, and (D) at 4.6. Data have been represented as Mean ± SD of three independent experiments.

4.4 Proposed model

Figure 4.9 demonstrates the effect of pH and ATP on the conformational landscape of FUS-RRM. As can be observed from the data presented in this Chapter, perturbations induced by pH changes and ATP supplementation have an opposite effect on the dynamics of FUS-RRM. ATP at pH 6.4 stabilises the ES^{CEST} state of FUS-RRM, while at pH 4.6, ATP addition stabilises the ES^{HARD} state of the protein. And upon stabilising ES^{HARD} state, it leads to delay aggregation. This highlights the importance of fast µs-ms dynamics to suppress FUS-RRM aggregation.

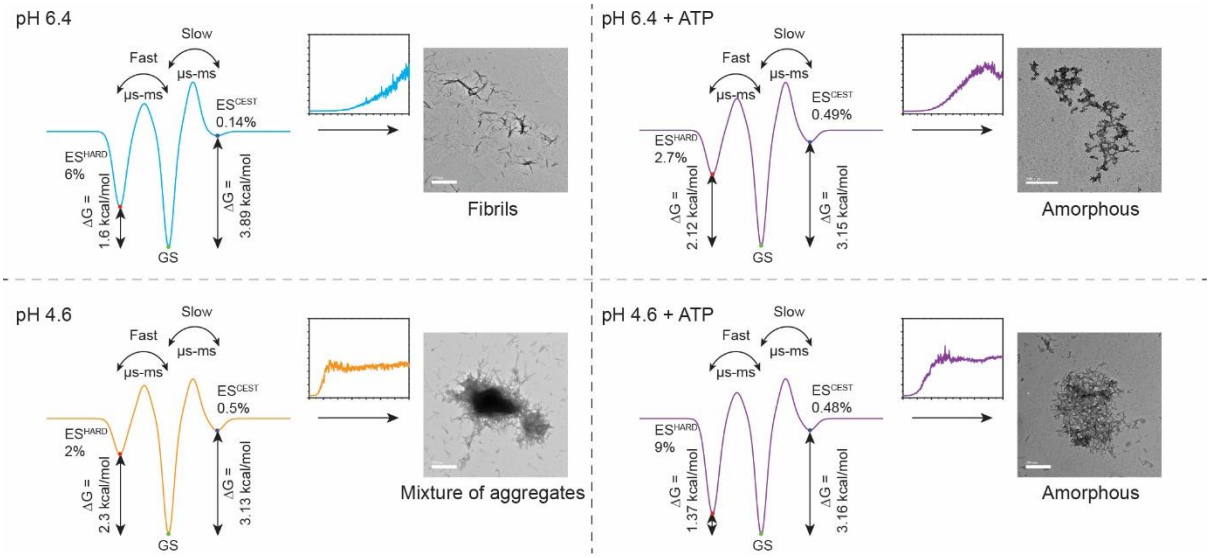

Figure 4.9. A cartoon representation of the free energy landscape of FUS-RRM showing conformational heterogeneity (a ground state, GS, and two excited states, ES^{HARD} and ES^{CEST}, measured by HARD-$R_{1\rho/2\rho}$ and ^{15}N-CEST, respectively) and the associated aggregate formation monitored by TEM. On the arrow heads, corresponding kinetics data as measured by ThT fluorescence has been included to highlight a perturbation in kinetics of aggregation. The free energy difference and experimentally determined population of each excited state has also been mentioned.

4.5 Discussion

From the titration experiment, we find that ATP binds weakly (K_d = 6.4/4.7 mM) to FUS-RRM but induces significant perturbations in both the slow and fast µs-ms dynamics. At pH 6.4, ATP stabilizes ES^{CEST}, while destabilizing ES^{HARD}, and increases the rate of formation of aggregates, but results in the formation of amorphous aggregates. At pH 4.6, however, ES^{CEST} remains more or less unperturbed in terms of population, but k_{ex} increases significantly from 142 to 900 s^{-1}. This is also highlighted by stabilization of ES^{HARD} from 2% to 9%, and subsequent decrease in the rate of formation of aggregates. The contrasting effects of ATP on slow and fast µs-ms dynamics at pH 6.4 and 4.6, along with the corresponding changes in aggregation behavior, suggest a complex relationship between ATP, pH, and protein aggregation kinetics (Figure 4.9). This suggests that while the population of ES^{CEST} is directly correlated with the rate of formation of aggregates, there is an inverse correlation between the population of ES^{HARD} and the rate of formation of aggregates. Although both dynamics seem to play an important role in aggregation, we do not know exactly which one precludes the other. But an increase in fast dynamics could be used as a model to delay aggregation, as has been suggested earlier also for FUS (18) or Aβ (8).

The results of pH-dependent aggregation kinetics suggest that there might be a certain optimum concentration of cellular ATP levels relative to the protein concentration that can

inhibit or delay the formation of amyloid aggregates. As cells undergo stress, higher ATP levels could stabilize the distinct conformation and thus prevent aggregation. An increased concentration of ATP might thus be a safeguard against aggregation-prone proteins during stress conditions or upon aging. This is also important when a mutation disrupts nucleic acid-binding ability, but higher ATP in such instances could be used to delay aggregation.

4.6 References

1. Greiner JV, Glonek T. Intracellular ATP Concentration and Implication for Cellular Evolution. Biology. 2021;10(11).
2. Moreira PI, Carvalho C, Zhu X, Smith MA, Perry G. Mitochondrial dysfunction is a trigger of Alzheimer's disease pathophysiology. Biochim Biophys Acta. 2010;1802(1):2-10.
3. Zamaraeva MV, Sabirov RZ, Maeno E, Ando-Akatsuka Y, Bessonova SV, Okada Y. Cells die with increased cytosolic ATP during apoptosis: a bioluminescence study with intracellular luciferase. Cell death and differentiation. 2005;12(11):1390-7.
4. Alvarez A, Cacabelos R, Sanpedro C, García-Fantini M, Aleixandre M. Serum TNF-alpha levels are increased and correlate negatively with free IGF-I in Alzheimer disease. Neurobiology of aging. 2007;28(4):533-6.
5. Swardfager W, Lanctôt K, Rothenburg L, Wong A, Cappell J, Herrmann N. A meta-analysis of cytokines in Alzheimer's disease. Biological psychiatry. 2010;68(10):930-41.
6. Exley C. ATP-promoted amyloidosis of an amyloid beta peptide. Neuroreport. 1997;8(15):3411-4.
7. Heo CE, Han JY, Lim S, Lee J, Im D, Lee MJ, et al. ATP Kinetically Modulates Pathogenic Tau Fibrillations. ACS chemical neuroscience. 2020;11(19):3144-52.
8. Kuramochi M, Nakamura M, Takahashi H, Komoriya T, Takita T, Pham NTK, et al. Adenosine triphosphate induces amorphous aggregation of amyloid β by increasing Aβ dynamics. Scientific reports. 2024;14(1):8134.
9. Mahapatra S, Sarbahi A, Punia N, Joshi A, Avni A, Walimbe A, et al. ATP modulates self-perpetuating conformational conversion generating structurally distinct yeast prion amyloids that limit autocatalytic amplification. The Journal of biological chemistry. 2023;299(5):104654.
10. Patel A, Malinovska L, Saha S, Wang J, Alberti S, Krishnan Y, et al. ATP as a biological hydrotrope. Science (New York, NY). 2017;356(6339):753-6.
11. Schanda P, Kupce E, Brutscher B. SOFAST-HMQC experiments for recording two-dimensional heteronuclear correlation spectra of proteins within a few seconds. J Biomol NMR. 2005;33(4):199-211.
12. Waudby CA, Ramos A, Cabrita LD, Christodoulou J. Two-Dimensional NMR Lineshape Analysis. Scientific reports. 2016;6:24826.
13. Delaglio F, Grzesiek S, Vuister GW, Zhu G, Pfeifer J, Bax A. NMRPipe: a multidimensional spectral processing system based on UNIX pipes. J Biomol NMR. 1995;6(3):277-93.
14. Bolik-Coulon N, Hansen DF, Kay LE. Optimizing frequency sampling in CEST experiments. J Biomol NMR. 2022;76(5-6):167-83.
15. Guenneugues M, Berthault P, Desvaux H. A method for determining B1 field inhomogeneity. Are the biases assumed in heteronuclear relaxation experiments usually underestimated? J Magn Reson. 1999;136(1):118-26.

16. Kang J, Lim L, Song J. ATP binds and inhibits the neurodegeneration-associated fibrillization of the FUS RRM domain. Communications biology. 2019;2:223.
17. Basu S, Alagar S, Bahadur RP. Unusual RNA binding of FUS RRM studied by molecular dynamics simulation and enhanced sampling method. Biophys J. 2021;120(9):1765-76.
18. Patel A, Lee HO, Jawerth L, Maharana S, Jahnel M, Hein MY, et al. A Liquid-to-Solid Phase Transition of the ALS Protein FUS Accelerated by Disease Mutation. Cell. 2015;162(5):1066-77.

Chapter 5: Conclusions and Future Directions

5.1 Conclusions

The results from this study provide important insights into the conformational dynamics of FUS-RRM, a key domain involved in RNA binding and cellular regulation. By combining information obtained from CEST, adiabatic $R_{1\rho}$ and $R_{2\rho}$ relaxation dispersion, this study uncovers the existence of multiple excited states in FUS-RRM. The results obtained from these investigations have helped expand our understanding of the intrinsic dynamic nature of the FUS-RRM and its possible functional implications in cellular processes, such as RNA binding and protein-RNA interactions.

The ps-ns timescale dynamics of FUS-RRM, suggest that FUS-RRM exists in a highly flexible conformational space, possibly allowing it to rapidly sample a large conformational space (1). We identified that the FUS-RRM populates not only GS and ES^{HARD} but also ES^{CEST} at slow µs-ms timescale. We showed using urea-perturbed ^{15}N-CEST measurements, ES^{CEST} represents a partially unfolded or locally disordered ensemble. A dynamic exchange was observed between these conformational substates in various environmental perturbations, including pH change and ATP supplementation, as described in this thesis. Further, a correlation between the populations of excited states (ES^{HARD} and ES^{CEST}) and their exchange rates with GS was observed to exist with the aggregation kinetics and aggregated states (fibrils and amorphous). At pH 6.4, ES^{HARD} is more populated when compared to $ES^{CEST,}$ resulting in a fibril state. While at pH 4.6, increased stability of ES^{CEST} state and destabilization of ES^{HARD} were observed, and a concurrent enhanced rate of aggregation was noted. ATP leads to stabilisation of the ES^{CEST} state at pH 6.4, leading to an increase in aggregation. In contrast, ATP stabilises the ES^{HARD} state at pH 4.6, which is associated with reduced aggregation. These observations support the idea that increased fast dynamics (more populated ES^{HARD}) suppress aggregation, while increased slow dynamics (more populated ES^{CEST}) promote it. Collectively, our results suggest that an artificial stabilization of ES^{HARD} may protect FUS-RRM against aggregation. The study also points to a broader mechanistic role of H^+ ions and ATP in modulating the aggregation of this RNA-binding protein. Interestingly, our pH-dependent aggregation kinetics suggest the existence of an optimal ATP-to-protein ratio that may prevent or delay amyloid formation.

From a physiological perspective, our findings may also help explain why neuronal cells maintain relatively low ATP concentrations compared to other cell types despite being very energy-intensive (2). We believe that while moderate ATP levels can stabilize functional conformers and suppress aggregation, excessive ATP may shift the energy landscape toward

alternate substates, facilitating aggregation under certain conditions. Under cellular stress or aging, where ATP levels fluctuate, its ability to act as a conformational buffer gets impaired, potentially increasing the risk of aggregation, and elevated ATP levels in such instances can stabilize aggregation-prone conformers. This points to ATP as a modulator of protein solubility and aggregation—consistent with emerging literature suggesting ATP has chaperone-like roles in cellular protein homeostasis. Moreover, in the context of disease mutations that disrupt nucleic acid binding, ATP may play a compensatory role by stabilizing a distinct, less aggregation-prone conformation(s), which requires further investigation. Overall, from pH and ATP perturbations, we find that the environmental factors can re-wire the energy landscape, shifting populations, and may lead to different functional outcomes, e.g., altering aggregation propensity, as is observed in this study. These results further emphasize the necessity of integrating diverse experimental approaches to comprehensively understand protein dynamics and their implications for function so that an increased conformational space (encompassing all the excited states and not limited to the native structure of a target protein) can be sampled for drug discoveries.

5.2 Future Directions

This study provides key insights into the role of conformational dynamics in FUS-RRM aggregation. Moving forward, several important avenues remain to be explored.

While ^{15}N CEST is widely used to probe excited states in proteins, but due to its low chemical shift dispersion, it has limited structural resolution. In order to derive information about the excited state structural properties, carbon-based CEST experiments are best suited to get residue-specific structural information for the lowly populated excited states (3). ^{13}C CEST, especially using ^{13}Cα, ^{13}Cβ, and ^{13}CO nuclei, provides higher chemical shift dispersion, side-chain, and secondary structure propensity.

Furthermore, molecular dynamics simulations could also be a strong pillar to complement experimental data by providing information about transient intermediates and help supplement the CEST data.

In addition to characterise the fibril morphologies, it would also benefit from cell-based assays to evaluate the cytotoxicity of fibrillar aggregates. This would link the aggregation pathways to pathological relevance, such as in neurodegenerative diseases.

Together, these approaches will give a more comprehensive picture of the role of conformational heterogeneity in FUS-RRM function, and provide some therapeutic targeting of aggregation-prone intermediates.

5.3 References

1. Lu Y, Lim L, Song J. RRM domain of ALS/FTD-causing FUS characteristic of irreversible unfolding spontaneously self-assembles into amyloid fibrils. Scientific reports. 2017;7(1):1043.

2. Greiner JV, Glonek T. Intracellular ATP Concentration and Implication for Cellular Evolution. Biology. 2021;10(11).

3. Madhurima K, Nandi B, Munshi S, Naganathan AN, Sekhar A. Functional regulation of an intrinsically disordered protein via a conformationally excited state. Science Advances.9(26):eadh4591.

Appendix 1: Protein over-expression and purification

Preparation of Stock Solutions

LB media

- Make 1 x 1liter ml solutions (25 g/L). Autoclave media and let it cool.
- Make 1 x 10 ml solutions (0.5 g/20 mL). Autoclave media and let it cool.

Preparation of stock solutions for protein purification

- 1 M Tris-base:

Dissolve 30.3 g of Tris-base in 200 ml autoclaved water. Adjust pH to 8 and make up the volume to 250 ml with MilliQ. Autoclave and store at room temperature.

- 3 M Imidazole:

Dissolve 20.424 g of imidazole in 90 ml autoclaved water and make up the volume to 100 ml with autoclaved water. Autoclave and store at room temperature.

- 5 M NaCl:

Dissolve 292.2 g of NaCl in 900 ml of autoclaved water and make up the volume to 1 liter with autoclaved water. Autoclave and store at room temperature.

- Kanamycin Stock solution (50 mg/ml)

Weigh 500 mg of Kanamycin di-sulfate. Dissolve in 10 ml autoclaved water. Filter sterilize in the hood. Make aliquots of 1 ml each and store at -20°C.

- 100 mg/ml Lysozyme:

Dissolve 100 mg of lysozyme in 1 ml of distilled water. Make aliquots of 0.5 ml in micro-centrifuge tubes. Store at -20°C until use.

- 1 M IPTG

Dissolve 119 mg of IPTG in 0.5 ml of distilled water and use it.

- Protease Inhibitor Cocktail (10X) solution

Dissolve 1 tablet of EDTA free protease inhibitor cocktail in 10 ml of distilled water. Filter sterilize through a syringe-filter. Make aliquots of 1 ml each in micro-centrifuge tubes. Store at -20°C until use.

- 100 mM PMSF

Dissolve 0.174 g of PMSF in 10 ml of 2-propanol, anhydrous. Keep on rotospin to dissolve for about 15-30 min. Store at 4°C until use.

- 0.1 M Sodium Phosphate dibasic (Na_2HPO_4)

Dissolve 7.35 g of sodium phosphate dibasic in about 80 ml of water and make up the volume to 100 ml with water. Filter and store until use.

- 0.1 M Sodium Phosphate monobasic (NaH_2PO_4)

Dissolve 2.65 g of sodium phosphate monobasic in about 80 ml of water and make up the volume to 100 ml with water. Filter and store until use.

- 1 M Sodium acetate

Dissolve 8.2 g of sodium acetate in about 80 ml of filtered MilliQ and make up the volume to 100 ml with water. Filter and store until use.

- 1 M glacial acetic acid

Use glacial acetic acid to make 1M of required solution. Make up the volume to 100 ml with MilliQ. Filter and store until use.

Protocol for Over-expression and Purification of FUS-RRM

Preparation of buffers for protein purification

(All volumes for buffer preparations to be taken from the stock solutions)

Equilibration Buffer or Gel Filtration Buffer, pH 8, 700 ml

20 mM Tris base	14 ml
150 mM NaCl	21 ml

Lysis Buffer, pH 8 100 ml

Use 100 ml of equilibration buffer and add 167 µl of 300 mM imidazole.

Elution Buffer, pH 8	**100 ml**
20 mM Tris base	2 ml
150 mM NaCl	3 ml
300 mM Imidazole	10 ml

1. Add stock liquids (Tris base, imidazole, NaCl)
2. Add filtered MilliQ to 80-90% of the final volume.
3. Titrate pH to 8.
4. Makeup the volume with filtered MilliQ water.
5. Filter sterilize into a sterile bottle.
6. Store all at 4°C.

NMR Buffer, pH 6.4 100 ml

10 mM sodium phosphate (7.35 ml of 0.1M NaH_2PO_4 + 2.65 ml of 0.1M Na_2HPO_4)

100 mM NaCl 2 ml

NMR Buffer, pH 4.6 100 ml

10 mM sodium acetate (0.505 ml of 1M acetic acid + 0.495 ml of 1M sodium acetate)

100 mM NaCl 2 ml

Overexpression of FUS-RRM protein in a bacterial expression system

1. Prepare LB media
2. Add kanamycin to the sterile LB media (20 ml) to a final concentration of 50 μg/ml.
3. Use a pipette-tip to pick BL21(DE3) cells containing appropriate plasmid from transformed agar plate and transfer it to 20 ml LB medium containing antibiotic.
4. Allow cells to grow overnight at 37°C in incubator shaker with shaker speed set to 180 rpm.
5. Add 20 ml overnight culture to 1 liter of LB media containing Kanamycin (final conc. 50 μg/ml) and continue incubation with shaking.
6. Monitor the OD600 after 2hrs till it reaches ~1.0.
7. Add IPTG (1 M stock) to a final concentration of 0.5 mM and continue induction for 8 hr at 28°C with shaking.
8. Centrifuge solution for 30 min at 4500 rpm, 4°C in a high-speed centrifuge. Decant the supernatant.
9. Store the pellet at -20 °C until use. [Usually, 1 liter culture→ 3-4 g (pellet weight)].

Cell Lysis and Purification of FUS-RRM protein

1. Resuspend the cell pellet in 20-30 ml of Lysis buffer pH 8. Keep the cell pellet on the ice during lysis.
2. Add 100 µl of PMSF.
3. Add 2 ml of PIC solution.
4. Add 500 µl of Triton-X 100 in ~5 ml of lysis buffer. Warm to dissolve and cool on ice and then use.
5. Add 100 µl of Lysozyme solution to the above solution.
6. Incubate for 20 min on ice. (till you get viscous solution i.e. DNA is released in the solution).
7. Sonicate using a probe sonicator.

(Sonication cycle: time 3 min, pulse on 5s, pulse off 5s, and amplitude 60%).

8. Add cell lysate to 50 ml oak ridge tubes and centrifuge at 14000xg for 30 min at 4°C in the high-speed centrifuge.
9. Transfer the supernatant to a fresh 50 ml corning tube. (Total soluble protein TSP-I).

Purification of tagged protein by Ni-NTA Affinity Chromatography

1. Prepare HisTrap column for protein binding.
    a. Pass 5-6 Column Volume (CV) of autoclaved water through the Ni-NTA column (HisTrap 5 ml column, GE Healthcare).
    b. Equilibrate the column using 5-10 CV of Lysis buffer.
2. Circulate TSP-I through the Ni-NTA column for about 2 hr at 4°C to allow binding of the protein to the column.
3. Pass 5 CV of GFC buffer (pH = 8) through the column to remove any non-specific protein binding.
4. Elute the bound protein by passing the elution buffer (pH = 8).
    a. Fill the column with elution buffer. Allow to equilibrate for 30 min.
    b. Elute by passing fresh 1 CV elution buffer. Collect the eluted fraction in a 15 ml fresh falcon.
    c. Repeat step b and collect the elutions in different falcons (upto 6).
    d. Check protein by running SDS-PAGE.
5. Pool all the eluted fractions containing protein and concentrate to 5 ml using a 3 kDa amicon filter. Take a sample of concentrated protein (label it before GFC).

Note: One can also use AKTA system for collecting proteins. Use flow rate of 1 ml/min for washing with GFC buffer using any pump. Then for elution use second pump with 0.5 ml/min. Monitor the A280 and collect in a falcon. Then concentrate it using a 3 kDa amicon filter till 5 ml.

Gel Filtration Purification of the Protein

Chromatographic conditions

a. Column: Sephacryl 16/60 100 HR (120ml, GE healthcare)
b. Flow rate: 0.5 ml/min
c. Delta column pressure limit: less than 0.15 Mbar
d. Pre-column pressure limit: less than 0.5 Mbar

For equilibrated column with GFC buffer. Use the method run as follows:

1. Equilibration: Equilibrate till 0.1 CV.
2. Method:
3. Sample injection: After 0.1 CV sample is injected into column.
4. Elution: Protein is eluted into 2 ml of 96-well plate.

NMR sample preparation

1. Buffer exchange the concentrated protein to NMR buffer pH 6.4. Store at 4°C until further use.
2. Use 10% of D_2O for the final 500 µl of protein sample. Transfer the sample to the washed NMR tube. Label the tube and close it using parafilm.

Appendix 2: Supporting tables

Table S1: Lag time (in hours) obtained from fitting the aggregation kinetics data measured at pH 6.4 and 4.6.

	pH 6.4			**pH 4.6**		
	25 μM	50 μM	100 μM	25 μM	50 μM	100 μM
Lag time (hours)	54.12	40.03	34.44	8.47	9.37	9.94

Table S2: Secondary structure estimation from CD spectrum (pH 6.4 and pH 4.6) and the solution structure (pH 7.0).

		β-strand (%)	α-helix (%)	Loop (%)
Calculated from PDB ID 2LCW	pH 7.0	20.4	20.4	59.2
Predicted using BeStSel from CD spectrum	pH 6.4	19.7	14.7	65.6
	pH 4.6	21.9	11.8	66.3

Table S3: R_1 relaxation rates measured from HARD experiment for FUS-RRM (pH 6.4) at 600 MHz NMR spectrometer. Only data for which good fits were obtained have been shown.

Residue number	R_1 (s^{-1})		Residue number	R_1 (s^{-1})		Residue number	R_1 (s^{-1})	
	Value	Error		Value	Error		Value	Error
D283	1.59	0.05	I310	1.25	0.02	S346	1.37	0.01
N285	1.37	0.03	I311	1.34	0.03	A347	1.35	0.03
F288	1.32	0.03	T313	1.22	0.02	A349	1.41	0.01
V289	1.42	0.07	N314	1.27	0.01	A350	1.42	0.03
Q290	1.3	0.01	T317	1.33	0.02	I351	1.29	0.03
G291	1.28	0.02	G318	1.36	0.01	D352	1.29	0.01
G293	1.31	0.01	Q319	1.34	0.01	W353	1.28	0.01
E294	1.22	0.01	M321	1.09	0.07	F354	1.27	0.01
N295	1.4	0.02	I322	1.28	0.01	D355	1.29	0.02
V296	1.17	0.02	L324	1.3	0.03	G356	1.36	0.02
T297	1.31	0.01	T326	1.47	0.09	E358	1.29	0.02
I298	1.33	0.01	D327	1.35	0.01	F359	1.32	0.01
E299	1.32	0.01	E329	1.28	0.02	S360	1.52	0.16
S300	1.29	0.01	T330	1.28	0.02	G361	1.45	0.05
V301	1.2	0.05	G331	1.45	0.02	N362	1.32	0.01
A302	1.37	0.04	K332	1.63	0.03	I364	1.51	0.05
D303	1.24	0.02	G335	1.45	0.03	V366	1.28	0.05
Y304	1.37	0.02	T338	1.29	0.01	S367	1.33	0.01
F305	1.28	0.01	V339	1.35	0.01	A369	1.39	0.03
K306	1.42	0.03	S340	1.28	0.01	T370	1.51	0.08
Q307	1.41	0.01	F341	1.31	0.03	R372	1.82	0.13
I308	1.36	0.02	D343	1.69	0.14	D374	1.76	0.05
G309	1.29	0.01						

Table S4: $R_{1\rho}$ relaxation rates measured using HSn pulses (n=1,2,4,6,8) from HARD experiment for FUS-RRM (pH 6.4) at 600 MHz NMR spectrometer. Only data for which good fits were obtained have been shown.

Residue Number	$R_{1\rho}$ (s^{-1})									
	HS1		HS2		HS4		HS6		HS8	
	Value	Error	Value	Error	Value	Error	Value	Error	Value	Error
D283	4.21	0.28	4.41	0.05	5.03	0.10	5.39	0.28	5.39	0.16
N285	4.22	0.18	5.21	0.19	6.10	0.29	6.47	0.42	6.70	0.39
F288	3.85	0.19	4.74	0.13	5.60	0.17	5.92	0.21	6.00	0.07
V289	4.16	0.21	4.51	0.07	5.39	0.33	6.13	0.20	6.20	0.33
Q290	3.79	0.11	4.86	0.03	5.45	0.03	6.01	0.13	5.76	0.06
G291	4.23	0.23	5.22	0.17	5.79	0.07	6.32	0.26	6.30	0.15
G293	4.50	0.23	5.36	0.10	6.09	0.21	6.62	0.36	6.62	0.24
E294	5.01	0.23	6.05	0.05	6.69	0.14	7.23	0.21	7.28	0.07
N295	4.16	0.16	5.07	0.15	5.77	0.15	6.18	0.29	6.24	0.08
V296	3.87	0.10	4.66	0.21	5.23	0.08	5.47	0.18	5.62	0.13
T297	3.91	0.21	4.78	0.08	5.43	0.06	5.96	0.24	5.90	0.14
I298	4.62	0.22	5.50	0.14	6.07	0.12	6.91	0.35	6.62	0.15
E299	4.76	0.26	5.77	0.13	6.48	0.12	7.10	0.35	7.09	0.17
S300	2.62	0.18	5.03	0.15	6.18	0.14	6.11	0.82	6.68	0.26
V301	4.84	0.25	5.55	0.10	6.35	0.20	6.49	0.39	6.51	0.16
A302	4.53	0.26	5.33	0.09	6.64	0.22	6.84	0.35	7.11	0.18
D303	4.59	0.27	5.53	0.16	6.42	0.20	6.65	0.34	6.92	0.23
Y304	4.38	0.22	5.10	0.13	5.96	0.15	6.59	0.26	6.62	0.19
F305	4.30	0.19	5.36	0.07	6.13	0.10	6.46	0.15	6.56	0.07
K306	4.11	0.18	4.74	0.07	5.86	0.17	5.96	0.28	6.31	0.22
Q307	4.90	0.23	5.89	0.15	6.71	0.10	7.19	0.29	7.24	0.14
I308	4.20	0.20	5.28	0.18	6.49	0.25	6.68	0.33	6.72	0.10
G309	4.60	0.35	5.38	0.17	6.05	0.11	6.74	0.43	6.63	0.21
I310	4.25	0.12	5.30	0.32	5.88	0.11	6.34	0.20	6.91	0.17
I311	4.58	0.17	5.79	0.25	6.50	0.20	7.18	0.26	7.06	0.19
T313	4.09	0.11	5.04	0.12	5.97	0.19	6.17	0.14	6.38	0.08
N314	4.49	0.28	5.33	0.14	5.98	0.10	6.49	0.32	6.48	0.15

T317	4.22	0.15	4.94	0.09	5.51	0.07	5.97	0.28	6.07	0.09
G318	4.25	0.23	5.12	0.13	5.81	0.09	6.34	0.23	6.19	0.10
Q319	3.89	0.15	4.64	0.10	5.29	0.18	5.64	0.26	5.73	0.17
M321	3.91	0.43	4.90	0.35	5.16	0.48	5.34	0.43	5.52	0.20
I322	4.04	0.21	4.98	0.12	5.33	0.07	6.23	0.30	5.96	0.18
L324	3.99	0.29	4.88	0.12	5.48	0.13	6.13	0.33	6.04	0.24
T326	4.58	0.33	5.38	0.20	6.23	0.12	6.76	0.23	6.89	0.20
D327	4.51	0.17	5.41	0.10	6.33	0.15	6.64	0.18	6.69	0.07
E329	4.48	0.23	5.50	0.15	6.09	0.12	6.33	0.22	6.51	0.14
T330	4.49	0.12	5.64	0.05	6.50	0.13	7.08	0.28	7.19	0.12
G331	3.97	0.16	4.90	0.12	5.71	0.16	6.03	0.22	5.99	0.16
K332	3.60	0.28	3.78	0.11	3.88	0.09	4.20	0.29	4.05	0.09
G335	4.57	0.19	5.53	0.09	6.65	0.26	6.91	0.09	7.16	0.14
T338	4.15	0.14	5.05	0.15	5.74	0.11	6.19	0.19	6.26	0.10
V339	3.83	0.45	4.38	0.40	4.98	0.31	5.81	0.25	6.00	0.20
S340	4.45	0.23	5.37	0.05	5.97	0.10	6.56	0.19	6.62	0.09
F341	4.03	0.19	4.81	0.03	5.65	0.07	6.05	0.29	5.83	0.13
D343	3.92	0.31	4.44	0.29	5.05	0.26	5.09	0.51	5.14	0.30
S346	4.46	0.22	5.26	0.10	5.85	0.14	6.49	0.25	6.44	0.22
A347	4.75	0.34	5.59	0.29	6.56	0.11	7.16	0.36	6.80	0.31
A349	3.82	0.28	4.88	0.22	5.46	0.21	6.17	0.22	6.27	0.09
A350	4.67	0.26	5.96	0.21	6.43	0.24	7.20	0.09	6.86	0.06
I351	4.23	0.25	5.46	0.25	5.99	0.18	6.56	0.29	6.61	0.15
D352	4.60	0.23	5.59	0.19	6.43	0.16	6.94	0.39	7.03	0.25
W353	4.29	0.10	5.53	0.10	6.13	0.11	6.42	0.14	6.58	0.06
F354	4.13	0.10	5.24	0.21	6.05	0.09	6.44	0.16	6.38	0.14
D355	4.64	0.24	5.57	0.16	6.49	0.08	6.96	0.26	7.05	0.10
G356	4.22	0.16	4.96	0.11	5.94	0.11	6.33	0.29	6.39	0.14
E358	2.89	0.05	3.57	0.09	4.33	0.05	4.58	0.06	4.69	0.10
F359	3.80	0.11	4.83	0.09	5.28	0.06	5.80	0.21	5.88	0.15
S360	4.91	0.71	5.29	0.63	6.37	0.22	6.29	1.06	6.00	0.47
G361	4.28	0.22	5.06	0.21	5.78	0.15	6.29	0.39	6.55	0.20

N362	3.92	0.22	4.57	0.09	5.38	0.13	5.66	0.23	5.86	0.16
I364	3.08	0.31	3.95	0.73	5.55	0.58	6.36	0.68	5.51	1.04
V366	4.26	0.20	5.39	0.40	5.47	0.33	6.10	0.12	5.94	0.22
S367	4.23	0.18	5.16	0.13	5.79	0.11	6.44	0.30	6.43	0.10
A369	4.99	0.55	6.24	0.22	6.38	0.22	6.65	0.44	6.92	0.19
T370	3.87	0.38	4.77	0.18	5.14	0.12	5.72	0.32	5.98	0.12
R372	3.75	0.30	4.05	0.47	4.84	0.27	4.56	0.50	5.25	0.50
D374	4.08	0.28	4.29	0.06	4.48	0.05	4.79	0.33	4.55	0.09

Table S5: $R_{2\rho}$ relaxation rates measured using HSn pulses (n=1,2,4,6,8) from HARD experiment for FUS-RRM (pH 6.4) at 600 MHz NMR spectrometer. Only data for which good fits were obtained have been shown.

Residue Number	**$R_{2\rho}$ (s^{-1})**									
	HS1		**HS2**		**HS4**		**HS6**		**HS8**	
	Value	**Error**	**Value**	**Error**	**Value**	**Error**	**Value**	**Error**	**Value**	**Error**
D283	11.92	0.73	11.45	0.95	12.13	1.10	10.26	1.31	10.90	1.31
N285	14.75	1.07	15.00	0.32	14.24	0.74	11.99	0.22	12.18	0.70
F288	13.72	0.46	13.83	0.49	13.01	1.40	10.74	1.28	10.69	0.75
V289	15.90	1.70	14.41	1.90	15.38	0.97	13.52	1.01	12.76	0.62
Q290	13.99	0.26	13.32	0.33	12.63	0.23	10.98	0.54	10.53	0.25
G291	14.10	1.05	13.41	1.35	14.10	0.65	11.88	0.42	12.66	0.14
G293	14.52	0.84	13.93	0.66	13.73	0.78	12.32	0.95	12.74	1.21
E294	15.73	0.43	15.88	0.32	15.82	0.18	13.42	0.43	13.71	0.15
N295	12.53	0.17	12.36	0.38	12.44	0.64	10.37	0.50	10.93	0.07
V296	11.71	0.94	11.41	0.59	10.46	1.94	8.25	1.35	9.27	1.03
T297	13.11	0.50	12.62	0.79	12.79	0.40	11.13	0.40	11.31	0.15
I298	15.53	0.54	15.21	0.46	14.05	0.88	11.67	0.93	11.73	0.77
E299	15.15	0.41	14.87	0.35	14.55	0.52	12.43	0.43	12.78	0.54
S300	13.49	0.82	12.41	0.71	14.18	0.68	12.31	0.50	12.79	1.45
V301	15.44	1.33	14.85	1.63	15.15	1.36	12.80	0.60	12.82	0.94
A302	15.08	0.91	14.75	1.12	14.34	0.55	12.43	0.50	12.82	0.72
D303	15.29	0.41	14.99	0.26	14.56	0.87	11.98	0.19	12.29	0.47

Y304	14.38	0.57	13.53	0.47	13.34	1.49	12.00	1.11	12.58	1.03
F305	14.78	1.07	14.08	1.33	13.60	0.40	12.48	0.84	12.23	1.18
K306	14.23	0.29	13.64	0.29	13.83	0.90	11.88	0.65	12.55	1.25
Q307	14.52	0.61	14.29	0.30	13.71	0.64	12.42	0.85	12.70	1.13
I308	13.56	1.15	12.98	0.43	12.76	1.57	11.64	1.70	12.24	1.44
G309	14.67	0.18	14.30	0.30	14.12	0.41	12.42	0.19	12.23	0.57
I310	14.11	1.13	13.44	0.30	13.53	0.92	11.56	1.39	11.42	1.65
I311	16.73	0.67	15.89	0.66	16.02	0.58	13.99	0.55	13.52	0.70
T313	14.92	0.25	14.80	0.35	14.05	0.73	12.07	0.31	12.04	0.62
N314	14.71	0.27	14.72	0.04	14.28	0.70	11.90	0.56	11.83	0.73
T317	13.22	0.40	13.08	0.63	12.90	1.06	11.45	0.53	11.71	0.70
G318	13.72	0.25	13.28	0.50	13.30	0.34	11.65	0.26	11.93	0.31
Q319	12.42	0.36	12.06	0.25	12.05	0.55	10.35	0.34	10.37	0.46
M321	14.60	1.33	15.99	1.18	14.73	3.13	10.44	2.63	11.00	3.37
I322	13.92	0.97	13.17	1.09	12.06	1.25	10.44	0.28	10.15	0.52
L324	13.32	0.52	13.13	0.42	12.51	0.32	10.48	0.68	10.57	0.35
T326	14.95	0.52	14.26	0.75	14.57	1.21	11.82	0.64	13.15	0.44
D327	15.13	0.14	15.02	0.28	14.51	0.90	12.48	0.54	12.61	0.61
E329	13.13	0.40	13.08	0.14	13.01	0.32	10.88	0.20	11.35	0.61
T330	17.69	0.81	16.78	0.33	16.37	1.00	14.26	1.26	14.26	1.50
G331	13.56	0.48	12.79	0.64	13.49	0.96	11.54	0.36	11.91	0.91
K332	6.46	0.32	6.56	0.24	6.90	0.44	5.53	0.26	6.26	0.53
G335	16.63	1.68	15.84	0.80	16.68	2.19	14.58	2.07	14.84	1.97
T338	13.95	1.17	13.80	0.74	13.85	1.37	12.62	1.02	12.46	1.38
V339	16.34	1.39	14.77	1.81	12.26	2.00	10.73	0.48	9.49	0.63
S340	14.36	0.05	14.19	0.21	13.18	0.91	11.43	0.60	11.63	0.87
F341	13.51	0.52	12.80	0.82	13.45	0.99	11.75	0.50	11.40	0.41
D343	10.83	1.50	10.68	0.71	10.78	1.73	10.88	3.03	12.97	4.08
S346	14.99	0.39	14.39	0.25	13.90	0.34	11.82	0.64	11.53	0.67
A347	16.69	0.79	15.69	1.28	16.17	2.33	14.42	1.61	13.89	1.28
A349	15.07	0.64	15.65	1.01	13.77	2.16	12.22	0.83	10.31	0.28
A350	15.75	0.95	15.76	0.83	15.79	0.34	13.02	0.81	12.97	0.77

I351	16.76	0.80	15.73	1.25	14.41	1.83	12.14	0.52	12.15	0.22
D352	15.28	0.66	14.92	0.41	14.74	0.66	12.56	0.59	13.05	0.73
W353	14.72	0.17	14.69	0.12	13.87	0.45	11.72	0.39	11.44	0.13
F354	17.20	1.11	16.63	0.48	15.97	1.08	13.08	0.98	12.41	1.45
D355	15.98	0.39	15.77	0.20	15.15	0.71	13.10	0.56	13.66	0.79
G356	17.11	0.61	15.98	0.29	15.72	0.86	13.00	0.72	12.80	1.02
E358	12.68	0.09	11.77	0.08	11.34	0.56	9.76	0.33	9.64	0.14
F359	15.50	1.16	14.29	0.53	14.01	0.98	11.29	1.31	11.37	1.44
S360	19.34	1.23	18.11	2.06	19.07	1.37	16.45	2.28	17.49	1.94
G361	14.40	0.84	14.31	0.18	14.71	1.31	12.62	0.65	12.88	0.83
N362	12.30	0.35	11.73	0.06	11.82	1.03	10.48	0.67	10.78	0.77
I364	15.01	3.47	15.22	0.93	13.53	2.33	8.17	1.07	12.39	1.59
V366	12.85	2.06	13.05	1.42	14.14	1.45	12.11	1.79	11.90	2.05
S367	14.48	0.44	13.82	0.44	13.67	0.69	11.56	0.42	11.30	0.14
A369	15.03	1.01	14.31	1.24	14.19	1.87	10.72	1.29	11.47	2.86
T370	13.29	0.83	12.62	0.78	12.83	1.71	11.26	1.60	11.96	1.71
R372	10.53	1.46	10.41	1.81	9.87	0.58	8.76	0.74	10.60	2.70
D374	7.73	0.32	7.63	0.14	8.00	0.34	6.26	0.31	7.12	0.43

Table S6: Fit parameters obtained after global fitting from HARD experiment for FUS-RRM (pH 6.4) at 600 MHz NMR spectrometer.

Residue	**Δω (kHz)**	**Error**	**k_{ex} (kHz)**	**Error**	**P_M (%)**	**Error**
D283	0.99	0.27	35.00	2.86	97.85	2.76
N285	0.68	0.37	39.89	2.39	88.76	11.24
F288	0.71	0.33	36.68	3.66	92.05	8.69
V289	0.83	0.35	28.17	1.66	96.05	3.45
Q290	0.96	0.28	33.94	2.56	97.60	2.50
G291	0.98	0.19	35.15	2.49	98.19	0.94
G293	0.78	0.30	43.88	2.71	95.21	3.13
N295	0.90	0.32	49.40	3.14	93.96	10.01
V296	0.40	0.11	50.33	0.35	84.42	8.09

T297	0.80	0.33	37.71	2.83	95.52	4.46
V298	0.96	0.30	38.17	2.67	95.68	6.82
E299	0.71	0.28	47.63	2.87	92.64	5.17
S300	1.12	0.17	39.67	1.45	98.66	0.73
V301	0.79	0.31	36.47	3.48	95.23	3.81
A302	0.81	0.30	42.88	2.29	95.08	3.70
D303	0.85	0.40	43.38	3.34	90.84	12.42
Y304	0.89	0.35	40.66	2.90	94.17	9.46
F305	0.73	0.33	38.75	2.31	93.60	5.18
K306	0.63	0.22	38.74	1.94	94.33	3.02
Q307	0.54	0.26	57.51	1.65	83.61	11.64
I308	0.47	0.15	51.70	0.60	84.00	10.49
G309	0.96	0.33	41.92	2.24	96.78	2.76
I310	1.16	0.18	40.45	1.20	98.58	1.13
I311	1.02	0.23	34.76	2.62	97.97	1.38
T313	0.68	0.34	37.58	2.89	90.21	11.02
N314	1.09	0.16	38.50	2.06	98.53	0.60
T317	1.04	0.25	39.61	1.59	98.16	1.61
G318	0.97	0.33	39.10	2.12	96.97	3.15
M321	0.92	0.21	28.60	2.10	98.02	1.61
I322	1.21	0.03	40.56	0.82	98.98	0.06
L324	0.86	0.30	41.42	2.27	96.46	3.07
T326	0.90	0.28	39.39	3.22	96.77	2.35
D327	0.99	0.27	39.00	2.37	97.60	2.08
E329	0.68	0.36	53.22	3.14	87.72	12.51
T331	1.10	0.16	36.44	2.93	98.74	0.63
K332	0.52	0.24	130.71	5.57	81.17	13.22
T338	0.98	0.24	36.31	2.65	97.88	1.90
V339	0.66	0.42	36.14	1.21	82.64	16.93
S340	0.85	0.35	44.28	3.76	94.36	6.23
F341	0.92	0.32	37.98	3.36	96.88	2.86
S346	0.79	0.27	36.96	3.02	96.02	3.04
A347	0.70	0.36	37.28	3.57	92.51	4.40
A349	0.62	0.35	36.34	1.06	86.70	14.35

A350	0.88	0.25	36.10	2.64	96.69	3.06
I351	0.91	0.31	35.11	2.36	96.34	4.02
D352	0.80	0.31	43.61	2.84	92.57	11.11
W353	0.77	0.37	41.59	2.15	90.74	10.53
F354	1.07	0.13	27.75	2.20	98.65	0.66
D355	0.89	0.27	39.01	2.88	96.14	3.97
G356	1.13	0.12	29.08	1.53	98.80	0.30
E358	1.07	0.11	25.62	1.49	99.14	0.27
F359	1.10	0.11	27.51	2.10	98.93	0.18
S360	1.08	0.13	20.74	1.65	98.82	0.50
G361	1.12	0.11	35.35	2.65	98.77	0.48
N362	0.63	0.34	45.59	2.66	86.78	14.06
I364	0.24	0.03	32.55	0.85	68.50	7.68
V366	0.76	0.25	36.58	2.91	96.07	2.92
S367	0.76	0.42	40.50	1.76	86.97	15.63
R372	0.93	0.23	32.38	3.44	98.18	1.90
D374	0.53	0.25	98.58	4.69	83.80	13.00

Table S7: R_1 relaxation rates measured from HARD experiment in presence of ATP for FUS-RRM (pH 6.4) at 600 MHz NMR spectrometer. Only data for which good fits were obtained have been shown.

Residue	**R_1 (s^{-1})**	**Error**
285	1.43	0.04
287	1.58	0.12
288	1.51	0.04
289	1.38	0.14
290	1.32	0.03
294	1.26	0.04
295	1.36	0.03
296	1.19	0.05
297	1.36	0.03
298	1.41	0.04
300	1.32	0.05

301	1.44	0.05
302	1.64	0.05
303	0.99	0.02
304	1.45	0.02
305	1.52	0.04
306	1.31	0.06
307	1.53	0.02
308	1.59	0.04
309	1.41	0.03
310	1.21	0.03
311	1.31	0.07
313	1.45	0.03
314	1.29	0.06
317	1.35	0.03
318	1.39	0.02
319	1.44	0.02
322	1.42	0.05
323	1.69	0.04
324	1.37	0.04
326	1.31	0.05
327	1.40	0.03
329	1.24	0.02
330	1.25	0.04
331	1.36	0.04
332	1.58	0.01
335	1.32	0.08
338	1.40	0.04
340	1.45	0.04
341	1.41	0.05
346	1.37	0.02
347	1.41	0.07
349	1.54	0.03
350	1.50	0.07
351	1.43	0.04

352	1.41	0.03
353	1.39	0.04
355	1.42	0.02
356	1.47	0.03
358	1.61	0.02
360	1.60	0.04
361	1.36	0.04
362	1.40	0.02
367	1.47	0.02
369	1.44	0.18
372	1.76	0.05

Table S8: $R_{1\rho}$ relaxation rates measured using HSn pulses (n=1,2,4,6,8) from HARD experiment in presence of ATP for FUS-RRM (pH 6.4) at 600 MHz NMR spectrometer. Only data for which good fits were obtained have been shown.

Residue Number	**$R_{1\rho}$ (s^{-1})**									
	HS1		**HS2**		**HS4**		**HS6**		**HS8**	
	Value	**Error**	**Value**	**Error**	**Value**	**Error**	**Value**	**Error**	**Value**	**Error**
285	4.23	0.10	4.91	0.22	5.59	0.30	5.28	0.14	6.25	0.23
287	4.18	0.49	4.97	0.28	6.42	0.56	4.78	0.38	5.46	0.39
288	3.87	0.17	5.23	0.54	5.84	0.43	5.52	0.27	5.81	0.11
289	4.62	0.45	5.40	1.56	7.69	0.55	6.67	0.33	8.26	1.13
290	3.53	0.06	4.08	0.13	5.51	0.11	4.95	0.10	5.13	0.10
294	5.52	0.34	6.18	0.26	7.34	0.18	6.93	0.07	7.54	0.22
295	3.58	0.11	4.62	0.53	5.87	0.20	5.20	0.30	5.17	0.24
296	4.20	0.22	4.37	0.12	5.25	0.18	5.11	0.26	5.33	0.23
297	3.74	0.10	3.96	0.27	4.27	0.43	4.20	0.22	5.23	0.09
298	3.97	0.23	4.70	0.17	4.73	0.71	5.24	0.18	6.01	0.17
300	4.54	0.43	4.62	0.28	6.49	0.45	5.59	0.30	6.00	0.28
301	4.84	0.19	5.67	0.39	6.43	0.43	6.27	0.34	7.31	0.41
302	4.99	0.43	5.86	1.16	7.21	0.46	6.66	0.35	6.87	0.42
303	3.81	0.14	3.29	0.68	2.31	0.55	2.39	0.37	4.36	0.11

304	4.77	0.28	5.00	0.50	6.16	0.30	5.88	0.26	6.11	0.26
305	4.61	0.22	5.17	0.47	5.78	0.33	5.74	0.15	6.08	0.18
306	4.24	0.30	4.45	0.51	5.33	0.54	4.78	0.14	5.37	0.20
307	5.03	0.18	6.15	0.37	6.81	0.50	7.18	0.33	7.34	0.33
308	4.46	0.23	5.31	0.42	6.56	0.47	6.56	0.16	6.33	0.25
309	3.92	0.07	4.85	0.48	5.68	0.17	5.46	0.10	5.38	0.17
310	4.61	0.16	5.17	0.56	6.33	0.34	6.12	0.25	6.60	0.18
311	5.02	0.19	5.64	0.56	6.70	0.39	6.64	0.26	6.90	0.24
313	4.12	0.26	5.00	0.25	5.67	0.29	5.65	0.33	6.05	0.33
314	4.41	0.16	4.78	0.44	5.95	0.08	5.83	0.17	6.05	0.20
317	4.58	0.21	4.90	0.45	5.82	0.23	5.62	0.12	5.95	0.21
318	3.85	0.19	4.31	0.30	5.46	0.11	5.20	0.15	5.72	0.25
319	3.49	0.08	3.68	0.06	5.08	0.22	4.48	0.11	4.69	0.12
322	3.70	0.14	4.62	0.34	5.53	0.10	4.76	0.27	4.92	0.13
323	4.68	0.13	5.60	0.31	5.70	0.19	5.44	0.29	6.14	0.39
324	3.41	0.15	4.00	0.19	5.19	0.23	4.55	0.23	4.47	0.15
326	4.49	0.10	4.68	1.00	5.58	0.23	5.87	0.17	5.85	0.13
327	4.43	0.08	4.94	0.38	5.93	0.06	6.14	0.11	6.52	0.12
329	4.82	0.22	5.44	0.56	6.23	0.34	6.24	0.22	6.53	0.16
330	5.32	0.16	5.86	0.21	6.86	0.15	6.97	0.19	7.62	0.19
331	4.04	0.07	4.30	0.14	5.58	0.16	5.31	0.17	5.70	0.24
332	4.06	0.26	3.95	0.32	4.71	0.16	4.29	0.21	4.24	0.22
335	4.19	0.12	5.16	0.21	5.90	0.44	6.57	0.36	6.48	0.61
338	3.76	0.16	5.10	0.32	5.11	0.31	5.57	0.10	5.32	0.21
340	5.06	0.32	5.99	0.40	6.35	0.11	6.29	0.08	6.62	0.25
341	3.43	0.20	4.16	0.11	5.15	0.15	5.18	0.25	4.75	0.16
346	4.51	0.17	4.71	0.35	5.92	0.19	5.89	0.21	6.24	0.26
347	4.69	0.42	4.80	0.41	5.55	0.47	6.43	0.28	6.23	0.31
349	4.48	0.17	4.83	0.31	5.84	0.10	5.55	0.23	6.45	0.10
350	4.08	0.18	4.75	0.35	6.34	0.14	5.74	0.45	6.19	0.16
351	4.47	0.45	5.37	0.92	6.84	0.15	6.18	0.37	6.30	0.21
352	4.55	0.30	5.26	0.70	6.55	0.35	6.38	0.19	6.43	0.20

353	4.46	0.16	5.67	0.16	4.17	1.28	6.67	0.15	6.41	0.18
355	4.34	0.14	5.03	0.23	6.01	0.33	6.20	0.22	6.36	0.18
356	4.07	0.29	4.48	0.25	6.27	0.09	5.89	0.33	5.47	0.36
358	4.09	0.24	4.19	0.23	4.50	0.15	4.39	0.14	4.74	0.21
360	5.08	0.20	5.98	0.36	5.97	0.38	6.32	0.34	6.80	0.17
361	4.19	0.26	4.63	0.22	5.16	0.44	5.69	0.27	5.82	0.13
362	3.70	0.11	4.05	0.16	5.46	0.20	4.84	0.09	5.22	0.19
367	4.36	0.18	5.25	0.22	6.45	0.04	5.98	0.11	6.48	0.14
369	4.77	0.39	5.13	0.80	6.66	0.52	7.05	0.65	6.39	0.54
372	4.03	0.31	3.76	0.81	4.90	0.39	4.53	0.26	4.52	0.20

Table S9: $R_{2\rho}$ relaxation rates measured using HSn pulses (n=1,2,4,6,8) from HARD experiment in presence of ATP for FUS-RRM (pH 6.4) at 600 MHz NMR spectrometer. Only data for which good fits were obtained have been shown.

Residue Number	**$R_{2\rho}$ (s^{-1})**									
	HS1		**HS2**		**HS4**		**HS6**		**HS8**	
	Value	**Error**	**Value**	**Error**	**Value**	**Error**	**Value**	**Error**	**Value**	**Error**
285	13.69	0.38	12.95	0.39	12.37	1.91	13.19	0.44	13.07	0.23
287	14.17	1.08	13.62	0.67	12.66	1.49	13.91	1.87	12.63	0.52
288	13.92	0.68	12.46	0.34	11.77	1.75	11.39	0.58	13.58	0.75
289	16.73	0.80	19.53	1.53	19.09	2.58	14.38	1.10	16.63	0.77
290	13.14	0.28	12.75	0.18	12.16	2.33	12.04	0.37	12.58	0.12
294	16.29	0.29	15.87	0.36	16.15	2.16	14.75	1.14	15.86	0.33
295	11.22	0.32	11.03	0.29	11.09	0.72	11.03	0.59	10.76	0.64
296	10.10	0.64	9.68	0.20	9.00	0.84	9.88	0.65	9.68	0.61
297	12.23	0.18	11.38	0.12	11.45	0.70	11.60	0.42	11.40	0.12
298	13.84	0.41	13.23	0.20	12.78	2.16	13.24	0.44	12.30	0.22
300	8.72	0.47	8.48	0.36	10.81	0.91	10.49	1.51	8.49	0.45
301	15.91	0.53	14.30	0.97	13.44	4.08	9.94	3.12	14.93	0.85
302	15.06	0.80	13.21	1.06	14.25	1.60	13.96	1.22	12.38	0.71
303	12.13	0.22	11.63	0.17	11.61	0.42	10.58	0.26	11.12	0.31

304	13.20	0.44	11.91	0.25	12.25	1.11	12.06	0.47	12.78	0.66
305	13.72	0.37	12.71	0.14	13.41	0.89	13.11	0.44	12.99	0.42
306	12.42	0.27	12.38	0.54	11.17	1.96	12.12	0.72	11.66	0.55
307	13.74	0.51	13.38	0.39	12.97	1.70	12.43	0.56	13.28	0.77
308	13.58	0.56	12.83	0.49	12.72	1.73	12.04	0.49	13.23	0.47
309	12.93	0.22	12.76	0.23	12.12	1.08	12.49	0.36	12.54	0.17
310	12.12	0.36	12.65	0.38	10.82	1.63	10.67	0.39	12.09	0.25
311	16.06	0.58	15.30	1.07	14.36	2.01	13.52	0.73	14.84	1.16
313	12.80	0.42	11.54	0.53	11.73	1.66	11.42	0.88	12.17	0.79
314	13.13	0.20	12.52	0.06	12.30	0.29	12.14	0.36	12.66	0.42
317	12.15	0.30	11.62	0.22	11.35	0.60	11.22	0.73	11.60	0.57
318	12.40	0.16	11.79	0.16	11.29	0.64	11.38	0.31	11.62	0.32
319	11.05	0.15	10.77	0.27	10.59	1.02	10.20	0.16	10.43	0.24
322	12.35	0.28	11.61	0.42	11.26	0.62	10.45	0.23	11.73	0.24
323	9.74	0.26	9.59	0.09	8.94	1.24	9.16	0.58	9.34	0.13
324	12.85	0.30	11.30	0.46	12.18	0.56	11.31	0.33	11.50	0.45
326	12.67	0.49	12.74	0.59	12.59	0.48	11.71	0.43	12.43	0.54
327	14.65	0.39	14.00	0.33	13.57	0.32	13.14	0.14	13.39	0.20
329	12.44	0.19	12.05	0.25	11.61	0.74	11.14	0.41	11.68	0.46
330	19.20	0.67	17.19	0.44	18.31	1.88	16.66	1.04	18.21	1.00
331	11.57	0.51	11.06	0.44	10.64	0.17	10.47	0.57	11.18	0.56
332	5.23	0.21	5.20	0.34	4.97	0.46	4.94	0.39	5.20	0.49
335	16.38	0.17	14.38	0.50	11.77	2.90	13.58	1.07	15.90	0.87
338	13.20	0.32	13.04	0.36	11.93	1.63	12.15	0.29	12.75	0.74
340	13.21	0.27	13.92	0.52	11.78	0.48	12.06	1.02	13.05	0.44
341	12.59	0.46	12.73	0.58	11.85	0.59	12.49	0.49	12.34	0.69
346	13.12	0.24	12.37	0.12	12.04	0.81	11.93	0.29	12.32	0.15
347	14.93	1.10	14.54	1.04	14.84	2.78	13.36	1.33	14.83	0.84
349	12.73	0.63	11.85	0.30	12.38	0.82	12.88	1.56	11.97	0.57
350	13.55	0.39	12.91	0.52	12.15	0.53	11.90	0.60	12.13	0.45
351	15.12	1.30	14.15	0.85	14.81	1.15	13.78	0.79	13.78	0.41
352	14.90	0.21	14.49	0.26	14.31	0.42	13.43	0.32	13.62	0.20

353	13.91	0.30	9.14	1.73	12.88	1.61	11.51	2.01	12.97	0.37
355	14.13	0.45	13.44	0.44	12.67	1.03	12.69	0.45	12.73	0.28
356	15.73	0.66	14.92	0.57	15.67	1.83	15.00	1.33	14.90	0.93
358	8.72	0.47	8.48	0.36	8.17	1.08	8.29	0.62	8.49	0.45
360	15.59	0.29	14.76	0.41	14.09	1.14	13.39	0.54	13.99	0.31
361	14.42	0.50	13.59	0.47	13.97	2.63	13.58	1.01	14.36	0.89
362	10.87	0.11	10.60	0.14	10.39	0.56	10.66	0.14	10.74	0.19
367	13.12	0.26	12.74	0.31	12.76	0.80	12.23	0.59	12.97	0.30
369	12.16	0.73	11.59	0.68	10.52	0.74	11.39	1.37	10.58	0.45
372	7.96	0.27	8.00	0.25	7.66	0.36	7.89	0.18	7.72	0.18

Table S10: Fit parameters obtained after global fitting from HARD experiment in presence of ATP for FUS-RRM (pH 6.4) at 600 MHz NMR spectrometer.

Residue	**Δω (kHz)**	**Error**	**k_{ex} (kHz)**	**Error**	**P_M (%)**	**Error**
285	0.79	0.23	0.13	0.03	97.69	0.35
288	0.77	0.16	0.17	0.07	98.09	0.52
289	1.17	0.04	0.20	0.13	97.65	0.97
290	0.86	0.26	0.15	0.04	97.50	0.45
294	0.76	0.23	0.12	0.01	97.72	0.24
295	1.19	0.02	0.13	0.02	98.64	0.18
296	0.92	0.26	0.18	0.07	99.46	0.16
297	0.81	0.20	0.17	0.06	97.90	0.57
298	1.25	0.02	0.32	0.20	98.57	0.69
300	0.08	0.20	0.82	1.41	96.81	2.53
301	0.55	0.26	36.62	3.93	84.61	14.79
302	0.49	0.34	41.48	3.67	77.46	13.46
303	1.25	0.02	0.45	0.30	98.28	0.96
304	0.92	0.28	0.15	0.06	98.47	0.43
305	0.73	0.18	0.14	0.01	98.00	0.13
306	1.26	0.02	0.18	0.08	98.12	0.54
307	0.90	0.33	0.13	0.05	99.16	0.22
308	0.78	0.23	0.13	0.03	98.22	0.29

309	0.92	0.26	0.15	0.04	97.89	0.42
310	0.79	0.26	0.12	0.01	99.02	0.08
311	0.75	0.33	36.05	3.25	93.96	4.92
313	0.85	0.27	0.16	0.04	98.74	0.28
314	0.78	0.23	0.12	0.01	98.21	0.18
317	0.94	0.23	0.19	0.09	98.93	0.33
318	1.04	0.24	0.17	0.06	98.41	0.42
319	1.18	0.04	0.19	0.05	98.41	0.32
322	0.94	0.22	0.23	0.13	98.47	0.59
323	0.01	0.00	0.87	0.81	96.83	1.53
324	1.06	0.24	0.27	0.12	98.42	0.60
326	0.72	0.18	0.18	0.08	98.51	0.42
327	1.24	0.03	0.27	0.14	98.54	0.63
329	0.80	0.25	0.11	0.01	99.08	0.05
330	0.86	0.24	0.15	0.06	96.86	0.73
331	1.09	0.20	0.24	0.17	99.03	0.46
332	0.01	0.01	0.84	0.82	95.87	4.01
335	0.80	0.23	0.12	0.02	97.28	0.32
338	1.21	0.04	0.27	0.13	98.60	0.57
340	1.01	0.25	0.13	0.02	98.64	0.17
341	1.14	0.16	0.22	0.08	98.08	0.53
346	0.72	0.19	0.13	0.03	98.34	0.26
347	1.24	0.04	0.33	0.18	98.48	0.73
349	1.05	0.27	0.21	0.11	98.82	0.45
350	1.24	0.05	1.40	2.69	99.19	0.43
351	1.20	0.08	0.67	0.93	98.91	0.42
352	1.23	0.01	0.17	0.10	97.89	0.72
353	0.70	0.02	0.13	0.02	98.87	0.16
355	1.12	0.19	0.25	0.12	98.78	0.42
356	1.24	0.06	0.31	0.22	97.94	1.09
358	0.86	0.26	0.19	0.14	99.27	0.25
360	1.22	0.05	0.37	0.59	98.41	0.66
361	1.14	0.07	0.26	0.15	98.27	0.81
362	0.69	0.18	0.11	0.01	98.23	0.11

367	0.76	0.23	0.12	0.01	98.34	0.13
369	0.57	0.25	76.96	5.15	83.90	12.55
372	0.67	0.14	0.17	0.09	99.43	0.22

Table S11: R_1 relaxation rates measured from HARD experiment for FUS-RRM (pH 4.6) at 600 MHz NMR spectrometer. Only data for which good fits were obtained have been shown.

Residue number	R_1 (s^{-1})		Residue number	R_1 (s^{-1})		Residue number	R_1 (s^{-1})	
	Value	Error		Value	Error		Value	Error
D283	1.53	0.03	I310	1.42	0.07	S346	1.56	0.05
N285	1.52	0.07	I311	1.66	0.09	A347	1.57	0.21
F288	1.77	0.03	T313	1.55	0.04	A349	1.55	0.18
V289	1.5	0.11	N314	1.52	0.05	A350	1.58	0.09
Q290	1.49	0.05	T317	1.49	0.05	I351	1.63	0.1
G291	1.43	0.05	G318	1.56	0.08	D352	1.56	0.06
G293	1.55	0.05	Q319	1.6	0.06	W353	1.46	0.06
E294	1.39	0.06	M321	1.66	0.16	F354	1.63	0.17
N295	1.57	0.03	I322	1.67	0.05	D355	1.56	0.04
V296	1.34	0.14	L324	1.47	0.05	G356	0.85	0.1
T297	1.57	0.07	T326	1.54	0.08	E358	1.53	0.03
I298	1.54	0.07	D327	1.62	0.03	F359	1.65	0.1
E299	1.59	0.03	E329	1.49	0.02	S360	1.55	0.03
S300	0.85	0.51	T330	1.43	0.08	G361	1.57	0.02
V301	1.6	0.08	G331	1.69	0.18	N362	1.57	0.05
A302	1.66	0.08	K332	1.57	0.03	I364	1.62	0.07
D303	1.58	0.05	G335	1.81	0.18	V366	1.62	0.11
Y304	1.62	0.06	T338	1.68	0.11	S367	1.59	0.03
F305	1.65	0.08	V339	1.46	0.19	A369	1.72	0.13
K306	1.58	0.1	S340	1.54	0.04	T370	1.48	0.02
Q307	1.65	0.05	F341	1.58	0.09	R372	1.77	0.11
I308	1.72	0.11	D343	1.66	0.04	D374	1.65	0.04
G309	1.53	0.06						

Table S12: $R_{1\rho}$ relaxation rates measured using HSn pulses (n=1,2,4,6,8) from HARD experiment for FUS-RRM (pH 4.6) at 600 MHz NMR spectrometer. Only data for which good fits were obtained have been shown.

Residue Number	$R_{1\rho}$ (s^{-1})									
	HS1		HS2		HS4		HS6		HS8	
	Value	Error	Value	Error	Value	Error	Value	Error	Value	Error
D283	3.71	0.18	4.28	0.07	4.21	0.09	4.85	0.23	5.11	0.16
N285	4.63	0.27	5.67	0.16	5.50	0.06	6.47	0.40	6.65	0.15
F288	4.76	0.49	4.30	0.34	5.70	0.31	5.39	0.44	6.13	0.29
V289	4.17	0.24	4.68	0.52	6.62	0.97	6.38	0.74	6.65	0.83
Q290	4.54	0.19	4.75	0.22	5.16	0.31	5.95	0.17	6.03	0.38
G291	5.06	0.34	6.35	0.33	5.51	0.17	6.87	0.48	6.61	0.53
G293	5.10	0.21	5.76	0.35	6.11	0.19	6.75	0.34	6.94	0.13
E294	5.56	0.19	6.42	0.07	7.11	0.12	7.94	0.24	7.86	0.21
N295	4.55	0.30	5.46	0.13	5.10	0.07	5.82	0.20	5.84	0.17
V296	4.87	0.23	4.19	0.77	6.29	0.38	6.26	0.41	6.09	0.15
T297	4.14	0.08	4.73	0.21	5.21	0.15	5.72	0.35	6.03	0.37
I298	4.67	0.21	5.49	0.43	5.53	0.29	6.79	0.36	6.66	0.22
E299	5.15	0.08	6.04	0.13	6.09	0.11	6.82	0.16	6.99	0.13
S300	4.72	0.13	5.16	0.52	5.94	0.46	5.81	0.38	6.03	0.46
V301	5.34	0.28	6.19	0.19	6.44	0.42	7.51	0.67	7.42	0.43
A302	4.62	0.11	5.44	0.26	5.90	0.52	6.94	0.59	6.36	0.14
D303	4.67	0.19	5.27	0.16	5.53	0.21	6.43	0.41	6.57	0.56
Y304	4.13	0.16	4.94	0.05	5.55	0.32	6.18	0.36	6.34	0.59
F305	4.65	0.17	5.65	0.11	6.03	0.07	6.56	0.42	6.84	0.43
K306	3.99	0.18	4.47	0.11	4.55	0.09	5.16	0.30	5.64	0.31
Q307	5.19	0.31	6.35	0.18	6.33	0.16	7.13	0.22	7.37	0.11
I308	4.98	0.60	6.06	0.44	5.41	0.20	5.97	0.31	6.87	0.65
G309	4.40	0.07	5.26	0.15	5.52	0.14	6.16	0.20	6.16	0.07
I310	5.44	0.21	6.44	0.33	5.65	0.27	6.12	0.32	7.24	0.62
I311	4.83	0.36	6.23	0.33	7.35	0.16	7.36	0.45	7.66	0.21
T313	4.69	0.13	4.94	0.21	5.06	0.20	5.95	0.48	6.25	0.30
N314	4.67	0.23	5.47	0.14	5.58	0.07	6.44	0.45	6.56	0.25

T317	5.32	0.13	5.44	0.21	5.76	0.23	6.37	0.29	6.85	0.26
G318	4.43	0.23	4.86	0.28	5.29	0.02	5.79	0.29	6.20	0.35
Q319	3.93	0.17	4.77	0.20	4.71	0.09	5.20	0.23	5.42	0.17
M321	4.65	0.71	5.59	0.35	6.81	1.12	6.98	2.17	8.29	1.05
I322	4.31	0.42	5.25	0.31	5.29	0.32	6.22	0.34	5.97	0.24
L324	4.33	0.34	4.77	0.35	4.46	0.25	6.10	0.38	5.94	0.46
T326	5.79	0.56	6.51	0.37	6.46	0.44	6.92	0.28	7.05	0.37
D327	4.62	0.16	5.16	0.19	5.77	0.15	6.82	0.21	6.94	0.06
E329	5.51	0.06	6.61	0.27	6.54	0.17	7.09	0.09	7.76	0.13
T330	5.52	0.15	7.26	0.10	8.81	0.29	9.87	0.08	9.39	0.22
G331	4.81	0.22	4.33	0.97	5.24	0.35	6.10	0.35	6.51	0.72
K332	3.37	0.10	3.60	0.06	3.37	0.02	3.80	0.23	4.04	0.05
G335	5.59	0.22	5.74	1.05	8.09	0.50	7.77	0.66	9.15	0.62
T338	5.01	0.50	5.97	0.40	6.59	0.26	6.62	0.29	7.11	0.24
V339	4.76	0.29	5.19	0.51	6.60	0.41	5.92	1.26	5.20	0.62
S340	5.58	0.40	6.32	0.40	6.15	0.45	7.38	0.25	6.92	0.41
F341	4.63	0.25	4.70	0.21	4.44	0.20	5.68	0.43	5.70	0.39
D343	4.35	0.37	5.17	0.42	4.91	0.31	5.22	0.25	5.70	0.16
S346	4.65	0.13	5.09	0.14	5.29	0.15	6.35	0.32	6.31	0.07
A347	4.48	0.75	4.68	1.03	4.83	0.16	6.27	0.90	7.05	1.53
A349	4.34	0.48	5.55	0.24	6.01	1.11	7.72	0.41	6.25	0.58
A350	5.67	0.18	6.38	0.36	7.05	0.17	8.25	0.75	7.09	0.38
I351	4.52	0.06	5.63	0.32	6.28	0.47	6.41	0.46	6.63	0.53
D352	5.27	0.13	6.14	0.26	6.03	0.07	6.50	0.16	6.92	0.16
W353	5.32	0.46	6.56	0.33	6.75	0.39	7.00	0.19	7.30	0.31
F354	4.86	0.30	5.66	0.29	5.89	0.25	6.73	0.63	6.11	0.50
D355	4.99	0.10	5.69	0.11	6.12	0.17	7.00	0.18	7.07	0.15
G356	2.85	0.37	3.12	0.22	3.12	0.06	3.39	0.46	2.83	0.32
E358	2.86	0.10	3.06	0.14	2.90	0.14	3.26	0.21	3.46	0.11
F359	4.28	0.18	4.85	0.20	4.81	0.36	5.43	0.25	5.43	0.38
S360	5.71	0.32	6.40	0.45	6.64	0.29	7.60	0.29	7.34	0.08
G361	4.40	0.24	5.02	0.41	5.06	0.17	5.70	0.21	6.54	0.52

N362	3.96	0.11	4.79	0.04	4.62	0.05	5.18	0.23	5.14	0.13
I364	5.06	0.19	5.62	0.40	5.97	0.54	6.92	0.34	6.89	0.34
V366	5.38	0.62	5.86	0.55	7.12	0.63	7.15	0.28	6.11	0.49
S367	4.56	0.23	5.21	0.16	5.38	0.17	5.97	0.48	6.15	0.19
A369	4.33	0.48	5.63	0.44	6.29	0.57	7.25	0.71	6.66	0.27
T370	4.25	0.18	4.49	0.23	4.55	0.08	5.20	0.34	5.28	0.22
R372	3.65	0.27	3.93	0.16	3.78	0.42	4.44	0.42	4.33	0.45
D374	4.59	0.16	4.82	0.23	4.60	0.17	4.87	0.05	5.17	0.05

Table S13: $R_{2\rho}$ relaxation rates measured using HSn pulses (n=1,2,4,6,8) from HARD experiment for FUS-RRM (pH 4.6) at 600 MHz NMR spectrometer. Only data for which good fits were obtained have been shown.

Residue Number	**$R_{2\rho}$ (s^{-1})**									
	HS1		**HS2**		**HS4**		**HS6**		**HS8**	
	Value	**Error**	**Value**	**Error**	**Value**	**Error**	**Value**	**Error**	**Value**	**Error**
D283	9.47	0.16	9.61	0.20	10.13	0.13	9.07	0.18	9.43	0.30
N285	13.36	0.31	13.98	0.42	13.49	0.17	12.62	0.33	13.70	0.73
F288	13.30	0.36	11.99	0.92	13.70	0.79	12.45	0.43	13.81	1.06
V289	13.47	0.79	13.80	0.64	14.38	0.44	12.55	1.22	13.81	0.58
Q290	13.60	0.51	13.10	0.39	13.21	0.45	11.28	0.74	12.66	0.64
G291	13.11	0.40	13.22	0.84	13.41	0.13	12.48	0.49	12.41	0.70
G293	14.20	0.24	13.89	0.78	14.47	0.32	13.25	0.31	15.56	0.70
E294	19.17	0.32	19.16	0.60	18.70	0.30	17.90	0.55	19.00	0.41
N295	11.63	0.21	11.81	0.50	11.54	0.60	11.33	0.19	11.09	0.51
V296	9.45	0.62	10.00	0.63	8.89	0.61	10.57	0.31	9.25	0.14
T297	12.47	0.07	13.26	0.39	12.99	0.51	12.60	0.28	12.39	0.33
I298	12.85	0.41	13.93	0.34	14.00	0.22	12.29	0.65	13.32	0.30
E299	13.48	0.12	14.24	0.25	13.85	0.32	13.56	0.31	13.79	0.57
S300	12.93	0.21	13.89	0.22	13.12	0.22	13.82	1.15	13.19	0.72
V301	11.22	1.28	12.20	1.00	12.20	1.17	12.55	0.63	11.40	0.66
A302	14.27	0.48	12.99	0.49	14.06	0.25	12.67	0.75	13.76	1.23
D303	13.59	0.26	13.48	0.49	13.35	0.38	12.63	0.39	13.63	0.50

Y304	12.92	0.28	12.88	0.30	13.40	0.54	12.06	0.38	13.03	0.50
F305	12.29	0.43	13.66	0.82	13.78	0.32	12.62	0.37	12.90	0.80
K306	13.10	0.38	12.56	0.38	13.30	0.44	12.34	0.39	12.85	0.79
Q307	13.21	0.03	14.00	0.40	13.48	0.38	13.08	0.19	13.73	0.61
I308	13.32	0.34	13.22	0.36	13.24	0.22	12.55	0.48	13.86	1.06
G309	12.74	0.32	13.16	0.47	13.14	0.25	13.00	0.36	13.52	0.42
I310	12.35	0.23	12.78	0.26	11.58	0.54	12.01	0.30	11.22	0.48
I311	16.55	0.62	17.17	1.03	17.33	0.78	16.42	1.12	17.10	0.90
T313	9.32	2.98	13.58	0.54	12.60	0.54	12.39	0.57	13.02	0.53
N314	13.07	0.24	13.10	0.32	13.84	0.24	12.81	0.21	13.88	0.57
T317	12.14	0.42	12.86	0.62	12.83	0.23	12.04	0.42	12.83	0.33
G318	12.07	0.34	12.59	0.19	12.90	0.40	12.02	0.39	12.54	0.74
Q319	10.97	0.12	10.83	0.53	11.01	0.23	10.19	0.11	10.62	0.37
M321	14.69	2.55	12.78	1.90	16.52	1.58	19.67	1.95	15.50	1.89
I322	11.96	0.74	12.70	0.55	12.88	0.30	11.35	0.56	12.69	0.33
L324	11.87	0.47	11.58	0.36	12.20	0.15	10.92	0.33	11.92	0.55
T326	13.03	0.42	15.39	0.57	14.63	0.34	13.23	0.15	13.82	0.75
D327	15.76	0.58	15.15	0.74	16.22	0.37	14.17	0.30	15.75	0.48
E329	13.76	0.11	14.77	0.57	13.99	0.36	12.90	0.36	13.45	0.34
T330	25.32	0.51	24.90	0.66	24.57	0.29	25.92	0.32	25.89	0.50
G331	11.87	0.85	13.41	1.16	12.91	0.78	14.90	1.13	14.31	1.82
K332	4.68	0.06	4.99	0.20	5.54	0.13	4.77	0.17	4.82	0.27
G335	19.85	1.55	20.22	1.26	19.83	2.20	18.38	2.43	19.97	1.11
T338	13.98	0.22	15.47	0.80	13.39	0.89	12.72	1.22	13.93	0.40
V339	12.26	0.51	12.93	0.35	13.18	0.52	12.24	0.64	11.88	0.90
S340	13.23	0.22	14.25	0.78	13.89	0.70	13.04	0.29	13.89	0.06
F341	12.33	0.77	12.73	0.40	13.86	0.42	11.83	0.56	12.35	0.49
D343	6.86	0.03	7.86	0.25	8.05	0.20	7.11	0.12	7.41	0.50
S346	12.40	0.16	12.71	0.16	12.43	0.22	12.16	0.24	12.55	0.39
A347	16.04	1.21	16.92	2.10	18.69	0.41	15.42	1.12	16.73	0.76
A349	12.53	0.60	14.24	1.21	13.89	0.80	13.20	0.97	13.08	2.38
A350	13.47	0.67	13.97	0.46	13.68	0.46	12.98	0.72	13.72	0.26

I351	14.24	0.63	15.29	0.31	15.78	0.64	13.36	0.60	15.01	0.92
D352	15.02	0.32	15.57	0.44	14.91	0.50	14.37	0.46	14.89	0.17
W353	13.36	0.42	13.91	0.76	14.64	0.80	12.89	0.32	12.05	0.43
F354	18.53	1.14	18.26	1.02	17.79	0.37	19.92	2.08	16.05	1.19
D355	14.48	0.18	14.08	0.13	13.92	0.15	14.11	0.20	14.10	0.61
G356	6.51	0.25	6.42	0.43	7.33	0.51	5.97	0.19	6.06	0.20
E358	4.96	0.11	5.09	0.25	5.72	0.20	5.12	0.12	5.06	0.21
F359	14.83	0.39	15.59	0.21	14.86	0.19	15.80	0.35	15.85	1.28
S360	16.88	0.33	17.81	0.53	16.12	0.83	16.66	0.22	16.25	0.38
G361	15.38	0.27	14.99	0.40	15.73	0.52	15.87	0.74	15.89	1.01
N362	10.66	0.17	10.64	0.35	11.30	0.34	10.38	0.25	11.05	0.59
I364	12.66	0.70	14.39	0.82	13.25	0.88	13.20	0.49	12.28	0.31
V366	13.67	0.94	14.17	0.84	12.13	0.90	13.38	1.75	14.73	1.05
S367	12.33	0.30	12.79	0.30	12.76	0.31	11.93	0.27	12.86	0.38
A369	13.80	1.21	13.19	0.65	12.95	0.57	13.04	0.42	12.73	0.58
T370	11.55	0.22	11.38	0.57	11.57	0.24	10.65	0.40	10.66	0.18
R372	6.36	0.21	7.22	0.50	7.91	0.42	7.34	0.49	6.37	0.93
D374	5.64	0.08	6.61	0.35	6.47	0.20	5.82	0.11	5.84	0.24

Table S14: Fit parameters obtained after global fitting from HARD experiment for FUS-RRM (pH 4.6) at 600 MHz NMR spectrometer.

Residue	Δω (kHz)	Error	k_{ex} (kHz)	Error	P_M (%)	Error
283	0.77	0.26	0.13	0.02	98.83	0.16
285	0.86	0.28	0.12	0.01	98.15	0.14
288	0.83	0.28	0.13	0.02	97.67	0.29
289	0.80	0.27	0.12	0.02	98.28	0.21
290	1.19	0.10	0.27	0.15	98.75	0.50
291	0.88	0.28	0.14	0.02	98.88	0.18
293	0.99	0.30	0.11	0.01	97.84	0.21
295	0.90	0.28	0.12	0.01	98.61	0.12
296	0.30	0.40	0.67	0.50	98.06	1.91
297	0.95	0.29	0.13	0.03	98.09	0.22
298	0.66	0.18	0.12	0.01	98.16	0.18
299	0.74	0.22	0.12	0.02	98.38	0.19
300	0.83	0.28	0.14	0.04	98.15	0.37
301	0.00	0.00	0.56	0.57	90.16	7.45
302	0.84	0.28	0.16	0.05	98.27	0.42
303	0.74	0.22	0.11	0.01	98.00	0.12
304	0.68	0.18	0.12	0.02	98.29	0.21
305	0.66	0.18	0.11	0.01	98.73	0.12
306	1.20	0.20	0.19	0.11	97.80	0.70
307	0.68	0.17	0.11	0.01	98.87	0.14
308	0.79	0.27	0.14	0.07	98.22	0.50
309	0.93	0.31	0.11	0.01	97.90	0.17
310	1.01	0.25	0.15	0.07	99.35	0.25
311	0.81	0.26	0.12	0.03	97.31	0.43
313	0.95	0.29	0.11	0.01	98.30	0.15
314	0.86	0.30	0.11	0.01	98.04	0.10
317	0.76	0.23	0.12	0.02	98.85	0.14
318	0.90	0.30	0.11	0.01	98.11	0.14
321	0.71	0.19	0.11	0.01	98.02	0.42
322	0.75	0.24	0.16	0.06	98.50	0.36

324	0.67	0.19	0.14	0.03	98.28	0.29
326	0.81	0.29	0.10	0.00	98.54	0.05
327	1.16	0.20	0.16	0.06	97.36	0.70
329	0.12	0.33	0.81	0.66	97.37	1.70
331	0.66	0.18	0.11	0.01	97.92	0.18
332	0.12	0.33	0.89	0.95	93.84	6.33
338	0.84	0.30	0.11	0.01	98.17	0.14
339	0.83	0.30	0.12	0.01	98.16	0.20
340	0.62	0.01	0.11	0.01	98.68	0.09
341	0.76	0.29	0.11	0.01	97.35	0.19
346	0.85	0.28	0.13	0.02	98.48	0.16
347	1.06	0.17	0.11	0.01	94.53	0.39
349	0.61	0.02	0.14	0.03	98.91	0.18
350	0.74	0.22	0.11	0.01	99.06	0.09
351	0.77	0.27	0.12	0.01	97.72	0.24
352	0.79	0.26	0.12	0.01	97.50	0.18
353	0.78	0.27	0.12	0.01	98.95	0.12
354	1.17	0.08	0.27	0.19	97.06	1.05
355	0.76	0.24	0.13	0.02	98.30	0.17
356	0.75	0.26	0.13	0.02	99.11	0.10
358	0.62	0.36	0.18	0.15	99.73	0.10
359	0.96	0.29	0.12	0.01	96.06	0.27
360	0.72	0.23	0.13	0.02	97.31	0.33
361	0.77	0.24	0.13	0.01	96.56	0.14
362	0.60	0.03	0.11	0.01	98.33	0.12
364	0.77	0.26	0.12	0.02	98.89	0.15
366	0.87	0.24	0.14	0.03	98.23	0.26
367	0.81	0.26	0.12	0.01	98.26	0.16
372	0.70	0.57	0.27	0.27	98.76	1.70
374	0.13	0.24	3.30	4.35	97.71	1.84

Table S15: R_1 relaxation rates measured from HARD experiment in presence of ATP for FUS-RRM (pH 4.6) at 600 MHz NMR spectrometer. Only data for which good fits were obtained have been shown.

Residue	R_1 (s^{-1})	Error
283	1.53	0.02
285	1.43	0.05
286	1.64	0.09
287	1.87	0.10
288	1.62	0.13
290	1.45	0.08
291	1.55	0.10
293	1.51	0.07
294	1.32	0.04
295	1.42	0.03
296	1.25	0.10
297	1.52	0.07
298	1.52	0.07
299	1.40	0.05
300	1.54	0.04
302	1.44	0.04
303	1.54	0.08
304	1.67	0.06
305	1.73	0.06
306	1.51	0.04
307	1.53	0.03
308	1.72	0.09
309	1.53	0.05
310	1.21	0.12
311	1.65	0.18
313	1.41	0.09
317	1.42	0.02
318	1.39	0.02
319	1.59	0.04
322	1.59	0.11

323	1.53	0.04
324	1.32	0.07
326	1.42	0.03
327	1.46	0.02
329	1.37	0.02
331	1.45	0.03
332	1.55	0.02
333	1.47	0.05
338	1.60	0.10
339	1.49	0.20
340	1.55	0.04
341	1.45	0.11
343	1.58	0.03
346	1.49	0.07
350	1.53	0.11
351	1.63	0.08
352	1.49	0.04
353	1.42	0.10
354	1.58	0.08
355	1.54	0.02
356	0.99	0.06
358	1.55	0.03
359	1.50	0.06
360	1.50	0.04
361	1.42	0.06
362	1.48	0.02
367	1.56	0.02
369	1.45	0.05
372	1.67	0.09
374	1.60	0.01

Table S16: $R_{1\rho}$ relaxation rates measured using HSn pulses (n=1,2,4,6,8) from HARD experiment in presence of ATP for FUS-RRM (pH 4.6) at 600 MHz NMR spectrometer. Only data for which good fits were obtained have been shown.

Residue Number	$R_{1\rho}$ (s^{-1})									
	HS1		HS2		HS4		HS6		HS8	
	Value	Error	Value	Error	Value	Error	Value	Error	Value	Error
283	3.20	0.13	3.71	0.14	4.23	0.17	3.86	0.09	4.63	0.17
285	3.97	0.25	5.02	0.22	5.57	0.24	5.56	0.27	5.76	0.25
286	4.14	0.69	4.55	0.62	5.03	0.52	5.18	0.86	8.75	2.16
287	4.40	0.53	5.16	0.56	6.35	1.08	5.49	0.38	6.16	0.49
288	4.47	0.64	4.82	0.20	5.87	0.39	5.82	0.39	6.25	0.35
290	4.02	0.38	3.83	0.36	3.41	0.34	4.00	0.47	5.91	0.46
291	3.29	0.18	4.87	0.08	4.90	0.50	5.67	0.38	5.64	0.20
293	4.40	0.31	5.74	0.48	6.28	0.30	6.86	0.26	6.98	0.48
294	5.12	0.19	6.59	0.39	8.13	0.26	8.34	0.32	9.53	0.41
295	3.08	0.18	5.01	0.22	5.97	0.47	5.46	0.37	4.98	0.26
296	2.88	0.39	5.20	0.25	6.25	0.71	4.82	0.38	5.19	0.93
297	4.44	0.24	5.48	0.35	6.53	0.48	5.95	0.26	6.88	0.44
298	4.27	0.32	4.85	0.28	5.86	0.59	5.43	0.46	6.65	0.42
299	2.89	0.11	3.56	0.17	3.15	0.13	2.90	0.13	3.36	0.12
300	4.63	0.26	5.31	0.25	6.37	0.64	5.89	0.36	6.93	0.46
302	4.60	0.37	5.24	0.38	6.26	0.51	5.74	0.45	7.51	0.29
303	4.95	0.37	5.42	0.28	6.23	0.45	6.13	0.20	7.42	0.62
304	4.48	0.18	4.22	0.22	4.67	0.13	4.73	0.11	7.42	0.76
305	4.97	0.39	5.45	0.32	6.76	0.44	5.94	0.23	7.88	0.60
306	3.68	0.37	4.53	0.15	5.35	0.38	5.37	0.22	5.71	0.41
307	4.91	0.30	5.88	0.23	6.97	0.43	6.41	0.16	7.48	0.45
308	4.76	0.51	5.81	0.30	7.02	0.58	6.47	0.42	7.79	0.65
309	4.79	0.31	5.78	0.35	6.57	0.47	6.27	0.41	7.33	0.72
310	2.65	0.64	5.33	0.53	5.99	0.43	5.80	0.43	4.22	0.61
311	3.88	0.35	4.94	0.45	6.83	0.37	6.03	0.48	6.93	0.58
313	3.56	0.27	4.00	0.13	4.67	0.28	4.61	0.28	4.73	1.68
317	4.26	0.21	5.02	0.23	5.59	0.28	5.43	0.29	6.11	0.23

318	4.04	0.22	4.68	0.23	5.71	0.27	5.55	0.26	5.77	0.22
319	3.27	0.13	3.96	0.20	4.35	0.17	4.22	0.11	5.03	0.31
322	3.89	0.42	4.10	0.33	5.22	0.23	4.40	0.18	6.28	0.49
323	3.40	0.13	5.15	0.24	5.46	0.35	5.16	0.20	4.91	0.15
324	4.11	0.33	4.94	0.38	6.10	0.37	5.13	0.38	6.04	0.31
326	4.32	0.06	5.16	0.14	6.00	0.24	6.33	0.41	7.12	0.46
327	4.81	0.44	5.32	0.14	6.46	0.36	6.32	0.20	7.37	0.44
329	4.67	0.22	5.44	0.12	6.53	0.26	6.05	0.23	7.29	0.24
331	3.70	0.12	4.37	0.18	5.14	0.39	4.98	0.18	5.54	0.22
332	2.77	0.10	3.41	0.09	3.19	0.10	3.27	0.10	3.58	0.08
333	4.43	0.25	5.30	0.33	6.79	0.53	6.10	0.33	6.97	0.39
338	3.33	0.35	4.37	0.39	5.53	0.45	5.28	0.19	6.09	0.31
339	4.69	0.49	4.78	0.53	6.77	0.90	4.74	0.58	6.55	0.84
340	4.58	0.29	5.14	0.19	5.66	0.23	5.49	0.20	6.51	0.41
341	3.53	0.17	4.25	0.17	5.20	0.29	4.89	0.32	6.31	0.56
343	3.74	0.13	4.30	0.21	4.68	0.24	4.22	0.14	4.83	0.13
346	3.71	0.17	5.27	0.25	6.40	0.52	6.27	0.48	6.31	0.67
350	5.42	0.51	5.70	0.20	6.22	0.52	6.32	0.26	7.81	0.58
351	3.97	0.32	4.48	0.40	5.42	0.29	5.39	0.54	6.73	0.61
352	4.62	0.25	5.36	0.20	6.03	0.34	5.73	0.20	7.02	0.42
353	4.08	0.16	5.99	0.64	7.00	0.32	6.25	0.28	6.41	0.18
354	4.17	0.43	5.43	0.27	6.53	0.41	5.84	0.31	6.70	0.57
355	4.51	0.18	5.09	0.21	5.75	0.23	5.85	0.22	6.77	0.33
356	2.95	0.33	3.29	0.28	3.19	0.32	3.00	0.38	3.35	0.47
358	2.65	0.11	2.67	0.07	2.75	0.15	2.68	0.05	3.23	0.12
359	3.59	0.26	4.14	0.28	5.41	0.38	5.85	0.29	5.19	0.39
360	4.78	0.31	5.82	0.30	5.91	0.32	5.98	0.12	7.31	0.27
361	3.31	0.18	4.91	0.28	5.84	0.30	5.90	0.17	6.42	0.39
362	3.88	0.15	4.36	0.16	4.96	0.18	5.12	0.11	5.69	0.26
367	3.77	0.07	5.00	0.18	5.16	0.29	5.76	0.21	6.05	0.09
369	4.52	0.61	5.20	0.41	5.71	0.76	5.37	0.43	6.85	0.65
372	3.82	0.38	3.78	0.39	4.75	0.46	4.03	0.29	4.90	0.17

374	3.75	0.11	4.48	0.21	4.84	0.35	4.30	0.27	4.60	0.09

Table S17: $R_{2\rho}$ relaxation rates measured using HSn pulses (n=1,2,4,6,8) from HARD experiment in presence of ATP for FUS-RRM (pH 4.6) at 600 MHz NMR spectrometer. Only data for which good fits were obtained have been shown.

Residue Number	$R_{2\rho}$ (s^{-1})									
	HS1		HS2		HS4		HS6		HS8	
	Value	Error	Value	Error	Value	Error	Value	Error	Value	Error
283	10.85	0.33	9.61	0.29	9.65	0.23	9.03	0.29	8.26	0.43
285	12.23	0.61	13.31	0.51	12.27	0.74	11.25	0.58	11.93	0.69
286	11.48	0.34	11.00	1.16	11.17	1.44	11.52	1.74	10.91	1.60
287	17.12	0.97	14.19	0.96	16.22	1.19	13.81	1.00	11.91	1.13
288	14.50	1.49	12.27	0.33	15.75	1.49	12.19	0.58	12.31	0.54
290	12.19	0.70	12.93	0.98	12.45	5.04	12.35	2.75	10.89	1.50
291	13.05	0.38	13.84	1.06	13.70	0.71	12.13	0.49	11.80	0.76
293	15.91	1.27	14.68	0.76	13.78	0.36	12.38	0.67	12.28	0.82
294	22.40	0.69	20.17	0.74	20.36	1.08	17.86	0.99	15.98	1.22
295	12.02	0.44	11.59	0.47	11.19	0.34	10.56	0.19	10.48	0.62
296	10.12	0.70	9.14	0.51	9.14	0.56	9.65	0.24	8.31	0.80
297	13.74	1.11	12.84	0.59	13.64	1.28	12.31	0.61	12.34	1.08
298	15.05	0.75	14.29	0.48	15.08	0.69	14.19	0.96	13.20	0.58
299	3.87	0.23	5.67	0.09	3.75	0.35	7.09	2.46	4.79	0.04
300	12.29	0.76	11.62	0.70	11.72	0.66	10.85	0.59	10.46	0.49
302	14.87	0.85	14.32	0.84	13.49	1.70	12.36	0.80	12.88	0.67
303	15.11	1.05	13.87	0.36	14.77	0.99	13.02	0.27	12.68	0.19
304	15.12	0.45	13.92	0.21	13.88	0.33	12.82	0.55	13.16	0.57
305	14.77	0.69	13.89	0.49	13.57	0.53	12.48	0.62	11.65	0.45
306	13.26	0.20	11.97	0.42	12.46	0.82	11.13	0.41	10.86	0.48
307	14.33	0.46	13.79	0.48	13.01	0.76	12.53	0.66	12.47	0.34
308	14.69	0.68	14.05	0.61	16.18	1.61	13.06	0.25	12.16	1.29
309	14.11	1.10	12.81	0.82	13.00	1.17	12.05	1.07	12.13	0.76
310	16.19	1.99	14.79	1.52	6.27	2.24	7.80	2.72	12.67	2.04
311	18.70	2.40	14.99	1.12	17.42	1.38	14.76	0.76	14.77	1.28
313	12.38	0.66	12.27	0.52	12.02	1.23	11.33	0.57	10.63	0.77

317	13.03	0.57	11.61	0.35	12.12	0.95	11.35	0.63	11.08	0.73
318	12.11	0.99	11.04	0.64	10.92	0.75	10.85	0.53	11.03	0.59
319	11.74	0.35	11.36	0.19	12.01	0.39	10.54	0.40	10.53	0.37
322	13.55	0.57	12.70	0.60	12.90	0.57	11.25	0.43	11.01	0.38
323	8.64	0.58	7.79	0.20	7.83	0.63	7.33	0.40	6.99	0.59
324	12.23	0.37	12.02	0.76	12.65	0.91	11.15	0.19	10.93	0.70
326	15.25	1.14	15.18	0.72	14.05	0.83	12.74	0.90	13.57	0.94
327	17.41	0.41	15.56	0.36	16.22	0.79	14.58	0.56	14.40	0.86
329	15.85	0.25	12.50	2.84	14.87	0.24	13.73	0.42	13.66	0.50
331	10.65	0.89	9.02	0.85	9.96	1.20	8.71	0.63	8.36	0.43
332	5.84	0.23	5.59	0.13	5.93	0.19	5.50	0.10	5.34	0.13
333	15.59	0.66	13.45	0.35	13.45	4.57	12.33	0.79	12.39	0.18
338	15.49	0.58	14.94	0.66	14.24	0.49	12.86	0.82	13.36	1.08
339	17.20	1.41	11.37	0.62	10.42	2.33	11.20	1.00	10.51	1.26
340	14.46	0.75	12.56	0.51	12.57	0.83	11.69	0.27	11.92	0.29
341	13.86	0.42	12.45	0.81	12.34	0.60	13.09	0.61	12.15	0.65
343	7.28	0.39	6.90	0.20	7.04	0.52	6.69	0.31	6.57	0.24
346	13.43	1.06	12.06	0.56	12.31	0.95	10.89	0.94	9.70	0.80
350	13.48	1.31	11.97	0.85	12.65	1.21	9.43	0.40	9.47	0.72
351	17.92	1.88	15.13	0.63	15.58	0.70	16.18	0.58	14.64	0.95
352	16.48	0.67	15.33	0.38	16.19	0.51	14.46	0.30	14.82	0.26
353	15.79	0.94	13.86	0.32	14.40	0.34	13.86	0.82	13.12	0.62
354	19.71	0.93	17.90	0.99	16.53	2.02	14.90	1.33	14.54	1.49
355	16.14	0.27	14.65	0.30	14.94	0.32	13.86	0.19	13.91	0.52
356	3.11	0.44	3.11	0.28	2.96	0.52	2.43	0.39	2.71	0.39
358	5.93	0.29	5.61	0.22	5.68	0.33	5.18	0.27	5.27	0.33
359	17.09	0.50	16.69	0.27	17.04	1.68	15.02	0.97	16.01	0.87
360	17.13	0.64	16.77	0.45	16.20	0.66	14.71	0.59	16.17	1.02
361	14.94	0.41	15.34	0.52	14.28	0.38	14.80	0.40	14.82	0.63
362	11.77	0.40	10.76	0.29	11.13	0.25	10.32	0.12	10.64	0.29
367	14.35	0.58	13.47	0.23	13.39	0.45	12.51	0.33	12.37	0.26
369	12.86	1.02	12.41	1.62	10.38	1.30	10.47	0.70	8.79	0.81

372	8.22	0.69	7.96	0.40	8.12	0.59	7.82	0.30	6.88	0.30
374	5.91	0.51	8.38	2.26	5.51	0.47	5.09	0.41	5.14	0.35

Table S18: Fit parameters obtained after global fitting from HARD experiment in presence of ATP for FUS-RRM (pH 4.6) at 600 MHz NMR spectrometer.

Residue	**Δω (kHz)**	**Error**	**k_{ex} (kHz)**	**Error**	**P_M (%)**	**Error**
283	0.49	0.32	28.90	2.24	81.73	18.59
285	1.18	0.04	0.18	0.13	98.49	0.51
286	0.29	0.05	52.50	2.45	73.05	9.08
287	0.90	0.41	24.84	2.80	91.17	13.68
288	0.88	0.31	0.13	0.01	97.91	0.15
290	0.47	0.31	26.41	0.44	88.15	8.11
291	0.66	0.19	0.12	0.02	97.61	0.28
293	0.67	0.33	36.31	3.50	88.31	13.19
294	0.44	0.19	36.78	0.51	75.52	14.03
295	1.18	0.11	0.39	0.38	99.12	0.42
296	0.79	0.31	0.15	0.05	99.49	0.13
297	0.50	0.34	43.91	2.10	80.75	12.22
298	1.26	0.01	0.37	0.23	98.57	0.65
299	0.19	0.38	1.20	1.94	95.34	5.31
300	0.48	0.27	64.76	2.08	79.24	11.18
302	0.69	0.37	37.57	2.15	91.17	8.06
303	0.62	0.26	36.96	3.38	90.75	9.23
304	1.26	0.01	0.39	0.25	98.31	0.90
305	0.67	0.38	36.46	3.31	87.51	12.49
306	0.68	0.29	34.83	2.20	93.82	7.71
307	0.51	0.25	52.64	3.45	83.96	11.57
308	0.97	0.32	0.19	0.07	98.63	0.35
309	0.57	0.28	50.82	4.69	88.44	7.33
310	0.29	0.04	36.88	2.42	80.64	9.31
311	0.88	0.30	0.19	0.08	97.43	0.79
313	0.57	0.36	30.61	2.69	85.77	13.78
317	0.57	0.35	41.47	2.10	86.53	13.75
318	0.69	0.39	40.70	2.08	89.94	11.69

319	1.26	0.02	0.21	0.11	98.00	0.71
322	0.86	0.47	3.96	8.82	88.03	16.68
323	0.25	0.40	0.86	1.36	96.75	2.51
324	1.18	0.20	0.20	0.09	98.89	0.30
326	0.81	0.34	37.24	3.00	93.55	8.67
327	0.45	0.22	33.14	3.21	82.17	12.21
329	1.05	0.26	0.34	0.13	98.85	0.35
331	0.40	0.26	54.07	2.15	80.00	10.14
332	0.49	0.26	0.37	0.67	99.63	0.16
333	0.64	0.35	38.04	4.89	88.25	10.60
338	1.18	0.09	0.28	0.20	97.78	1.05
339	0.42	0.27	34.88	0.96	80.67	12.81
340	0.77	0.33	35.08	2.91	94.65	5.52
341	1.16	0.19	0.37	0.38	98.41	1.04
343	0.18	0.36	1.36	2.46	93.80	6.76
346	0.38	0.13	53.40	1.64	77.87	12.59
350	0.73	0.25	208.96	13.72	77.58	12.40
351	0.99	0.29	0.16	0.04	96.51	0.71
352	1.26	0.02	0.23	0.14	97.74	0.89
353	0.57	0.30	34.89	2.09	87.87	13.16
354	0.81	0.31	23.18	1.95	96.33	3.31
355	1.24	0.06	0.25	0.16	98.14	0.82
356	0.01	0.00	0.81	0.71	96.66	1.08
358	0.32	0.29	33.05	1.27	78.89	12.50
359	1.23	0.04	0.63	0.58	98.20	1.46
360	1.22	0.07	0.35	0.32	98.03	1.31
361	0.79	0.26	0.13	0.03	97.12	0.35
362	0.87	0.33	0.16	0.06	98.74	0.28
367	1.24	0.06	0.42	0.32	98.89	0.48
369	0.42	0.24	54.36	3.08	80.56	11.64
372	0.36	0.19	44.76	2.04	81.60	13.83

Table S19: R_1, R_2, [^{1}H]-^{15}N nOe relaxation rates measured for FUS-RRM (pH 6.4) at 600 MHz NMR spectrometer. Only data for which good fits were obtained have been shown.

Residue number	R_1 (s^{-1})		R_2 (s^{-1})		[^{1}H]-^{15}N nOe	
	Value	Error	Value	Error	Value	Error
D283	1.51	0.06	9.58	0.06	0.61	0.01
N285	1.37	0.05	12.13	0.06	0.78	0.01
F288	1.42	0.03	11.73	0.07	0.82	0.01
V289	1.36	0.02	12.41	0.31	0.78	0.03
Q290	1.36	0.05	11.08	0.09	0.78	0.01
G291	1.29	0.08	11.18	0.16	0.76	0.01
G293	1.39	0.04	12.49	0.05	0.71	0.01
E294	1.27	0.03	13.24	0.05	0.70	0.01
N295	1.40	0.01	10.91	0.04	0.67	0.01
V296	1.16	0.06	9.73	0.07	0.50	0.02
T297	1.33	0.08	10.90	0.07	0.70	0.01
I298	1.38	0.08	11.33	0.10	0.77	0.02
E299	1.32	0.11	12.40	0.11	0.80	0.01
S300	1.32	0.11	11.97	0.11	0.70	0.01
V301	1.43	0.08	10.83	0.13	0.78	0.03
A302	1.44	0.03	13.13	0.23	0.78	0.02
D303	1.30	0.07	12.27	0.04	0.76	0.01
Y304	1.39	0.02	12.97	0.07	0.78	0.01
F305	1.36	0.11	11.77	0.09	0.79	0.01
K306	1.40	0.05	11.83	0.07	0.75	0.01
Q307	1.46	0.01	13.42	0.09	0.74	0.01
I308	1.40	0.04	13.03	0.13	0.74	0.02
G309	1.36	0.05	13.27	0.08	0.71	0.01
I310	1.21	0.04	11.40	0.09	0.63	0.01
I311	1.39	0.05	15.05	0.18	0.77	0.02
T313	1.33	0.06	12.86	0.11	0.75	0.01

N314	1.25	0.08	11.76	0.09	0.74	0.01
T317	1.34	0.03	11.43	0.11	0.65	0.01
G318	1.39	0.06	10.76	0.10	0.70	0.01
Q319	1.35	0.10	11.19	0.04	0.61	0.01
M321	1.08	0.12	11.03	0.28	0.73	0.08
I322	1.29	0.05	11.76	0.15	0.77	0.02
L324	1.30	0.07	10.92	0.11	0.75	0.01
T326	1.42	0.03	12.26	0.17	0.75	0.01
D327	1.30	0.04	11.94	0.09	0.71	0.01
E329	1.34	0.09	11.37	0.04	0.53	0.004
T330	1.25	0.02	16.46	0.17	0.58	0.01
G331	1.43	0.05	10.51	0.09	0.68	0.01
K332	1.52	0.07	5.53	0.04	0.05	0.01
G335	1.36	0.07	15.90	0.71	0.74	0.02
T338	1.39	0.05	14.15	0.76	0.81	0.01
V339	1.34	0.07	10.48	0.13	0.84	0.03
S340	1.36	0.10	11.19	0.09	0.74	0.01
F341	1.36	0.04	11.10	0.11	0.77	0.02
D343	1.45	0.09	7.34	0.09	0.30	0.01
S346	1.39	0.02	12.43	0.09	0.77	0.01
A347	1.44	0.07	13.64	0.19	0.88	0.03
A349	1.45	0.03	13.42	0.13	0.78	0.02
A350	1.45	0.02	12.39	0.19	0.72	0.02
I351	1.35	0.05	12.84	0.15	0.77	0.02
D352	1.36	0.10	12.78	0.13	0.79	0.01
W353	1.33	0.09	12.51	0.07	0.69	0.01
F354	1.33	0.08	13.36	0.11	0.81	0.01
D355	1.35	0.10	13.88	0.03	0.77	0.01
E358	1.25	0.09	10.96	0.05	0.69	0.01
F359	1.34	0.05	13.94	0.14	0.76	0.02
S360	1.34	0.08	12.03	0.25	0.79	0.02
G361	1.38	0.03	13.24	0.12	0.75	0.01

N362	1.35	0.06	11.26	0.03	0.72	0.01
I364	1.45	0.08	13.28	0.06	0.65	0.01
V366	1.32	0.10	11.46	0.26	0.79	0.04
S367	1.38	0.04	12.92	0.08	0.57	0.01
A369	1.45	0.08	11.10	0.12	0.78	0.02
T370	1.33	0.10	10.19	0.10	0.63	0.01
R372	1.64	0.03	7.00	0.09	0.43	0.02
D374	1.60	0.07	6.51	0.06	0.27	0.003

Table S20: R_1, R_2, [^{1}H]-^{15}N nOe relaxation rates measured for FUS-RRM (pH 4.6) at 600 MHz NMR spectrometer. Only data for which good fits were obtained have been shown.

Residue number	**R_1 (s^{-1})**		**R_2 (s^{-1})**		**[^{1}H]-^{15}N nOe**	
	Value	**Error**	**Value**	**Error**	**Value**	**Error**
D283	1.43	0.08	9.12	0.07	0.52	0.01
N285	1.37	0.06	6.11	0.71	0.78	0.01
F288	1.43	0.04	12.44	0.57	0.79	0.02
V289	1.43	0.06	13.86	0.27	0.71	0.04
Q290	1.32	0.05	12.42	0.27	0.60	0.02
G291	1.29	0.08	11.51	0.32	0.75	0.02
G293	1.39	0.03	14.14	0.38	0.71	0.01
E294	1.30	0.05	19.35	0.21	0.68	0.01
N295	1.39	0.03	11.13	0.16	0.66	0.01
V296	1.22	0.04	9.88	0.16	0.46	0.02
T297	1.36	0.08	11.99	0.31	0.66	0.01
I298	1.38	0.04	12.12	0.24	0.73	0.02
E299	1.45	0.05	12.90	0.15	0.67	0.01
S300	1.38	0.09	12.96	0.24	0.76	0.01
V301	1.38	0.09	11.77	0.21	0.60	0.02
A302	1.47	0.05	13.48	0.52	0.78	0.03
D303	1.38	0.03	13.67	0.48	0.79	0.01
Y304	1.45	0.04	11.61	0.17	0.79	0.01

F305	1.36	0.09	12.34	0.32	0.76	0.02
K306	1.38	0.04	12.43	0.21	0.72	0.01
Q307	1.49	0.01	13.03	0.12	0.70	0.01
I308	1.38	0.04	13.50	0.28	0.72	0.02
G309	1.38	0.05	14.47	0.49	0.72	0.01
I310	1.25	0.05	12.66	0.28	0.61	0.01
I311	1.41	0.05	15.80	0.44	0.73	0.03
T313	1.33	0.04	12.74	0.34	0.78	0.01
N314	1.27	0.08	11.58	0.21	0.70	0.01
T317	1.32	0.02	13.14	0.61	0.61	0.01
G318	1.40	0.05	11.34	0.28	0.68	0.01
Q319	1.36	0.09	10.69	0.13	0.60	0.01
M321	1.19	0.10	10.95	0.50	0.73	0.08
I322	1.34	0.05	12.98	0.44	0.74	0.02
L324	1.32	0.07	11.39	0.31	0.70	0.02
T326	1.29	0.04	13.53	0.32	0.71	0.02
D327	1.32	0.05	13.92	0.15	0.72	0.01
E329	1.37	0.08	13.66	0.13	0.53	0.005
T330	1.26	0.02	28.96	0.82	0.54	0.01
G331	1.44	0.05	9.53	0.32	0.26	0.00
K332	1.40	0.05	4.40	0.07	0.08	0.00
G335	1.37	0.08	19.73	1.05	0.72	0.03
T338	1.40	0.06	15.21	0.82	0.80	0.01
V339	1.40	0.04	11.80	0.40	0.77	0.04
S340	1.41	0.08	11.96	0.16	0.74	0.02
F341	1.41	0.05	12.70	0.48	0.79	0.02
D343	1.41	0.07	7.70	0.37	0.15	0.00
S346	1.44	0.03	12.24	0.08	0.77	0.01
A347	1.42	0.05	14.28	0.43	0.76	0.04
A349	1.47	0.04	5.39	0.56	0.82	0.03
A350	1.44	0.06	13.95	1.00	0.81	0.03
I351	1.38	0.08	13.15	0.31	0.80	0.02

D352	1.39	0.07	14.16	0.26	0.76	0.01
W353	1.37	0.08	12.16	0.17	0.78	0.01
F354	1.38	0.07	13.89	0.19	0.78	0.02
D355	1.39	0.08	13.99	0.15	0.76	0.01
E358	1.41	0.08	5.68	0.16	0.30	0.00
F359	1.32	0.05	15.99	0.46	0.75	0.02
S360	1.38	0.07	15.23	0.67	0.75	0.02
G361	1.33	0.02	14.22	0.18	0.68	0.01
N362	1.37	0.06	11.54	0.22	0.71	0.01
I364	1.58	0.09	12.40	0.14	0.66	0.01
V366	1.41	0.06	11.96	0.60	0.75	0.04
S367	1.37	0.08	11.90	0.10	0.78	0.01
A369	1.44	0.09	11.11	0.27	0.76	0.03
T370	1.26	0.09	10.25	0.08	0.62	0.01
R372	1.50	0.07	7.56	0.34	0.27	0.01
D374	1.53	0.05	5.97	0.09	0.23	0.003

Table S21: ^{15}N CEST I/I_0 data at pH 6.4.

	I/I_0															
^{15}N Offset (ppm)	**N285**	**G293**	**E294**	**T297**	**E299**	**S300**	**D303**	**F305**	**Q307**	**T317**	**T330**	**T338**	**D352**	**D355**	**I351**	**G356**
102.0	0.58	0.51	0.60	0.58	0.58	0.59	0.58	0.59	0.56	0.54	0.58	0.54	0.58	0.58	0.61	0.57
102.5	0.58	0.47	0.60	0.59	0.58	0.59	0.58	0.58	0.57	0.53	0.57	0.54	0.58	0.59	0.60	0.57
103.0	0.57	0.42	0.59	0.59	0.58	0.59	0.57	0.58	0.57	0.50	0.55	0.56	0.57	0.59	0.60	0.56
103.5	0.56	0.35	0.61	0.59	0.58	0.60	0.58	0.58	0.57	0.46	0.53	0.55	0.58	0.59	0.60	0.57
104.0	0.58	0.19	0.60	0.58	0.58	0.59	0.58	0.58	0.56	0.37	0.51	0.53	0.56	0.59	0.61	0.56
104.5	0.56	0.03	0.60	0.58	0.58	0.59	0.58	0.57	0.57	0.20	0.47	0.52	0.57	0.59	0.60	0.56
105.0	0.57	0.01	0.59	0.58	0.58	0.58	0.58	0.56	0.57	0.04	0.40	0.51	0.58	0.59	0.58	0.56
105.5	0.57	0.07	0.59	0.58	0.58	0.59	0.58	0.57	0.56	0.00	0.28	0.50	0.59	0.58	0.61	0.57
106.0	0.58	0.23	0.60	0.58	0.58	0.59	0.58	0.58	0.56	0.06	0.12	0.47	0.58	0.58	0.59	0.57
106.5	0.57	0.37	0.59	0.57	0.58	0.59	0.58	0.57	0.56	0.25	0.00	0.41	0.57	0.59	0.62	0.57
107.0	0.58	0.43	0.59	0.56	0.57	0.59	0.58	0.57	0.56	0.40	0.01	0.30	0.58	0.58	0.61	0.56
107.5	0.56	0.49	0.60	0.56	0.57	0.59	0.57	0.57	0.56	0.47	0.04	0.15	0.58	0.59	0.60	0.54
108.0	0.58	0.52	0.59	0.55	0.59	0.58	0.58	0.55	0.56	0.51	0.21	0.02	0.57	0.59	0.59	0.55
108.5	0.57	0.51	0.57	0.52	0.57	0.58	0.57	0.54	0.56	0.53	0.36	0.00	0.58	0.59	0.59	0.55
109.0	0.57	0.50	0.56	0.50	0.58	0.57	0.57	0.54	0.56	0.55	0.43	0.06	0.57	0.58	0.59	0.51
109.5	0.56	0.53	0.56	0.46	0.58	0.58	0.57	0.52	0.55	0.55	0.48	0.23	0.58	0.57	0.61	0.51
110.0	0.56	0.54	0.55	0.38	0.57	0.57	0.57	0.48	0.55	0.57	0.51	0.36	0.57	0.59	0.59	0.52
110.5	0.56	0.57	0.54	0.24	0.57	0.56	0.56	0.45	0.55	0.57	0.53	0.43	0.56	0.57	0.57	0.55
111.0	0.55	0.58	0.51	0.06	0.57	0.56	0.55	0.37	0.55	0.58	0.56	0.46	0.56	0.57	0.60	0.53
111.5	0.57	0.57	0.47	0.00	0.57	0.55	0.54	0.22	0.55	0.57	0.56	0.49	0.58	0.57	0.58	0.53
112.0	0.56	0.58	0.39	0.04	0.57	0.55	0.53	0.05	0.53	0.56	0.56	0.51	0.57	0.58	0.58	0.50
112.5	0.55	0.56	0.26	0.22	0.56	0.53	0.51	0.01	0.52	0.56	0.55	0.52	0.55	0.57	0.59	0.49
113.0	0.55	0.57	0.07	0.36	0.56	0.51	0.48	0.03	0.51	0.56	0.54	0.53	0.55	0.56	0.58	0.45
113.5	0.57	0.57	0.00	0.45	0.56	0.48	0.43	0.20	0.47	0.56	0.55	0.52	0.53	0.56	0.60	0.40
114.0	0.56	0.57	0.01	0.50	0.55	0.41	0.34	0.35	0.44	0.58	0.58	0.51	0.53	0.55	0.60	0.32
114.5	0.56	0.57	0.14	0.52	0.52	0.30	0.19	0.44	0.38	0.60	0.59	0.52	0.52	0.54	0.58	0.16
115.0	0.54	0.58	0.31	0.55	0.51	0.13	0.03	0.48	0.27	0.59	0.59	0.54	0.50	0.53	0.56	0.01
115.5	0.55	0.58	0.42	0.55	0.48	0.01	0.00	0.50	0.09	0.60	0.60	0.56	0.45	0.50	0.55	0.00
116.0	0.53	0.58	0.48	0.56	0.44	0.01	0.05	0.52	-0.01	0.60	0.60	0.56	0.41	0.46	0.52	0.04
116.5	0.53	0.58	0.51	0.55	0.38	0.11	0.22	0.53	0.01	0.59	0.60	0.55	0.31	0.41	0.56	0.19
117.0	0.51	0.56	0.53	0.55	0.24	0.28	0.35	0.53	0.14	0.59	0.60	0.57	0.14	0.32	0.51	0.32
117.5	0.49	0.58	0.54	0.54	0.07	0.39	0.42	0.53	0.29	0.60	0.61	0.56	0.02	0.15	0.45	0.40
118.0	0.45	0.57	0.56	0.55	0.01	0.46	0.45	0.54	0.39	0.60	0.61	0.55	0.00	0.02	0.39	0.48
118.5	0.37	0.57	0.56	0.57	0.01	0.50	0.49	0.56	0.44	0.61	0.60	0.55	0.08	0.01	0.26	0.49
119.0	0.25	0.58	0.56	0.58	0.17	0.53	0.53	0.56	0.45	0.62	0.60	0.56	0.25	0.06	0.08	0.51
119.5	0.08	0.57	0.55	0.59	0.32	0.54	0.54	0.57	0.48	0.61	0.60	0.56	0.37	0.23	0.02	0.53
120.0	0.00	0.57	0.56	0.57	0.42	0.54	0.55	0.57	0.51	0.60	0.61	0.57	0.44	0.35	0.01	0.53
120.5	0.02	0.58	0.58	0.59	0.46	0.54	0.56	0.58	0.53	0.60	0.62	0.56	0.47	0.43	0.16	0.55
121.0	0.15	0.58	0.59	0.59	0.50	0.55	0.55	0.56	0.54	0.60	0.62	0.57	0.50	0.47	0.29	0.53
121.5	0.31	0.57	0.60	0.59	0.51	0.56	0.57	0.57	0.54	0.60	0.62	0.56	0.52	0.48	0.40	0.54
122.0	0.42	0.58	0.60	0.59	0.53	0.58	0.57	0.58	0.55	0.60	0.61	0.58	0.54	0.50	0.47	0.54
122.5	0.47	0.58	0.59	0.58	0.52	0.58	0.58	0.58	0.55	0.61	0.61	0.57	0.53	0.54	0.52	0.56
123.0	0.49	0.57	0.60	0.59	0.52	0.58	0.58	0.58	0.55	0.60	0.61	0.57	0.52	0.55	0.53	0.56
123.5	0.52	0.58	0.60	0.58	0.52	0.58	0.58	0.56	0.55	0.61	0.60	0.58	0.54	0.56	0.54	0.56

124.0	0.54	0.59	0.60	0.59	0.55	0.58	0.58	0.59	0.56	0.61	0.61	0.57	0.55	0.57	0.57	0.56
124.5	0.54	0.59	0.61	0.59	0.56	0.58	0.58	0.58	0.56	0.60	0.60	0.58	0.56	0.57	0.56	0.56
125.0	0.55	0.58	0.60	0.60	0.56	0.58	0.58	0.59	0.56	0.60	0.61	0.57	0.56	0.57	0.60	0.58
125.5	0.57	0.59	0.60	0.60	0.57	0.59	0.58	0.58	0.56	0.61	0.61	0.57	0.57	0.58	0.60	0.56
126.0	0.56	0.58	0.60	0.60	0.57	0.59	0.59	0.58	0.55	0.60	0.61	0.56	0.58	0.58	0.59	0.55
126.5	0.56	0.57	0.60	0.60	0.57	0.59	0.58	0.59	0.56	0.60	0.62	0.57	0.58	0.58	0.59	0.58
127.0	0.56	0.58	0.60	0.59	0.57	0.58	0.59	0.58	0.56	0.60	0.61	0.57	0.58	0.58	0.60	0.59
127.5	0.55	0.58	0.61	0.59	0.58	0.59	0.59	0.58	0.56	0.60	0.60	0.56	0.59	0.57	0.61	0.57
128.0	0.57	0.58	0.60	0.60	0.57	0.58	0.59	0.59	0.56	0.60	0.61	0.57	0.58	0.57	0.59	0.56
128.5	0.56	0.59	0.61	0.60	0.58	0.59	0.58	0.59	0.56	0.60	0.60	0.57	0.59	0.57	0.61	0.57
129.0	0.58	0.59	0.60	0.60	0.57	0.59	0.58	0.58	0.57	0.61	0.62	0.56	0.58	0.59	0.60	0.56
129.5	0.57	0.58	0.60	0.60	0.58	0.59	0.59	0.60	0.57	0.60	0.61	0.56	0.58	0.58	0.59	0.57
130.0	0.56	0.58	0.61	0.59	0.56	0.59	0.58	0.58	0.56	0.61	0.61	0.57	0.59	0.58	0.59	0.56
130.5	0.56	0.58	0.60	0.59	0.58	0.59	0.59	0.58	0.56	0.60	0.62	0.57	0.59	0.57	0.62	0.56
131.0	0.56	0.57	0.60	0.60	0.58	0.59	0.58	0.58	0.56	0.61	0.62	0.57	0.59	0.57	0.57	0.57
131.5	0.58	0.59	0.60	0.60	0.58	0.60	0.59	0.58	0.57	0.61	0.63	0.57	0.57	0.58	0.61	0.57
132.0	0.58	0.58	0.60	0.60	0.58	0.59	0.58	0.60	0.57	0.61	0.61	0.57	0.57	0.58	0.61	0.59
132.5	0.58	0.58	0.60	0.59	0.58	0.59	0.58	0.58	0.57	0.61	0.60	0.55	0.57	0.59	0.61	0.56
133.0	0.57	0.58	0.61	0.59	0.58	0.59	0.59	0.59	0.56	0.61	0.60	0.57	0.58	0.59	0.59	0.55

Table S22: ^{15}N CEST I/I_0 data at pH 4.6.

	I/I_0									
^{15}N offset (ppm)	**E294**	**T297**	**E299**	**F305**	**Q307**	**T317**	**T330**	**T338**	**D352**	**S360**
102.0	0.56	0.58	0.59	0.58	0.58	0.56	0.52	0.55	0.55	0.57
102.5	0.59	0.56	0.57	0.60	0.55	0.55	0.60	0.56	0.58	0.54
103.0	0.60	0.60	0.59	0.60	0.58	0.50	0.54	0.54	0.60	0.59
103.5	0.60	0.61	0.58	0.56	0.56	0.47	0.53	0.53	0.59	0.62
104.0	0.60	0.59	0.58	0.61	0.54	0.38	0.48	0.55	0.58	0.65
104.5	0.59	0.58	0.60	0.58	0.55	0.21	0.46	0.51	0.57	0.57
105.0	0.58	0.59	0.59	0.58	0.55	0.06	0.37	0.51	0.58	0.59
105.5	0.62	0.60	0.59	0.58	0.56	-0.02	0.29	0.51	0.58	0.62
106.0	0.58	0.54	0.58	0.62	0.55	0.04	0.14	0.48	0.58	0.62
106.5	0.61	0.55	0.59	0.57	0.57	0.20	0.03	0.39	0.58	0.59
107.0	0.57	0.57	0.58	0.57	0.55	0.37	0.00	0.31	0.60	0.62
107.5	0.58	0.56	0.58	0.55	0.56	0.45	0.04	0.15	0.58	0.57
108.0	0.59	0.54	0.59	0.56	0.54	0.49	0.01	0.02	0.59	0.58
108.5	0.58	0.54	0.58	0.53	0.56	0.51	0.09	-0.01	0.54	0.60
109.0	0.57	0.50	0.57	0.56	0.55	0.54	0.18	0.04	0.56	0.60
109.5	0.57	0.46	0.57	0.51	0.55	0.54	0.29	0.15	0.57	0.61
110.0	0.53	0.35	0.57	0.51	0.53	0.53	0.37	0.32	0.56	0.62
110.5	0.52	0.23	0.56	0.45	0.55	0.55	0.47	0.43	0.58	0.62
111.0	0.48	0.09	0.55	0.35	0.54	0.55	0.50	0.47	0.57	0.58

111.5	0.46	-0.02	0.57	0.24	0.54	0.54	0.52	0.47	0.58	0.57
112.0	0.40	-0.03	0.55	0.05	0.55	0.54	0.49	0.52	0.57	0.61
112.5	0.25	0.10	0.57	-0.01	0.51	0.50	0.44	0.51	0.55	0.62
113.0	0.11	0.26	0.54	0.02	0.51	0.52	0.48	0.50	0.54	0.58
113.5	0.02	0.39	0.55	0.13	0.48	0.56	0.52	0.49	0.52	0.65
114.0	-0.01	0.46	0.54	0.30	0.43	0.57	0.57	0.44	0.52	0.56
114.5	0.01	0.46	0.54	0.41	0.37	0.58	0.59	0.46	0.50	0.58
115.0	0.15	0.54	0.50	0.46	0.24	0.59	0.60	0.50	0.49	0.61
115.5	0.28	0.52	0.47	0.51	0.09	0.62	0.62	0.55	0.42	0.59
116.0	0.36	0.56	0.40	0.53	0.04	0.61	0.58	0.55	0.34	0.56
116.5	0.44	0.50	0.30	0.52	0.01	0.60	0.61	0.58	0.22	0.60
117.0	0.45	0.55	0.14	0.52	0.12	0.62	0.60	0.58	0.05	0.54
117.5	0.49	0.48	0.02	0.45	0.26	0.59	0.55	0.57	-0.01	0.50
118.0	0.49	0.50	0.01	0.53	0.37	0.62	0.60	0.58	-0.02	0.49
118.5	0.50	0.52	0.05	0.55	0.39	0.61	0.65	0.59	0.10	0.51
119.0	0.49	0.56	0.24	0.54	0.41	0.62	0.60	0.56	0.25	0.53
119.5	0.48	0.58	0.36	0.55	0.42	0.58	0.61	0.57	0.38	0.53
120.0	0.52	0.60	0.42	0.55	0.50	0.60	0.62	0.58	0.43	0.55
120.5	0.54	0.59	0.44	0.58	0.51	0.60	0.60	0.54	0.45	0.53
121.0	0.59	0.57	0.47	0.57	0.53	0.62	0.57	0.60	0.48	0.50
121.5	0.60	0.60	0.48	0.58	0.56	0.62	0.60	0.55	0.48	0.55
122.0	0.57	0.59	0.51	0.58	0.53	0.62	0.59	0.56	0.47	0.47
122.5	0.57	0.56	0.47	0.60	0.53	0.58	0.61	0.60	0.46	0.44
123.0	0.60	0.60	0.46	0.61	0.56	0.58	0.61	0.59	0.50	0.34
123.5	0.61	0.58	0.50	0.59	0.57	0.61	0.62	0.58	0.53	0.26
124.0	0.60	0.60	0.52	0.60	0.55	0.61	0.61	0.56	0.55	0.13
124.5	0.60	0.62	0.54	0.60	0.56	0.61	0.62	0.57	0.56	0.00
125.0	0.59	0.60	0.57	0.56	0.57	0.60	0.60	0.55	0.54	0.00
125.5	0.60	0.61	0.58	0.59	0.55	0.61	0.57	0.61	0.59	0.03
126.0	0.58	0.60	0.58	0.59	0.55	0.60	0.65	0.54	0.55	0.13
126.5	0.60	0.60	0.58	0.61	0.56	0.59	0.63	0.58	0.56	0.38
127.0	0.60	0.63	0.55	0.57	0.55	0.63	0.63	0.56	0.57	0.42
127.5	0.62	0.56	0.57	0.63	0.56	0.62	0.64	0.59	0.57	0.50
128.0	0.61	0.60	0.58	0.59	0.53	0.60	0.61	0.60	0.57	0.48
128.5	0.62	0.59	0.58	0.59	0.57	0.59	0.63	0.58	0.58	0.54
129.0	0.62	0.60	0.57	0.57	0.54	0.62	0.62	0.57	0.57	0.56
129.5	0.60	0.60	0.57	0.59	0.57	0.63	0.62	0.55	0.59	0.56
130.0	0.64	0.60	0.59	0.58	0.55	0.61	0.65	0.57	0.60	0.59
130.5	0.60	0.58	0.58	0.60	0.55	0.59	0.63	0.51	0.59	0.56
131.0	0.62	0.61	0.59	0.60	0.55	0.60	0.66	0.59	0.54	0.55
131.5	0.59	0.56	0.58	0.59	0.58	0.62	0.62	0.58	0.56	0.60
132.0	0.61	0.58	0.58	0.64	0.53	0.60	0.62	0.59	0.57	0.63
132.5	0.57	0.59	0.57	0.59	0.58	0.60	0.63	0.58	0.59	0.59

133.0	0.59	0.59	0.57	0.59	0.56	0.61	0.61	0.57	0.59	0.64
133.5	0.60	0.56	0.58	0.58	0.54	0.61	0.61	0.58	0.58	0.62
134.0	0.59	0.60	0.59	0.57	0.55	0.62	0.59	0.57	0.59	0.63

Table S23: ^{15}N CEST I/I_0 data for 1M urea.

	I/I_0													
^{15}N offset (ppm)	**G293**	**E294**	**T297**	**E299**	**S300**	**D303**	**F305**	**Q307**	**T317**	**T330**	**T338**	**D352**	**D355**	**G356**
102.0	0.48	0.58	0.54	0.52	0.58	0.56	0.54	0.54	0.52	0.54	0.54	0.53	0.56	0.53
102.5	0.47	0.58	0.54	0.54	0.57	0.55	0.54	0.55	0.50	0.54	0.53	0.54	0.55	0.51
103.0	0.42	0.58	0.52	0.54	0.56	0.56	0.53	0.54	0.49	0.54	0.50	0.55	0.56	0.54
103.5	0.35	0.58	0.54	0.54	0.56	0.56	0.53	0.55	0.44	0.51	0.50	0.54	0.56	0.54
104.0	0.22	0.57	0.55	0.55	0.56	0.55	0.55	0.54	0.38	0.51	0.52	0.53	0.53	0.51
104.5	0.05	0.55	0.54	0.54	0.56	0.55	0.54	0.53	0.22	0.45	0.52	0.55	0.54	0.53
105.0	0.02	0.57	0.52	0.53	0.57	0.55	0.52	0.53	0.07	0.39	0.49	0.54	0.53	0.55
105.5	0.05	0.57	0.51	0.54	0.57	0.56	0.53	0.58	0.03	0.33	0.48	0.54	0.54	0.52
106.0	0.19	0.58	0.53	0.55	0.57	0.55	0.54	0.54	0.07	0.14	0.44	0.54	0.54	0.52
106.5	0.29	0.55	0.54	0.50	0.56	0.55	0.54	0.55	0.25	0.00	0.41	0.55	0.56	0.50
107.0	0.39	0.56	0.53	0.52	0.56	0.54	0.54	0.53	0.36	0.01	0.30	0.53	0.55	0.52
107.5	0.42	0.57	0.52	0.54	0.56	0.55	0.56	0.52	0.46	0.08	0.20	0.55	0.54	0.51
108.0	0.46	0.59	0.49	0.53	0.56	0.56	0.55	0.56	0.48	0.23	0.04	0.55	0.55	0.55
108.5	0.41	0.56	0.49	0.55	0.57	0.56	0.50	0.53	0.48	0.36	0.01	0.53	0.54	0.50
109.0	0.38	0.55	0.45	0.54	0.56	0.54	0.49	0.53	0.50	0.44	0.08	0.54	0.56	0.38
109.5	0.42	0.55	0.43	0.56	0.55	0.55	0.49	0.54	0.54	0.48	0.20	0.53	0.55	0.40
110.0	0.48	0.53	0.36	0.55	0.56	0.54	0.46	0.54	0.54	0.51	0.33	0.53	0.55	0.47
110.5	0.48	0.52	0.24	0.54	0.55	0.54	0.41	0.52	0.53	0.49	0.35	0.52	0.55	0.46
111.0	0.53	0.49	0.07	0.51	0.55	0.52	0.34	0.54	0.52	0.54	0.44	0.51	0.56	0.48
111.5	0.51	0.45	0.01	0.53	0.55	0.51	0.22	0.51	0.55	0.53	0.44	0.53	0.54	0.46
112.0	0.51	0.40	0.05	0.51	0.54	0.51	0.07	0.49	0.54	0.51	0.48	0.53	0.52	0.47
112.5	0.50	0.29	0.21	0.52	0.52	0.50	0.00	0.49	0.49	0.52	0.50	0.52	0.53	0.42
113.0	0.52	0.10	0.33	0.52	0.50	0.46	0.04	0.48	0.47	0.48	0.47	0.50	0.53	0.43
113.5	0.52	0.01	0.39	0.52	0.47	0.44	0.19	0.45	0.46	0.44	0.46	0.52	0.55	0.39
114.0	0.52	-0.01	0.46	0.52	0.42	0.37	0.32	0.43	0.47	0.50	0.42	0.50	0.54	0.27
114.5	0.52	0.12	0.49	0.51	0.33	0.24	0.38	0.39	0.52	0.52	0.43	0.49	0.51	0.19

115.0	0.55	0.28	0.50	0.49	0.17	0.06	0.45	0.27	0.51	0.56	0.46	0.48	0.51	0.03
115.5	0.55	0.42	0.49	0.45	0.02	0.01	0.44	0.06	0.55	0.56	0.52	0.45	0.47	0.01
116.0	0.53	0.46	0.52	0.42	0.01	0.05	0.46	0.00	0.56	0.57	0.53	0.42	0.47	0.03
116.5	0.55	0.48	0.50	0.38	0.10	0.21	0.49	0.01	0.54	0.57	0.54	0.31	0.41	0.14
117.0	0.50	0.52	0.50	0.27	0.27	0.31	0.49	0.14	0.55	0.57	0.55	0.18	0.34	0.30
117.5	0.56	0.49	0.45	0.11	0.38	0.39	0.46	0.29	0.54	0.59	0.53	0.02	0.17	0.41
118.0	0.52	0.51	0.41	0.00	0.46	0.40	0.40	0.37	0.57	0.57	0.50	0.02	0.03	0.44
118.5	0.54	0.53	0.44	0.03	0.48	0.39	0.45	0.40	0.54	0.58	0.53	0.05	0.01	0.45
119.0	0.55	0.51	0.50	0.15	0.49	0.46	0.50	0.40	0.59	0.57	0.54	0.20	0.04	0.48
119.5	0.54	0.46	0.52	0.30	0.51	0.50	0.50	0.40	0.52	0.58	0.56	0.35	0.19	0.51
120.0	0.53	0.45	0.53	0.39	0.51	0.52	0.53	0.42	0.55	0.60	0.50	0.40	0.33	0.49
120.5	0.53	0.50	0.54	0.41	0.50	0.52	0.52	0.49	0.56	0.60	0.50	0.43	0.37	0.48
121.0	0.54	0.53	0.52	0.45	0.49	0.54	0.57	0.52	0.57	0.57	0.53	0.45	0.41	0.53
121.5	0.52	0.55	0.52	0.48	0.51	0.54	0.52	0.50	0.57	0.58	0.54	0.47	0.42	0.53
122.0	0.51	0.55	0.55	0.49	0.54	0.54	0.57	0.52	0.56	0.58	0.56	0.48	0.40	0.51
122.5	0.53	0.57	0.55	0.46	0.55	0.54	0.55	0.53	0.56	0.58	0.54	0.47	0.46	0.51
123.0	0.53	0.58	0.52	0.46	0.55	0.54	0.56	0.54	0.58	0.58	0.57	0.44	0.50	0.49
123.5	0.55	0.56	0.54	0.45	0.56	0.55	0.53	0.51	0.58	0.59	0.53	0.43	0.52	0.51
124.0	0.56	0.56	0.55	0.42	0.56	0.55	0.53	0.56	0.58	0.59	0.54	0.50	0.52	0.52
124.5	0.54	0.56	0.55	0.46	0.56	0.56	0.56	0.52	0.55	0.62	0.53	0.50	0.53	0.52
125.0	0.52	0.56	0.54	0.51	0.56	0.56	0.53	0.53	0.57	0.60	0.54	0.54	0.56	0.50
125.5	0.53	0.58	0.53	0.51	0.58	0.55	0.55	0.55	0.58	0.59	0.55	0.54	0.55	0.51
126.0	0.55	0.57	0.54	0.53	0.58	0.55	0.54	0.55	0.57	0.61	0.51	0.53	0.55	0.52
126.5	0.53	0.59	0.55	0.52	0.56	0.56	0.57	0.51	0.56	0.59	0.54	0.52	0.54	0.49
127.0	0.50	0.57	0.56	0.52	0.56	0.55	0.53	0.53	0.56	0.59	0.54	0.54	0.54	0.50
127.5	0.55	0.57	0.55	0.52	0.57	0.56	0.57	0.56	0.58	0.55	0.52	0.53	0.55	0.52
128.0	0.54	0.57	0.53	0.54	0.57	0.57	0.54	0.54	0.57	0.56	0.57	0.53	0.54	0.55
128.5	0.55	0.57	0.54	0.53	0.56	0.57	0.54	0.54	0.58	0.59	0.53	0.53	0.55	0.53
129.0	0.52	0.57	0.53	0.55	0.57	0.56	0.52	0.54	0.55	0.58	0.53	0.55	0.55	0.53
129.5	0.55	0.58	0.54	0.54	0.56	0.57	0.55	0.54	0.55	0.57	0.51	0.53	0.53	0.53
130.0	0.55	0.58	0.54	0.53	0.58	0.54	0.56	0.54	0.55	0.58	0.52	0.56	0.55	0.50
130.5	0.54	0.58	0.54	0.53	0.57	0.58	0.55	0.55	0.57	0.58	0.55	0.54	0.57	0.50

131.0	0.54	0.57	0.53	0.54	0.57	0.55	0.52	0.54	0.57	0.62	0.53	0.56	0.55	0.53
131.5	0.56	0.57	0.53	0.52	0.57	0.55	0.51	0.53	0.58	0.60	0.53	0.55	0.55	0.55
132.0	0.55	0.58	0.56	0.56	0.56	0.57	0.54	0.55	0.55	0.57	0.54	0.55	0.56	0.54
132.5	0.53	0.59	0.54	0.54	0.56	0.56	0.58	0.53	0.56	0.57	0.55	0.55	0.56	0.56
133.0	0.53	0.57	0.54	0.56	0.57	0.55	0.55	0.53	0.56	0.57	0.53	0.54	0.56	0.54

Table S24: ^{15}N CEST I/I_0 data for pH 6.4 in presence of ATP.

	I/I_0												
^{15}N offset (ppm)	**N285**	**E294**	**T297**	**E299**	**S300**	**F305**	**Q307**	**T317**	**T330**	**T338**	**D352**	**D355**	**G356**
101.17	0.58	0.61	0.63	0.56	0.59	0.60	0.57	0.57	0.60	0.55	0.60	0.59	0.61
102.49	0.58	0.62	0.60	0.58	0.60	0.60	0.58	0.48	0.55	0.53	0.64	0.57	0.60
103.81	0.59	0.61	0.62	0.59	0.59	0.59	0.56	0.15	0.41	0.52	0.64	0.57	0.57
105.13	0.55	0.62	0.60	0.60	0.60	0.57	0.57	0.06	0.12	0.47	0.62	0.60	0.61
106.45	0.58	0.61	0.61	0.57	0.60	0.58	0.55	0.43	-0.02	0.19	0.64	0.53	0.55
107.77	0.58	0.58	0.55	0.55	0.59	0.58	0.59	0.54	0.32	0.01	0.62	0.56	0.55
109.09	0.56	0.55	0.40	0.59	0.58	0.50	0.56	0.59	0.51	0.36	0.62	0.58	0.54
110.40	0.57	0.47	-0.01	0.57	0.57	0.32	0.54	0.58	0.55	0.49	0.61	0.56	0.53
111.72	0.53	0.22	0.48	0.59	0.55	0.01	0.51	0.56	0.56	0.54	0.60	0.57	0.46
113.04	0.53	0.01	0.57	0.50	0.43	0.51	0.46	0.59	0.58	0.53	0.56	0.58	0.30
114.36	0.53	0.51	0.59	0.49	0.02	0.54	0.20	0.61	0.61	0.57	0.49	0.52	-0.01
115.68	0.51	0.57	0.56	0.34	0.51	0.55	1.80025652E-4	0.61	0.62	0.55	0.27	0.40	0.44
117.00	0.46	0.57	0.60	0.01	0.55	0.58	0.47	0.61	0.65	0.54	0.01	0.02	0.48

118.32	0.15	0.57	0.62	0.49	0.56	0.61	0.55	0.61	0.63	0.57	0.49	0.11	0.59
119.64	0.03	0.60	0.62	0.50	0.59	0.62	0.55	0.62	0.64	0.57	0.54	0.43	0.56
120.96	0.38	0.61	0.61	0.53	0.59	0.57	0.55	0.63	0.62	0.61	0.56	0.48	0.58
122.28	0.49	0.62	0.63	0.59	0.59	0.64	0.55	0.63	0.65	0.57	0.61	0.56	0.61
123.60	0.54	0.61	0.61	0.55	0.60	0.59	0.57	0.60	0.64	0.57	0.60	0.57	0.58
124.91	0.56	0.62	0.63	0.56	0.60	0.65	0.57	0.60	0.63	0.57	0.62	0.58	0.58
126.23	0.55	0.62	0.65	0.57	0.60	0.62	0.57	0.60	0.64	0.57	0.62	0.57	0.61
127.55	0.57	0.60	0.60	0.58	0.60	0.61	0.56	0.63	0.63	0.61	0.63	0.58	0.57
128.87	0.56	0.61	0.63	0.59	0.59	0.60	0.56	0.63	0.63	0.59	0.61	0.57	0.59
130.19	0.58	0.62	0.66	0.62	0.59	0.62	0.57	0.63	0.64	0.58	0.62	0.57	0.64
131.51	0.54	0.63	0.60	0.58	0.61	0.60	0.57	0.62	0.64	0.58	0.62	0.58	0.61
132.83	0.58	0.63		0.58			0.57	0.64	0.64	0.58	0.62	0.60	

Table S25: ^{15}N CEST I/I_0 data for pH 4.6 in presence of ATP.

	I/I_0								
^{15}N offset (ppm)	**E294**	**T297**	**F305**	**Q307**	**T317**	**T330**	**T338**	**D352**	**S360**
101.17	0.61	0.60	0.60	0.59	0.51	0.53	0.56	0.56	0.62
102.49	0.58	0.59	0.58	0.57	0.43	0.51	0.57	0.57	0.62
103.81	0.61	0.58	0.55	0.58	0.14	0.36	0.51	0.57	0.61
105.13	0.57	0.57	0.55	0.57	0.04	0.19	0.43	0.58	0.65
106.45	0.58	0.55	0.56	0.58	0.40	0.00	0.16	0.56	0.59
107.77	0.56	0.52	0.53	0.59	0.51	0.04	-0.02	0.58	0.61
109.09	0.53	0.40	0.51	0.58	0.54	0.31	0.51	0.56	0.68
110.40	0.44	0.01	0.31	0.57	0.56	0.44	0.53	0.55	0.61
111.72	0.19	0.12	-0.02	0.54	0.51	0.47	0.50	0.54	0.63
113.04	-0.01	0.43	0.48	0.45	0.58	0.52	0.59	0.52	0.62
114.36	0.42	0.52	0.48	0.17	0.60	0.57	0.58	0.42	0.61
115.68	0.49	0.55	0.49	-0.01	0.59	0.60	0.58	0.16	0.60
117.00	0.47	0.50	0.55	0.43	0.60	0.62	0.59	-0.01	0.53
119.64	0.55	0.56	0.56	0.52	0.61	0.62	0.61	0.45	0.56
120.96	0.60	0.62	0.58	0.56	0.61	0.65	0.59	0.47	0.56
122.28	0.63	0.65	0.57	0.55	0.61	0.61	0.57	0.52	0.49
123.60	0.58	0.61	0.58	0.57	0.60	0.64	0.57	0.56	0.33
124.91	0.61	0.60	0.55	0.59	0.61	0.62	0.60	0.57	0.04
126.23	0.60	0.63	0.56	0.58	0.60	0.58	0.59	0.57	0.08
127.55	0.61	0.62	0.62	0.58	0.64	0.62	0.58	0.58	0.45
128.87	0.61	0.63	0.60	0.59	0.61	0.61	0.58	0.59	0.53

130.19	0.63	0.64	0.60	0.61	0.63	0.65	0.60	0.58	0.58
131.51	0.60	0.59	0.59	0.60	0.64	0.64	0.60	0.57	0.60
132.83	0.60	0.61	0.60	0.60	0.59	0.64	0.63	0.59	0.61

Table S26: p_{ES} and k_{ex} obtained by fitting HARD-$R_{1\rho/2\rho}$ and ^{15}N-CEST for various samples and the corresponding free energies.

HARD $R_{1\rho}$ and $R_{2\rho}$			
RRM	**p_{ES} (%)**	**k_{ex} (ks^{-1})**	**ΔG (kcal/mol)**
pH 6.4	6.2 ± 5.0	40.9 ± 2.3	1.6±0.5
pH 4.6	2.1 ± 0.6	0.3 ± 0.2	2.3±0.2
RRM + ATP	**p_{ES} (%)**	**k_{ex} (ks^{-1})**	**ΔG (kcal/mol)**
pH 6.4	2.7 ± 1.4	3.7 ± 0.5	2.1±0.3
pH 4.6	9.0 ± 6.6	23.9 ± 1.8	1.4±0.4
CEST			
RRM	**p_{ES} (%)**	**k_{ex} (ks^{-1})**	**ΔG (kcal/mol)**
pH 6.4	0.1 ± 0.0	0.3 ± 0.0	3.9±0.0
pH 4.6	0.5 ± 0.1	0.1 ± 0.0	3.1±0.1
RRM + ATP	**p_{ES} (%)**	**k_{ex} (ks^{-1})**	**ΔG (kcal/mol)**
pH 6.4	0.5 (fixed)	0.1 (fixed)	3.1±0.0
pH 4.6	0.5 ± 0.0	0.9 (fixed)	3.2±0.0
RRM + 1 M urea	**p_{ES} (%)**	**k_{ex} (ks^{-1})**	**ΔG (kcal/mol)**
pH 6.4	0.5 ± 0.0	0.2 ± 0.0	3.1±0.0